

The Halo Occupation Distribution: Towards an Empirical Determination of the Relation Between Galaxies and Mass

Andreas A. Berlind, and David H. Weinberg

Department of Astronomy, The Ohio State University, Columbus, OH 43210;

Email: aberlind,dhw@astronomy.ohio-state.edu

ABSTRACT

We investigate galaxy bias in the framework of the “Halo Occupation Distribution” (HOD), which defines the bias of a population of galaxies by the conditional probability $P(N|M)$ that a dark matter halo of virial mass M contains N galaxies, together with prescriptions that specify the relative spatial and velocity distributions of galaxies and dark matter within halos. By populating the halos of a cosmological N -body simulation using a variety of HOD models, we examine the sensitivity of different galaxy clustering statistics to properties of the HOD. The galaxy correlation function responds to different aspects of $P(N|M)$ on different scales. Obtaining the observed power-law form of $\xi_g(r)$ requires rather specific combinations of HOD parameters, implying a strong constraint on the physics of galaxy formation; the success of numerical and semi-analytic models in reproducing this form is entirely non-trivial. Other clustering statistics such as the galaxy-mass correlation function, the bispectrum, the void probability function, the pairwise velocity dispersion, and the group multiplicity function are sensitive to different combinations of HOD parameters and thus provide complementary information about galaxy bias. We outline a strategy for determining the HOD empirically from redshift survey data. This method starts from an assumed cosmological model, but we argue that cosmological and HOD parameters will have non-degenerate effects on galaxy clustering, so that a substantially incorrect cosmological model will not reproduce the observations for any choice of HOD. Empirical determinations of the HOD as a function of galaxy type from the 2dF and SDSS redshift surveys will provide a detailed target for theories of galaxy formation, insight into the origin of galaxy properties, and sharper tests of cosmological models.

Subject headings: cosmology: theory, galaxies: formation, large-scale structure of universe

1. Introduction

The relation between the galaxy and dark matter distributions depends on the physics of galaxy formation, and it is expected that galaxies are, at least to some degree, biased tracers of the mass distribution. This expectation, which is supported by observational evidence that galaxy clustering varies with luminosity, morphology, and color (Guzzo et al. 1997; Norberg et al. 2001;

Zehavi et al. 2001; and references therein), complicates efforts to test cosmological models against observed galaxy clustering. However, the presence of bias also implies that galaxy clustering can be used to constrain the physics of galaxy formation, especially as independent observations define the background cosmology with increasing precision (e.g., Wang, Tegmark, & Zaldarriaga 2001). The 2dF and SDSS galaxy redshift surveys (Colless et al. 2001; York et al. 2000), which can measure the clustering of different galaxy types with unprecedented detail, are now bringing this goal within reach. Achieving it requires a language for describing bias that is powerful enough to capture the information in these measurements and thereby connect observations of galaxy clustering to the physics of galaxy formation.

In this paper, we examine the influence of bias on galaxy clustering statistics, using the framework of the “Halo Occupation Distribution” (HOD). This approach describes bias at the level of “virialized” dark matter halos, structures of typical overdensity $\rho/\bar{\rho} \sim 200$, which are expected to be in approximate dynamical equilibrium. Gas dynamics, radiative cooling, and star formation can strongly influence the distribution of galaxies *within* such halos (e.g., the numbers, masses, and locations of galaxies), but the masses and spatial distribution of halos themselves should be determined mainly by gravitational dynamics of the dark matter. In the HOD framework, the bias of any particular class of galaxies is fully defined by the probability distribution $P(N|M)$ that a halo of virial mass M contains N galaxies, along with the relations between the galaxy and dark matter spatial and velocity distributions within halos. While the history of the galaxy population is necessarily entwined with the background cosmology, the HOD description suggests a useful conceptual division between the “cosmological model” and the “theory of galaxy formation” in predictions of galaxy clustering: the cosmological model determines the properties of the halo distribution, and the theory of galaxy formation specifies how those halos are populated with galaxies.

The most important strength of the HOD formulation of bias is its completeness. For a given cosmological model, the HOD tells us everything a theory of galaxy formation has to say about the statistics of galaxy clustering, in real space and redshift space, and on small, intermediate, and large scales¹. Conversely, if we can determine the HOD empirically, we will learn everything that observed galaxy clustering has to tell us about the physics of galaxy formation. Moreover, the HOD provides a physically informative basis for interpreting discrepancies between predicted and observed galaxy clustering, or between predictions of different galaxy formation theories themselves. It would be more illuminating to learn, for example, that a given theory predicts too many red galaxies in halos of mass $10^{13} - 10^{14} M_{\odot}$ than to learn that it predicts the wrong 3-point correlation function of such galaxies. Finally, since the HOD describes bias at the level of systems near dynamical equilibrium, empirical determinations of the HOD can take advantage of mass estimation methods that are inapplicable on large scales. For example, traditional virial methods and X-ray mass estimates of clusters can provide fairly direct constraints on $P(N|M)$ at high M (see § 5).

The halo occupation framework has a long history, initially in analytic models that described galaxy clustering as a superposition of randomly distributed clusters with specified profiles and a

¹We discuss some caveats to this assertion at the end of § 2

range of masses (Neyman & Scott 1952; McClelland & Silk 1977; Peebles 1974). The explosion of recent activity in this field has been fueled partly by the recognition that a combination of this approach with recently developed tools for predicting the spatial clustering of halos (Mo & White 1996) provides a powerful formalism for analytic calculations of dark matter clustering, which can be naturally extended to biased galaxy populations (e.g., Seljak 2000; Ma & Fry 2000; Peacock & Smith 2000; Scoccimarro et al. 2000; White 2001; and numerous other papers referred to in subsequent sections). Our own interest was sparked largely by the paper of Benson et al. (2000; see Kauffmann, Nusser, & Steinmetz 1997 and Kauffmann et al. 1999 for similar analyses), who demonstrated that they could reproduce the clustering of galaxies in their semi-analytic models by populating N-body halos according to a predicted $P(N|M)$. Furthermore, they showed that the predicted clustering depends not only on the complex mass dependence of the mean occupation, but also on finer details of sub-Poisson fluctuations about the mean. This result illustrates the power of the HOD to test detailed predictions of galaxy formation theories. Models of $P(N|M)$ based on semi-analytic calculations of Benson et al. (2000) and Kauffmann et al. (1999) have been incorporated into several of the papers cited above, and some recent papers have presented predictions of hydrodynamic simulations for $P(N|M)$ (White, Hernquist, & Springel 2001; Yoshikawa et al. 2001). We will compare predictions of $P(N|M)$ from hydrodynamic simulations and semi-analytic calculations in a future study (Berlind et al., in preparation).

The HOD description can be contrasted with another widely used approach that characterizes bias in terms of the correlation between galaxy density and properties of the large-scale environment, such as mass density, temperature, and geometry. This “environmental bias” approach has been used to study the effects of generic biasing models on galaxy clustering statistics (Weinberg 1995; Mann, Peacock, & Heavens 1998; Dekel & Lahav 1999; Narayanan, Berlind, & Weinberg 2000; Berlind, Narayanan, & Weinberg 2001) and to encapsulate predictions of hydrodynamic simulations and semi-analytic galaxy formation models (Blanton et al. 1999; Cen & Ostriker 2000; Somerville et al. 2001; Yoshikawa et al. 2001). It has also led to valuable analytic results concerning the shape of the galaxy power spectrum and the influence of bias on higher-order clustering on large scales (Coles 1993; Fry & Gaztañaga 1993; Fry 1994; Juszkiewicz et al. 1995; Scherrer & Weinberg 1998; Coles, Melott, & Munshi 1999). However, this formulation cannot effectively describe bias on scales smaller than the smoothing length used to define the environment, and the choice of smoothing scale is, itself, rather arbitrary. In the HOD framework, there is some range of reasonable methods for defining halos, but the choice of $\rho/\bar{\rho} \sim 200$ for a typical halo boundary is well motivated by the division between the infall and dynamical equilibrium regimes. Also, as already noted, this choice allows use of virial mass estimates to constrain $P(N|M)$ empirically, while the large-scale matter density, which plays a fundamental role in environmental formulations of bias, is generally unobservable.

Our methodology in this paper is to define generic models of the HOD, apply them to an N-body simulation of the inflationary cold dark matter scenario (see § 2), and investigate the dependence of galaxy clustering statistics on the HOD parameters. This numerical approach complements earlier analytic work on halo bias by considering a wider range of clustering statistics and HOD models, some of them not readily amenable to analytic calculations. We will interpret our results in light of the analytic formalism developed in other papers and in terms of some heuristic analytic models presented here as a guide for understanding. The next section defines our

HOD prescriptions more formally. We then devote considerable attention, in § 3, to the two-point correlation function $\xi(r)$, because of its intrinsic importance and in order to illustrate some general features of the way the HOD influences galaxy clustering. We consider other clustering statistics in § 4, and properties of galaxy groups in § 5. A general theme emerging from these results is that different statistics respond to different features of the HOD, implying that precise measurements of galaxy clustering can in principle yield an empirical determination of the HOD. Achieving this goal in practice requires a scheme for getting a good first guess at the HOD that will reproduce the observed galaxy clustering. We outline such a scheme and present an illustrative test in § 6. In its present form, this scheme assumes that the underlying cosmology is known, but we speculate on prospects for breaking the degeneracy between bias and cosmology. We summarize our results in § 7.

2. Models of the Halo Occupation Distribution

In the HOD framework, the relation between the galaxy and matter distributions is fully defined by

- (1) the probability distribution $P(N|M)$ that a halo of virial mass M contains N galaxies,
- (2) the relation between the galaxy and dark matter spatial distributions within halos, and
- (3) the relation between the galaxy and dark matter velocity distributions within halos.

We use the term “Halo Occupation Distribution” (or HOD) to refer to all three of these aspects. Each individual class of galaxies (defined, for example, by luminosity and color ranges or by morphological type) has its own HOD.

For this study we have used the high resolution GIF N-body simulations carried out by the Virgo consortium (Jenkins et al. 1998). The particular model we have focused on is the flat Λ CDM model with $\Omega_m = 0.3$, $\Omega_\Lambda = 0.7$, $H_0 = 70 \text{ km s}^{-1} \text{ Mpc}^{-1}$, and a spectral shape parameter $\Gamma = 0.21$ (in the parameterization of Efstathiou, Bond, & White 1992). The simulation follows the evolution of 256^3 particles, each of mass $1.4 \times 10^{10} h^{-1} M_\odot$, in a comoving box of size $141.3 h^{-1} \text{ Mpc}$. The rms mass fluctuations on a scale of $8 h^{-1} \text{ Mpc}$ are $\sigma_8 = 0.9$, in agreement with the observed abundance of clusters (Eke, Cole, & Frenk 1996). Gravitational forces are significantly softer than $1/r^2$ on scales $\lesssim 30 h^{-1} \text{ kpc}$.

We identify halos in the dark matter distribution using a “friends-of-friends” (FoF) algorithm (Davis et al. 1985) with a linking length of 0.2 times the mean inter-particle separation, and we only consider halos consisting of 10 or more particles. This means that the smallest halos we can resolve have a mass of $1.4 \times 10^{11} h^{-1} M_\odot$.

For our present purposes, an HOD prescription amounts to a recipe for selecting a subset of the dark matter particles in these halos to represent the galaxy population of the simulation. Most of the models we show in this paper are tuned to produce a galaxy population with a space density of $\bar{n}_g = 0.01 h^3 \text{ Mpc}^{-3}$. This space density corresponds to galaxies of luminosity $L \gtrsim 0.5 L_*$, assuming no further cuts in color or morphology. Our HOD prescriptions consist of the following features:

1. $N_{\text{avg}}(M)$ – We consider two types of models for this relation, power laws and broken power

laws. In the power-law models, the mean number of galaxies that populate dark matter halos of mass M is

$$N_{\text{avg}} = \begin{cases} 0 & \text{if } M < M_{\text{min}} \\ (M/M_1)^\alpha & \text{otherwise,} \end{cases} \quad (1)$$

where α is the power-law index, M_{min} is the cutoff halo mass below which halos cannot contain galaxies, and M_1 sets the amplitude of the relation and corresponds to the mass of halos that contain, on average, one galaxy. In the broken power-law models,

$$N_{\text{avg}} = \begin{cases} 0 & \text{if } M < M_{\text{min}} \\ (M/M_1)^\alpha & \text{if } M_{\text{min}} \leq M \leq M_{\text{crit}} \\ (M/M'_1)^\beta & \text{otherwise,} \end{cases} \quad (2)$$

where α and β are the low and high mass power-law indices, M_{crit} is the halo mass at which the power-law slope breaks, and M'_1 is required by continuity to be $M'_1 = M_1^{(\alpha/\beta)} M_{\text{crit}}^{(1-\alpha/\beta)}$. For a given HOD model, the value of M_1 is chosen to produce a galaxy population of the desired space density.

The parameters M_{min} , α , β , and M_{crit} are directly related to the efficiency of galaxy formation as a function of halo mass. For example, bright galaxies cannot form in halos below a certain mass because these halos do not contain enough cold gas, hence the need for M_{min} . The simplest form of $N_{\text{avg}}(M)$ would have N proportional to M ($\alpha = 1$) for $M > M_{\text{min}}$. However, many physical mechanisms can alter the efficiency of galaxy formation as a function of halo mass. For example, the typical cooling time for gas increases with halo mass, and this suggests that $\alpha < 1$. This effect could be counteracted by an earlier average formation time of galaxies that end up in high mass halos. Galaxy mergers may alter galaxy numbers preferentially in intermediate mass halos, where mergers are most frequent. Any given physical process can affect $N_{\text{avg}}(M)$ differently for different galaxy classes. For example, mergers decrease the number of low luminosity galaxies but increase the number of high luminosity galaxies. Morphological transformations, likewise, increase the numbers of one galaxy type while decreasing those of another. We will, therefore, be able to learn much about the processes that determine galaxy properties by comparing the HOD for different galaxy classes.

2. $P(N|N_{\text{avg}})$ – Once N_{avg} is determined, the actual number of galaxies that occupies any given halo is drawn from a probability distribution $P(N|N_{\text{avg}})$. We consider three such probability distributions: (a) a Poisson distribution; (b) a very narrow distribution, which we call “Average”, where the actual number of galaxies is the integer either above or below N_{avg} , with relative frequencies needed to give the required mean (this is identical to the “Average” distribution used by Benson et al. 2000); (c) a Negative Binomial distribution, which is substantially wider than Poisson. Although it is possible for the form of $P(N|N_{\text{avg}})$ to vary with M , we do not consider such models in this paper. Figure 1 shows $P(N|M)$ for a particular HOD prescription (power-law $N_{\text{avg}}(M)$ with $M_{\text{min}} = 2.8 \times 10^{11} h^{-1} M_\odot$, $\alpha = 0.5$). Each point represents the number of galaxies chosen to occupy a particular halo in the dark matter distribution. The two panels show the difference between assuming an Average and a Poisson $P(N|N_{\text{avg}})$.

In the high halo mass regime, $P(N|N_{\text{avg}})$ should depend on the statistics of halo merger histories (Lacey & Cole 1993). The distribution of merger histories for halos of a given mass

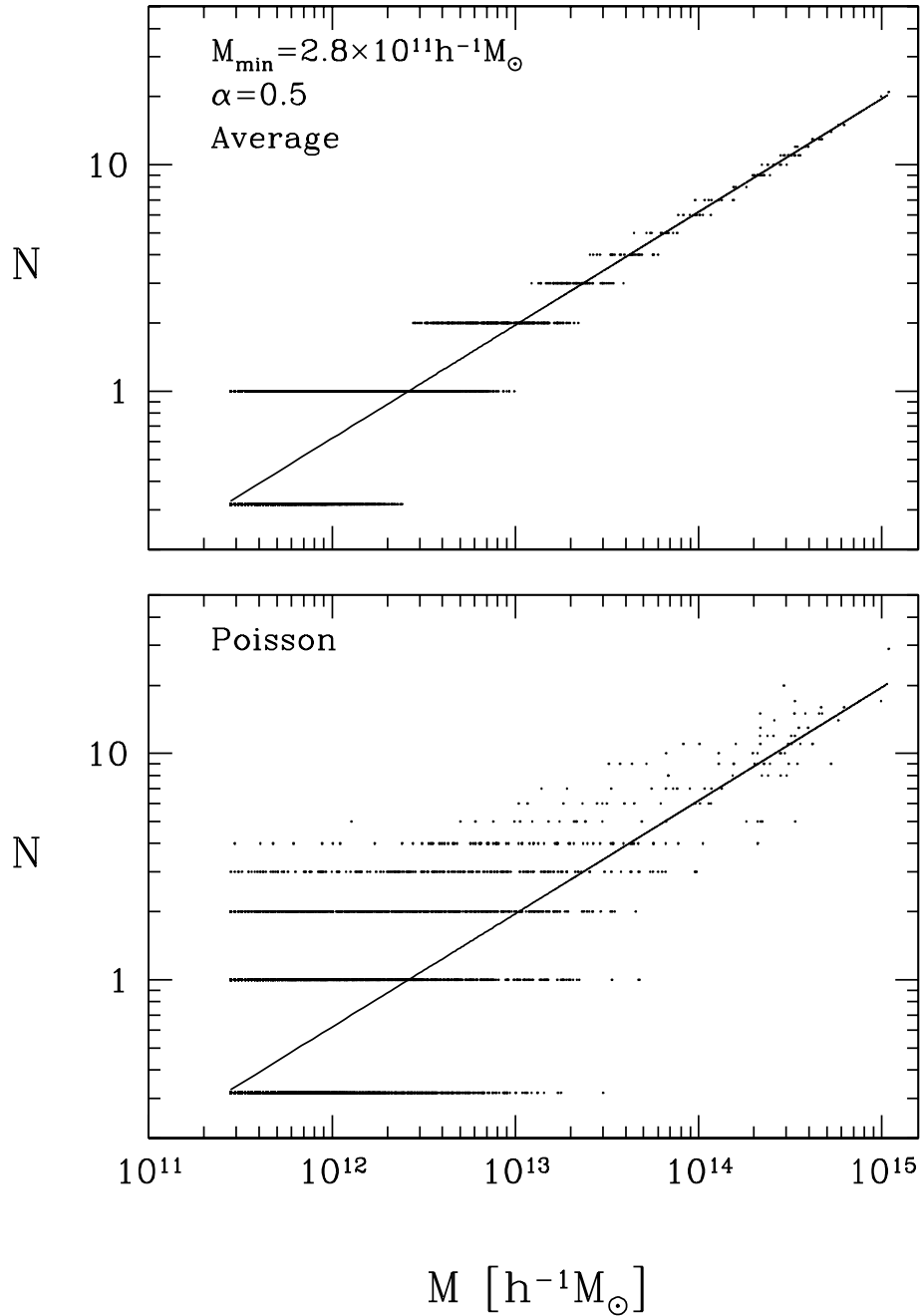


Fig. 1.— $P(N|M)$ relation for two particular HOD models. Each point represents the number of galaxies that occupy a single halo in the N -body simulation. Points for halos that contain no galaxies are arbitrarily placed at $\log N = -0.5$. The HOD prescriptions shown have a power-law $N_{\text{avg}}(M)$ with $\alpha = 0.5$ and $M_{\text{min}} = 2.8 \times 10^{11} h^{-1} M_{\odot}$ (see definitions in § 2), as indicated by the solid lines. The $P(N|N_{\text{avg}})$ distribution are Average (top panel) and Poisson (bottom panel).

will produce a resulting distribution of galaxy numbers for those halos. In the low mass regime, each halo is expected to contain only one galaxy, but whether that galaxy would pass a given luminosity threshold depends on the gas cooling and star formation history of that halo. Therefore, $P(N|N_{\text{avg}})$ depends on the regularity of galaxy formation in halos of a given final mass.

3. *Central galaxy* – Once the actual number of galaxies N that occupy each halo is determined, we must specify how these galaxies are distributed within halos. The first step in this process is to specify whether or not there must be a galaxy at the center of each halo for which $N > 0$. We investigate both these cases. If we force a galaxy to sit at the halo center, we place it at the halo center of mass and assign it the mean halo velocity.

4. *Galaxy concentration* – We allow for the possibility that galaxies are more or less spatially concentrated than the dark matter within halos. We implement such models by selecting “galaxy” particles with probability $P \propto r^{\Delta\gamma}$, so that, on average,

$$\rho_g(r)/\rho_m(r) = r^{\Delta\gamma}. \quad (3)$$

This prescription imposes a difference $\Delta\gamma$ in the logarithmic slopes of galaxy and dark matter profiles without imposing any specific form or symmetry on the galaxy distribution in the halos; the galaxy distribution will inherit the geometry of the dark matter. A non-zero $\Delta\gamma$ can be applied together with the central galaxy prescription or on its own.

5. *Velocity bias* – Finally, we allow for the possibility of velocity bias within halos. The mean velocity of galaxies in a halo should not differ from that of the dark matter, since both components are responding to the same large-scale gravitational field. However, the galaxies in a halo might have a higher or lower velocity dispersion than the dark matter particles at the same locations. We define a velocity bias factor α_v through the relation

$$\mathbf{v}_g = \mathbf{v}_h + \alpha_v(\mathbf{v}_m - \mathbf{v}_h), \quad (4)$$

where \mathbf{v}_g and \mathbf{v}_m are the velocities of the galaxies and the dark matter particles that they are assigned to and \mathbf{v}_h is the mean center-of-mass halo velocity. For example, if $\alpha_v = 0$ all the galaxies within a halo have the mean halo velocity, while if $\alpha_v = 1$ galaxy velocities trace the dark matter velocities. Our central galaxy and galaxy concentration prescriptions impose some degree of velocity bias even if $\alpha_v = 1$, the first because the central galaxy is assumed to move at \mathbf{v}_h , and the second because the typical dark matter velocities depend on radius if the halo is not isothermal.

Prescriptions 3, 4, and 5 allow us to represent a number of physical processes that could affect the galaxy distribution in important ways. For example, dynamical friction could cause galaxies to sink to the center of a halo and end up with a spatial distribution that is more centrally concentrated and a velocity distribution that is colder than that of dark matter. In addition, if galaxies form near the centers of their original parent halos, they can inherit spatial and velocity bias as a result of incomplete relaxation during the merging of these halos into a larger common halo (Evrard 1987). On the other hand, galaxy mergers happening at the centers of massive halos could reduce galaxy numbers in those regions, thus causing galaxies to be less centrally concentrated than dark matter ($\Delta\gamma > 0$). Also, an $\alpha_v > 1$ velocity bias could arise as a result of preferential destruction or merging of galaxies that have a low velocity.

Following the above steps, we have created a large number of galaxy distributions spanning a wide space of HOD parameters. All of these galaxy distributions come from the same dark halo population and differ only in the HOD. We have calculated a variety of clustering statistics for each of these galaxy distributions in order to test the sensitivity of each statistic to features of the HOD. It would be impractical to show all statistics for all of our HOD models, so in each of the following sections we focus on a subset of models that illustrate the sensitivity of the statistic under examination. Our approach of populating N-body simulations according to an HOD with power-law $N_{\text{avg}}(M)$ is similar to that used by Jing, Mo, & Börner (1998), Jing & Börner (1998), and Jing, Börner & Suto (2002) in their modeling of measurements from the LCRS and PSCz redshift surveys. However, the implementations are different, and our HOD model is substantially more general: we allow variations of M_{min} and the form of $P(N|N_{\text{avg}})$ in addition to variations in α , and we allow the possibility of spatial and velocity biases within halos.

We asserted in § 1 that the HOD formulation can provide a complete statistical description of the bias between galaxies and mass. Underlying this assertion is an implicit assumption that the galaxy content of a halo of virial mass M is statistically independent of that halo’s larger scale environment. This assumption is supported by the N-body simulation results of Lemson & Kauffmann (1999), who find, in agreement with predictions of the excursion set model (Bond et al. 1991), that halos of fixed mass in different environments have similar properties and formation histories, although the halo mass function is itself systematically shifted towards higher mass halos in high density regions. However, the alleged independence of halo histories and large scale environment merits more detailed theoretical investigation. The hypothesis that the HOD formulation is complete will ultimately be tested empirically, by seeing whether an HOD model can reproduce all facets of observed galaxy clustering when applied to a cosmological model consistent with other observational data. Additional implicit assumptions, that all galaxies reside in virialized dark matter halos and that the halo population itself is minimally affected by baryonic physics, seem well justified, though the latter deserves more thorough testing with hydrodynamic simulations². The specific parameterizations adopted here may not capture all of the important features of the true HOD, though they are flexible enough to produce a wide range of results and can easily be generalized to include, e.g., mass dependence of $P(N|N_{\text{avg}})$ or $\Delta\gamma$.

3. The Galaxy Correlation Function

We begin our analysis with the two-point correlation function $\xi_g(r)$, which plays a fundamental role in understanding galaxy clustering because it has been thoroughly studied as a function of galaxy type, color, and luminosity (see Norberg et al. 2001, 2002, Zehavi et al. 2001, and numerous references therein) and because its observed form is remarkably simple. For typical optically selected samples, $\xi_g(r)$ is a power-law $(r/r_0)^{-\gamma}$ for separations $r \lesssim 5h^{-1}\text{Mpc}$, with $r_0 \approx 5 - 6h^{-1}\text{Mpc}$ and $\gamma \approx 1.8$. More luminous galaxies have a larger r_0 and similar γ , while

²The second assumption would not hold if we defined halos at a much higher overdensity, since dissipative collapse of baryon clumps increases their ability to retain surrounding dark matter concentrations within groups and clusters. However, from our point of view, high density halos surrounding individual galaxies are substructure within overdensity 200 halos, so they are described statistically by the HOD itself.

redder or early-type galaxies have a larger γ and a higher clustering amplitude on small scales.

Cosmological N-body simulations show that CDM models do not predict a power-law matter correlation function (e.g., Jenkins et al. 1998), and analytic theory (Hamilton et al. 1991; Peacock & Dodds 1996) implies that the linear theory power spectrum would have to contain a specially tuned feature in order to yield a power-law $\xi(r)$ on non-linear scales. If the primordial power spectrum is a smooth function, as expected on theoretical grounds, it appears that scale-dependent bias must transform the curved matter correlation function into a power-law galaxy correlation function. Remarkably, galaxy distributions predicted by hydrodynamic simulations, by “sub-halo” analyses of high resolution N-body simulations, and by semi-analytic models applied to N-body halos all yield power-law galaxy correlation functions, at least for some reasonable choices of cosmology and galaxy definition parameters (Pearce et al. 1999; Davé et al. 2000; Cen & Ostriker 2000; Yoshikawa et al. 2001; Colín et al. 1999; Kauffmann et al. 1999; Benson et al. 2000; Somerville et al. 2001).

In the context of HOD bias, we would like to know whether a power-law $\xi_g(r)$ follows from some simple and generic property of the HOD, such as a particular galaxy profile in high multiplicity halos, or whether it demands finely tuned parameter choices. We also want to know more generally how the amplitude and shape of $\xi_g(r)$ depend on parameters of the HOD.

3.1. Analytic Discussion

Recent papers (Seljak 2000; Ma & Fry 2000; Scoccimarro et al. 2000; Sheth et al. 2001) present a fairly complete analytic theory of the galaxy correlation function in the halo bias model. The basic idea is to add the “1-halo” term representing galaxy pairs within a single halo to the “2-halo” term representing pairs in separate, spatially correlated halos (as done in a different context by Scherrer & Bertschinger 1991). The full analytic theory becomes simple in the Fourier domain, where convolutions of the halo profile transform into multiplications. As a guide to interpreting our numerical results, we begin with a complementary, more approximate discussion of correlations in real space.

For separations larger than the virial diameter of the largest halos, all pairs must come from galaxies in separate halos. Mo & White (1996) derived an analytic approximation for the bias factor of halos $b_h(M)$ as a function of halo mass M using the Press-Schechter (1974) formalism. Above the characteristic mass M_* in the Press-Schechter mass function, halo formation is enhanced in regions of high background density (and suppressed in underdense regions), so $b_h(M)$ exceeds unity and increases rapidly with increasing mass. Halos with $M < M_*$ are weakly anti-biased because they merge into more massive systems in overdense regions. Jing’s (1998) numerical results yield $b_h(M) \approx 0.7 - 0.8$ for $M \ll M_*$. We assume that the cross-correlation between halos of mass M_1 and M_2 is

$$\xi_{12}(r) = b_h(M_1)b_h(M_2)\xi_m(r), \tag{5}$$

where $\xi_m(r)$ is the mass correlation function.

Consider a halo of mass M_1 . The mean number of excess galaxies in a volume dV at distance r from the halo is obtained by integrating over the differential halo mass function dn/dM (which

has units of number density per unit mass), weighting each halo by the mean number of galaxies $N_{\text{avg}}(M)$ and by the biased correlation factor:

$$N_{\text{excess}} = \int_{M_{\text{min}}}^{\infty} dM_2 \frac{dn}{dM_2} N_{\text{avg}}(M_2) b_h(M_1) b_h(M_2) \xi_m(r) dV. \quad (6)$$

If the number density of galaxies is \bar{n}_g , then the number density of correlated galaxy pairs is

$$\begin{aligned} \frac{1}{2} \bar{n}_g^2 \xi_g(r) dV &= \frac{1}{2} \int_{M_{\text{min}}}^{\infty} dM_1 \frac{dn}{dM_1} N_{\text{avg}}(M_1) N_{\text{excess}} \\ &= \frac{1}{2} \int_{M_{\text{min}}}^{\infty} dM_1 \frac{dn}{dM_1} N_{\text{avg}}(M_1) \int_{M_{\text{min}}}^{\infty} dM_2 \frac{dn}{dM_2} N_{\text{avg}}(M_2) b_h(M_1) b_h(M_2) \xi_m(r) dV \\ &= \frac{1}{2} \xi_m(r) dV \int_{M_{\text{min}}}^{\infty} dM_1 \frac{dn}{dM_1} N_{\text{avg}}(M_1) b_h(M_1) \int_{M_{\text{min}}}^{\infty} dM_2 \frac{dn}{dM_2} N_{\text{avg}}(M_2) b_h(M_2) \end{aligned} \quad (7)$$

where the factor of 1/2 corrects for double counting of each pair. Thus, at large separations we expect

$$\xi_g(r) = b^2 \xi_m(r), \quad b = \bar{n}_g^{-1} \int_{M_{\text{min}}}^{\infty} dM \frac{dn}{dM} N_{\text{avg}}(M) b_h(M), \quad (8)$$

and the galaxy bias is just the weighted value of the halo bias.

On small scales, the correlation function is dominated by the 1-halo term representing galaxy pairs that reside in the same halo. The total number density of such pairs is

$$n_{\text{pair,1h}} = \int_{M_{\text{min}}}^{\infty} dM \frac{dn}{dM} \frac{\langle N(N-1) \rangle_M}{2} \approx \frac{\bar{n}_g^2}{2} \int_0^{2R_{\text{max}}} \xi_g(r) 4\pi r^2 dr, \quad (9)$$

where $\langle N(N-1) \rangle_M = \int_0^{\infty} dN P(N|M) N(N-1)$ and the second equality would be exact if *all* correlated pairs out to the maximum halo virial diameter $2R_{\text{max}}$ came from the 1-halo contribution. (Bullock et al. 2002 apply a similar argument to Lyman-break galaxy clustering.) More generally, we can write

$$\frac{\bar{n}_g^2}{2} \int_0^r \xi_{1h}(r) 4\pi r^2 dr = \int_{M_{\text{min}}}^{\infty} dM \frac{dn}{dM} \frac{\langle N(N-1) \rangle_M}{2} F\left(\frac{r}{2R_{\text{vir}}}\right), \quad (10)$$

where $\xi_{1h}(r)$ refers specifically to the correlation function associated with galaxy pairs in the same halo and the function $F(r/2R_{\text{vir}})$ represents the average fraction of galaxy pairs in halos of mass M that have separation less than r (a fraction $r/2R_{\text{vir}}$ of the virial diameter). Since the only r dependence on the r.h.s. of equation (10) appears in $F(r/2R_{\text{vir}})$, we can differentiate with respect to r to find

$$2\pi r^2 \bar{n}_g^2 \xi_{1h}(r) = \int_{M_{\text{min}}}^{\infty} dM \frac{dn}{dM} \frac{\langle N(N-1) \rangle_M}{2} \frac{1}{2R_{\text{vir}}(M)} F'\left(\frac{r}{2R_{\text{vir}}}\right). \quad (11)$$

While the large scale bias factor (eq. [8]) depends only on $N_{\text{avg}}(M)$, the correlation function in the 1-halo regime depends on the 2nd factorial moment $\langle N(N-1) \rangle_M$, and hence on the form of $P(N|N_{\text{avg}})$. A Poisson distribution of mean $\langle N \rangle$ has variance $\langle N^2 \rangle - \langle N \rangle^2 = \langle N \rangle$, so $\langle N(N-1) \rangle_M = \langle N^2 \rangle_M - \langle N \rangle_M = \langle N \rangle_M^2 = N_{\text{avg}}^2(M)$. Our Average distribution, on the other hand, has $\langle N(N-1) \rangle_M = N_{\text{avg}}^2(M) - N_{\text{avg}}(M)$ (even when $N_{\text{avg}}(M)$ is not an integer), which can be substantially lower than the Poisson value when $N_{\text{avg}}(M)$ is small. The small-scale galaxy

correlation function also depends on the halo profile through $F(r/2R_{\text{vir}})$ — more concentrated halos have a larger fraction of pairs at small r , boosting the small-scale correlations at the expense of slightly larger separations.

Figure 2a shows the cumulative pair fraction $F(r/2R_{\text{vir}})$ for one of our HOD models. We take the virial radius of each halo to be

$$R_{\text{vir}} = \left(\frac{3M}{800\pi\bar{\rho}_m} \right)^{1/3}, \quad (12)$$

where $\bar{\rho}_m$ is the mean mass density and M is the halo mass. We measure the separation distribution from the numerically realized galaxy distribution and average over all halos (solid line), as well as halos in narrower mass bins. With separations scaled to virial diameters, the function $F(r/2R_{\text{vir}})$ is nearly independent of halo mass, though there is a slight trend of higher concentration at lower mass, as expected from N-body studies of halo profiles (Navarro, Frenk, & White 1997; Bullock et al. 2001). All pairs have separations less than $2R_{\text{vir}}$, and about half the pairs have separations less than $R_{\text{vir}}/2$.

The halo-averaged form of $F(r/2R_{\text{vir}})$ should be virtually independent of $P(N|M)$, since the cumulative pair distribution is insensitive to halo mass. However, $F(r/2R_{\text{vir}})$ is sensitive to the relative distribution of galaxies and dark matter within halos. Figure 2b shows $F(r/2R_{\text{vir}})$ averaged over all halos for HOD models in which the galaxies are more centrally concentrated ($\Delta\gamma = -1$; short-dashed curve) or less centrally concentrated ($\Delta\gamma = +1$; long-dashed curve) than the dark matter. As expected, $F(r/2R_{\text{vir}})$ rises faster for more central concentration, since most pairs lie close to the halo center. The dotted curve in Figure 2b shows a model with $\Delta\gamma = 0$ but a central galaxy in every halo (for which $N > 0$), which yields a result intermediate between the $\Delta\gamma = 0$ and $\Delta\gamma = -1$ models. In this case, unlike all the others, we expect $F(r/2R_{\text{vir}})$ to depend strongly on halo mass, since the central galaxy contributes to a significant fraction of pairs in low multiplicity halos but not in high multiplicity halos. For central galaxy models, it is more informative to rewrite equation (10) in the form

$$\frac{\bar{n}_g^2}{2} \int_0^r \xi_{1h}(r) 4\pi r^2 dr = \int_{M_{\text{min}}}^{\infty} dM \frac{dn}{dM} \left[\frac{\langle (N-1)(N-2) \rangle_M}{2} F\left(\frac{r}{2R_{\text{vir}}}\right) + \langle N-1 \rangle_M F_c\left(\frac{r}{2R_{\text{vir}}}\right) \right], \quad (13)$$

where $F(r/2R_{\text{vir}})$ now refers only to pairs that do *not* involve the central galaxy and $F_c(r/2R_{\text{vir}})$, which is simply the cumulative halo profile itself, refers only to pairs that include the central galaxy. Here $F(r/2R_{\text{vir}})$ and $F_c(r/2R_{\text{vir}})$ should both be approximately independent of halo mass, but F_c rises faster than F , and the relative weight of the two terms depends on N . We see from equation (13) that a central galaxy should be important only on scales where low multiplicity halos make a significant contribution to the correlation function.

3.2. Numerical Results

Figures 3-6 show correlation functions for galaxy distributions created using a variety of HOD models that all have a power-law $N_{\text{avg}}(M)$ (as defined in eq. [1]). Each figure demonstrates the dependence of $\xi_g(r)$ on a particular feature of the HOD by displaying models that differ only in

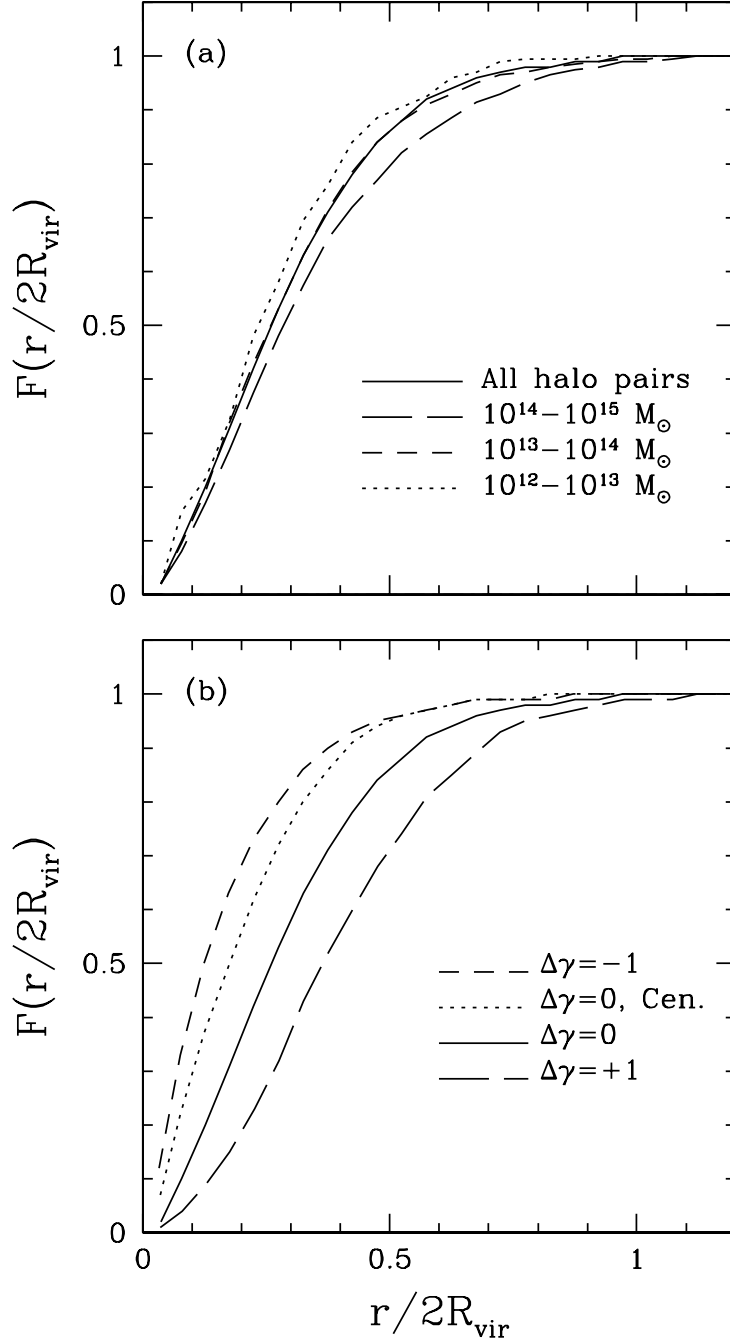


Fig. 2.— The cumulative fraction of galaxy pairs within halos as a function of separation, $F(r/2R_{\text{vir}})$, as defined in equation (10). Panel (a) shows $F(r/2R_{\text{vir}})$ for halos of different mass ranges in the case of an HOD model with $\alpha = 0.5$, $M_{\text{min}} = 2.8 \times 10^{11} h^{-1} M_{\odot}$, and an Average $P(N|N_{\text{avg}})$. Panel (b) shows $F(r/2R_{\text{vir}})$ averaged over the halo population for HOD models with the same $P(N|M)$ as panel (a), but with variations of the galaxy spatial distribution within halos. There are three HOD prescriptions with different values of $\Delta\gamma$ and one where a galaxy is forced to lie at the center of each halo for which $N > 0$.

that feature. We note that models with different values of M_{\min} or α also have different values of M_1 , since this parameter is used to fix the mean number density of galaxies to $\bar{n}_g = 0.01h^3\text{Mpc}^{-3}$. For purpose of comparison, each figure also shows the dark matter correlation function and the real space $\xi_g(r)$ inferred by Baugh (1996) from angular clustering in the APM galaxy survey (Maddox et al. 1990).

Figure 3 shows the effect on $\xi_g(r)$ of varying M_{\min} . On large scales, only the amplitude of the correlation function is affected, with higher values of M_{\min} having a slightly larger amplitude. Since the number density of galaxies remains fixed, the result of increasing M_{\min} is to remove galaxies from low mass halos and redistribute them into halos of mass $M > M_{\min}$. In terms of equation (8), this means that weight is taken away from the lower mass halos that have a smaller halo bias factor b_h , so the galaxy bias b increases. On scales $r \lesssim 1h^{-1}\text{Mpc}$, both the shape and amplitude of the correlation function are very sensitive to M_{\min} , with higher values of M_{\min} producing a steeper slope and higher amplitude of $\xi_g(r)$. Figure 4 shows the effect of varying α . Qualitatively, increasing α has an effect similar to that of increasing M_{\min} , since both changes boost the fraction of galaxies in high mass, positively biased halos. However, the changes to the shape of $\xi_g(r)$ are different in detail. We will return to a discussion of these effects shortly.

Figure 5 shows the effect of varying $P(N|N_{\text{avg}})$ while keeping $N_{\text{avg}}(M)$ fixed. It is clear that the impact on large scales is negligible, while on small scales the amplitude of $\xi_g(r)$ increases with increasing width of the $P(N|N_{\text{avg}})$ distribution. This behavior is expected because the large-scale bias factor (eq. [8]) depends only on $N_{\text{avg}}(M)$, while $\xi_{1h}(r)$ depends on $\langle N(N-1) \rangle_M$ (eq. [11]), which is larger for wider distributions that have the same N_{avg} . The impact of $P(N|N_{\text{avg}})$ grows at smaller scales, where low mass (and hence low multiplicity) halos contribute to $\xi_{1h}(r)$.

Figure 6 shows the effect of varying the distribution of galaxies within halos, while keeping $P(N|M)$ fixed. The plot shows four models: one where galaxies are more centrally concentrated than the dark matter within halos ($\Delta\gamma = -1$), one where galaxies are less concentrated within halos ($\Delta\gamma = +1$), one where galaxies trace the dark matter within halos ($\Delta\gamma = 0$), and a model where a galaxy is forced to lie at the center of every halo for which $N > 0$. The effects of varying the spatial distribution of galaxies within halos are confined to small scales. As expected, the model where galaxies are more centrally concentrated within halos has a correlation function that is amplified on very small scales and depressed on scales corresponding to the virial size of halos. The model where galaxies are less centrally concentrated exhibits the opposite behavior. Forcing halos to have central galaxies only affects $\xi_g(r)$ by increasing it slightly on the smallest scales, as we expect from equation (13). Relative to changes in $P(N|M)$, the effect of changing the distribution of galaxies within halos is small, at least on the scales $r > 0.1h^{-1}\text{Mpc}$ considered here.

To better understand the behavior in Figures 3-6, it is helpful to decompose $\xi_{1h}(r)$ into contributions from halos in different mass ranges. Figure 7 presents such a decomposition for several HOD models (see figure 2 of Seljak 2000 for a similar decomposition in the Fourier domain). Figure 7a shows a power-law $N_{\text{avg}}(M)$ model with $\alpha = 0.5$ and $M_{\min} = 2.8 \times 10^{11}h^{-1}M_{\odot}$ that has a Poisson $P(N|N_{\text{avg}})$. The thick solid curve shows the correlation function for this galaxy distribution (also seen in Figures 3-6), and the thin solid curve represents the contribution from galaxy pairs within the same halo (the 1-halo term). As expected, the 1-halo term dominates on scales up to the virial size of typical halos and drops off quickly at larger scales. The remaining

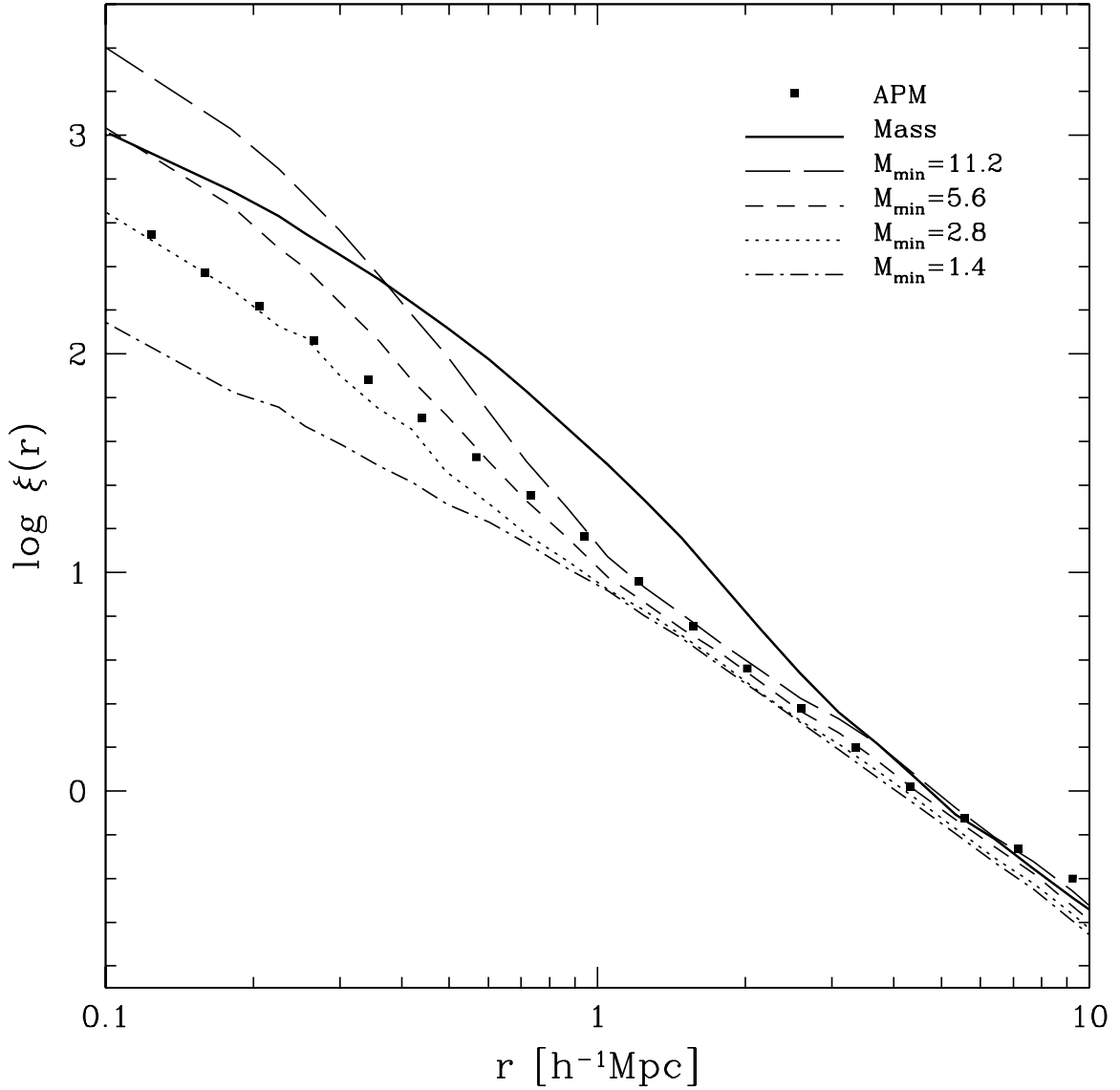


Fig. 3.— Influence of M_{\min} on the galaxy correlation function. Curves show galaxy correlation functions for HOD models with a power-law $N_{\text{avg}}(M)$, $\alpha = 0.5$, Average $P(N|N_{\text{avg}})$, and different values of M_{\min} , which are listed in the legend in units of $10^{11} h^{-1} M_{\odot}$. The solid curve shows the mass correlation function, and points show the correlation function measured from the APM galaxy survey (Baugh 1996).

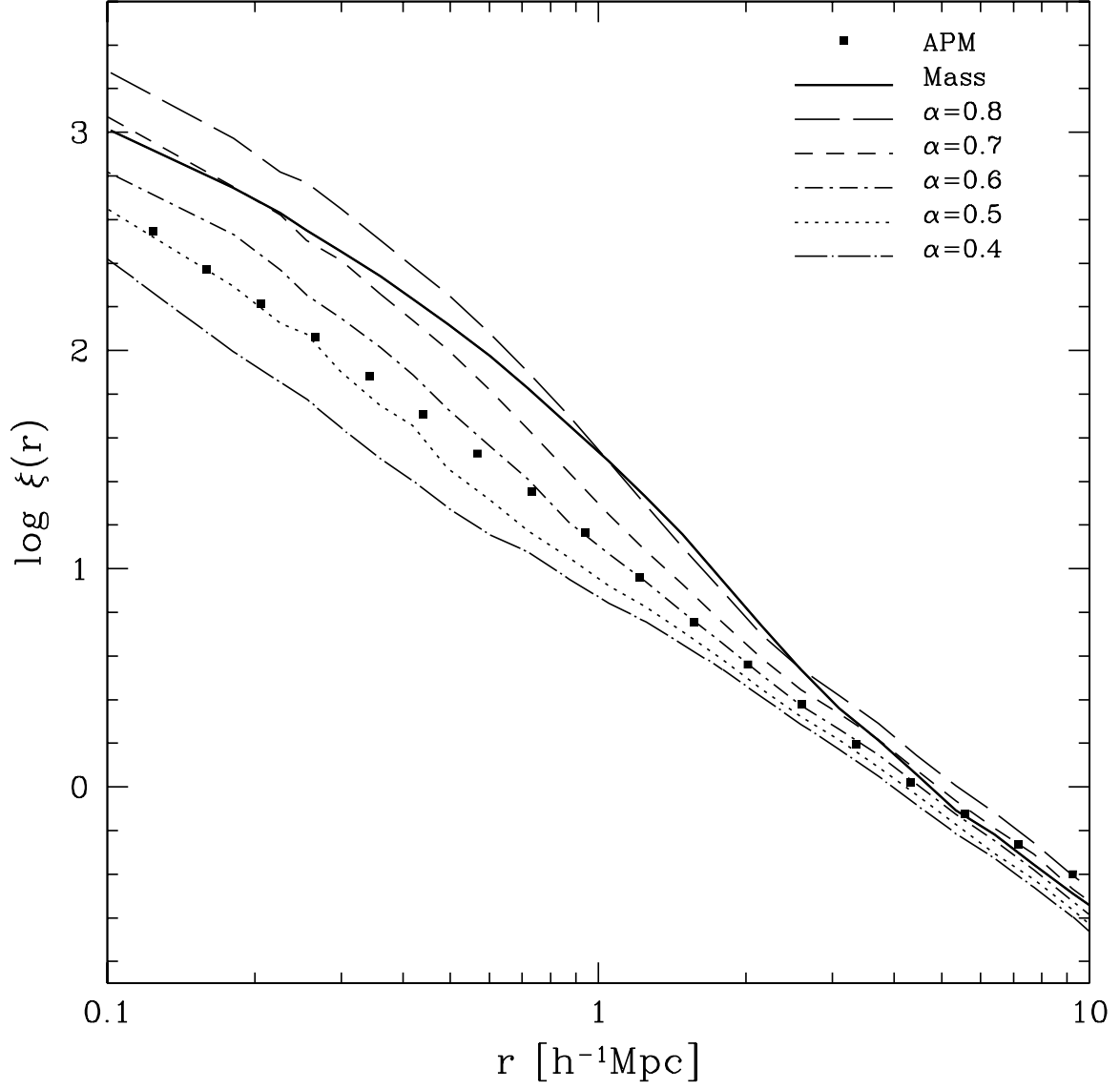


Fig. 4.— Influence of α on the galaxy correlation function. Curves show galaxy correlation functions for HOD models with a power-law $N_{\text{avg}}(M)$, $M_{\text{min}} = 2.8 \times 10^{11} h^{-1} M_{\odot}$, Average $P(N|N_{\text{avg}})$, and different values of α , which are listed in the legend.

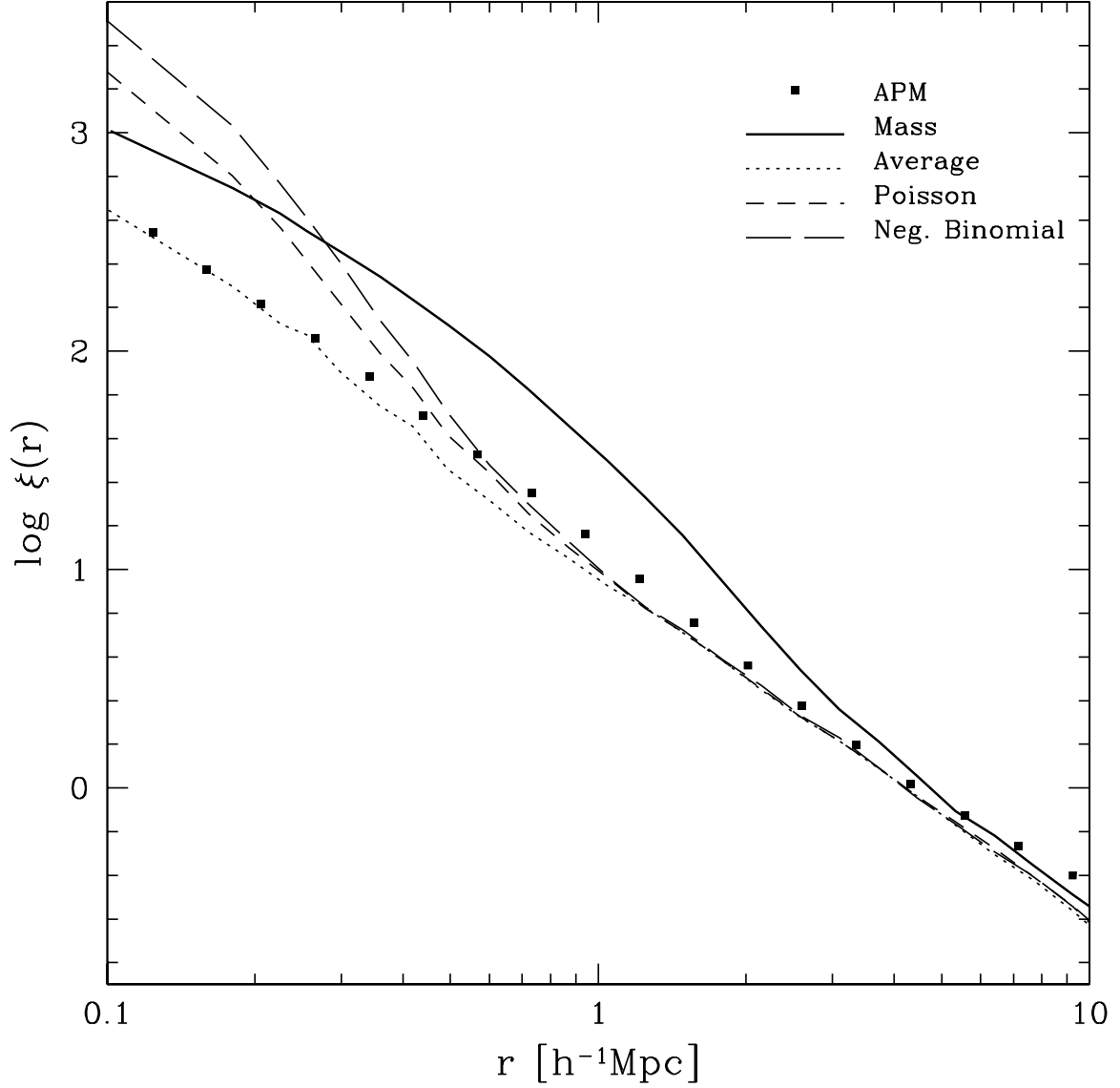


Fig. 5.— Influence of $P(N|N_{\text{avg}})$ on the galaxy correlation function. Curves show galaxy correlation functions for HOD models with a power-law $N_{\text{avg}}(M)$, $M_{\text{min}} = 2.8 \times 10^{11} h^{-1} M_{\odot}$, $\alpha = 0.5$, and different forms of $P(N|N_{\text{avg}})$, which are listed in the legend.

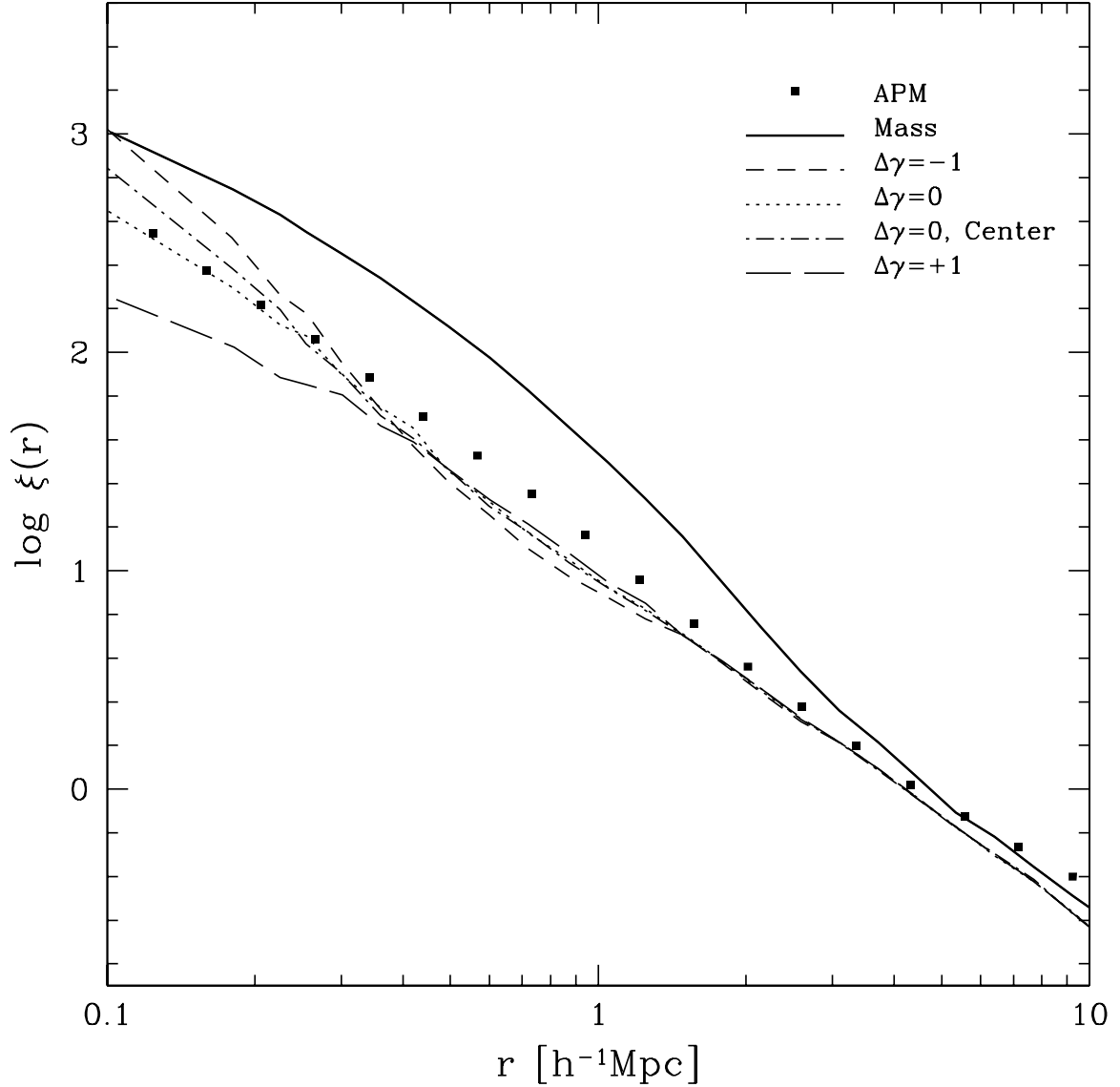


Fig. 6.— Influence of the galaxy profiles within halos on the galaxy correlation function. As in Figs. 3-5, the dotted curve shows $\xi_g(r)$ for a model with $M_{\min} = 2.8 \times 10^{11} h^{-1} M_{\odot}$, $\alpha = 0.5$, Average $P(N|N_{\text{avg}})$, and galaxies tracing dark matter within halos. Short-dashed and long-dashed curves show results for models in which galaxy profiles are respectively more concentrated or less concentrated than dark matter profiles ($\Delta\gamma = -1$ or $\Delta\gamma = +1$, see eq. [3]). The dot-dashed curve shows a model in which the first galaxy of each halo lies at the halo center and subsequent galaxies have the same profile as the dark matter.

four curves show the contribution to the 1-halo term from halos with $M = 10^{11} - 10^{12}h^{-1}M_{\odot}$ (dot-dashed curve), $10^{12} - 10^{13}h^{-1}M_{\odot}$ (dotted curve), $10^{13} - 10^{14}h^{-1}M_{\odot}$ (short dashed curve), and $10^{14} - 10^{15}h^{-1}M_{\odot}$ (long dashed curve). Each curve is highest at the smallest scales and drops off at larger scales. However, the curves for high mass halos start at lower amplitude and extend to larger r , since pairs are spread over a larger virial volume. Consequently, galaxy pairs in low mass halos dominate $\xi_g(r)$ at very small scales, while galaxy pairs in high mass halos dominate $\xi_g(r)$ on scales corresponding to their virial radii.

Figure 7b shows the effect of doubling M_{\min} while keeping all other HOD parameters fixed. Since \bar{n}_g remains constant, galaxies that were previously in low mass halos are redistributed to halos above the new value of M_{\min} . In Figure 7b, the contributions to $\xi_g(r)$ from galaxy pairs in the three highest halo mass bins uniformly increase. The lowest mass bin ($10^{11} - 10^{12}h^{-1}M_{\odot}$) behaves differently because M_{\min} lies within it, causing some of the halos in this bin to lose pairs and others to gain pairs, resulting in no net change to the contribution from that bin. Doubling M_{\min} slightly increases the large scale bias factor, but the impact on $\xi_{1h}(r)$ is much greater, so the overall effect is to steepen $\xi_g(r)$.

Figure 7c shows the effect of increasing α while keeping all other HOD parameters fixed. The contribution of the high mass halos increases dramatically, whereas the contribution of the lowest mass halos drops. We can thus understand why increasing α has a “smoother” effect on $\xi_g(r)$ than increasing M_{\min} , producing less distortion in the overall shape. First, increasing α has a larger impact on the large scale bias factor, so the 1-halo and 2-halo terms rise more nearly in step. Second, increasing α flattens the shape of $\xi_{1h}(r)$ as it increases its amplitude, by redistributing pairs to halos with larger virial radii. The shape of $\xi_{1h}(r)$ therefore stays closer to the extrapolated shape of $\xi_g(r)$ from large scales.

Figure 7d shows the effect of changing the $P(N|N_{\text{avg}})$ distribution from Poisson to Average. The narrower distribution yields a smaller value of $\langle N(N-1) \rangle_M$ for the same $N_{\text{avg}}(M)$, especially in low multiplicity halos. As a result, the 1-halo contribution to $\xi_g(r)$ drops dramatically at small scales, $r \sim 0.1 - 0.4h^{-1}\text{Mpc}$. The contribution of halos with $M = 10^{11} - 10^{12}h^{-1}M_{\odot}$ disappears completely because M_1 exceeds $10^{12}h^{-1}M_{\odot}$, so with an Average $P(N|N_{\text{avg}})$ no halo in this mass range can have more than one galaxy. The suppression of pairs in low mass halos allows $\xi_g(r)$ to continue as a power law down to $r = 0.1h^{-1}\text{Mpc}$.

The last two panels of Figure 7 show the effect of changing the spatial distribution of galaxies within halos. The HOD models have the same $P(N|M)$ as the model shown in Figure 7d, so the number of pairs in halos of each mass range is the same as before. However, the radial separations of these pairs are squeezed towards smaller r for $\Delta\gamma = -1$ (Fig. 7e) and stretched towards larger r for $\Delta\gamma = +1$ (Fig. 7f), making the correlation function steeper or shallower at small scales. The shapes of these curves are directly related to the function $F(r/2R_{\text{vir}})$, defined in equation (10) and plotted in Figure 2, which depends on the radial profile of galaxies within halos.

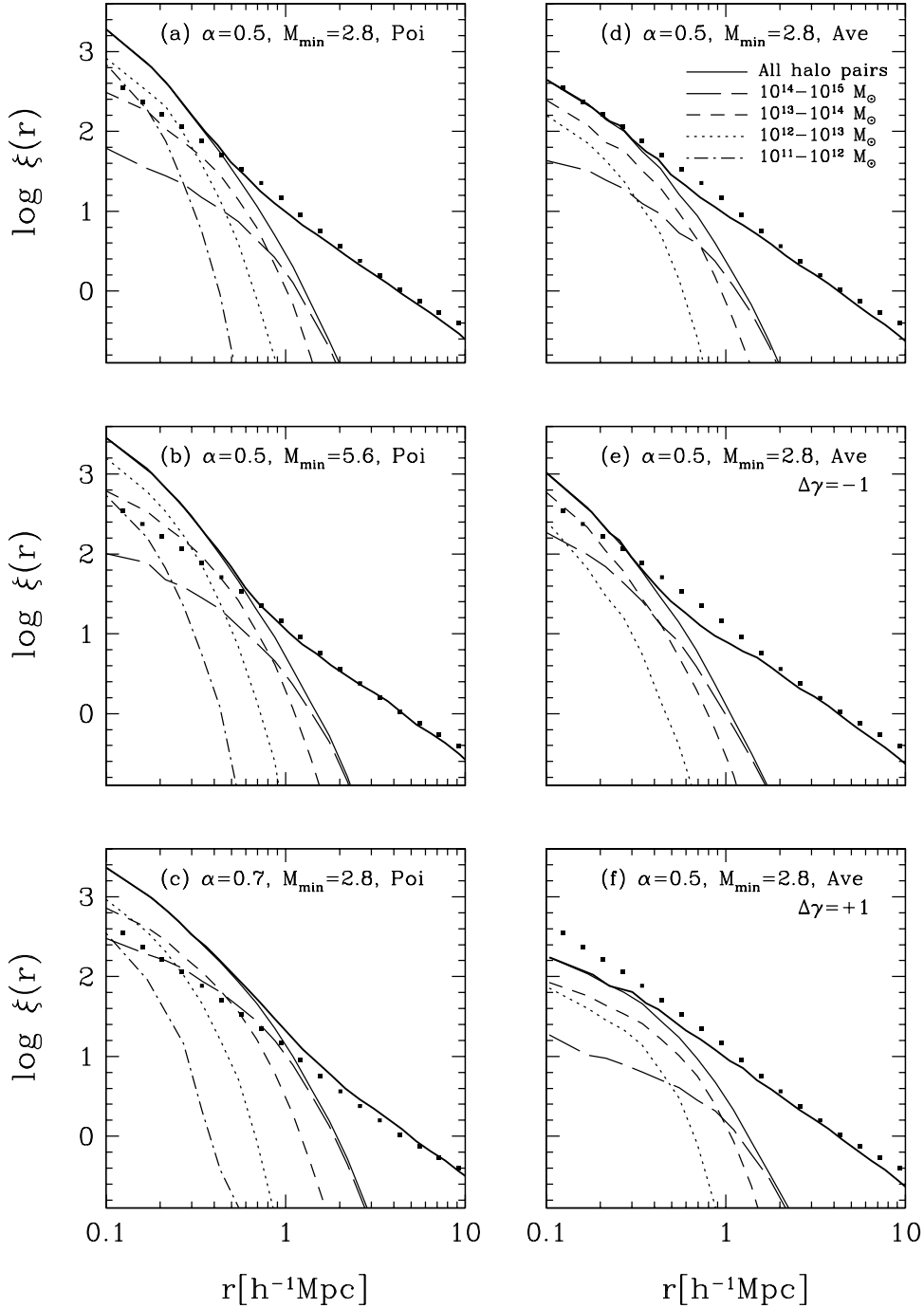


Fig. 7.— Contributions to the galaxy correlation function from pairs within halos of different mass ranges. Each panel represents a particular HOD model. The models are specified at the top of each panel, where M_{\min} is given in units of $10^{11}h^{-1}M_{\odot}$, and Poi and Ave represent Poisson and Average $P(N|N_{\text{avg}})$ distributions, respectively. Each panel shows the full galaxy correlation function (thick solid curve), the correlation function including only galaxy pairs that lie within the same halos (thin solid curve), and the contribution to $\xi_g(r)$ from pairs that lie only within halos of a certain mass range (remaining 4 curves). The mass ranges are indicated in panel (d). Also shown, for comparison, is the APM galaxy correlation function (squares).

3.3. Understanding the Observed Correlation Function

In light of these results, what do we make of the observed power-law form of $\xi_g(r)$? One obvious conclusion is that a power-law $\xi_g(r)$ is not a generic prediction of HOD models applied to a Λ CDM cosmology; most of the models in Figures 3-6 show clear departures from a power law. We can understand this behavior by considering Figure 7 and the analytic discussion in § 3.1. On large scales, the shape of $\xi_g(r)$ is the same as the shape of $\xi_m(r)$, and the amplitude of $\xi_g(r)$ is determined by the $\xi_m(r)$ amplitude and the bias factor b (eq. [8]). On small scales, typically $r \lesssim 0.5h^{-1}\text{Mpc}$ (Fig. 7), the 1-halo term dominates. In this regime, the shape and amplitude of $\xi_g(r)$ are governed by equation (11), which involves $\langle N(N-1) \rangle_M$ rather than $N_{\text{avg}}(M)$ and does not involve $\xi_m(r)$ explicitly at all (though ξ_m and dn/dM are connected indirectly). Achieving a power-law $\xi_g(r)$ requires that the amplitude of $\xi_{1\text{h}}(r)$ place it on the extension of $b^2\xi_m(r)$, and it requires that the distribution of pair counts as a function of halo mass yield a power law of the same slope in the 1-halo regime.

Suppose we have a model that achieves this somewhat delicate balancing act, such as the $\alpha = 0.5$, $M_{\text{min}} = 2.8 \times 10^{11}h^{-1}M_{\odot}$, Average model. Changing $P(N|N_{\text{avg}})$ has no effect at large scales, since b depends only on $N_{\text{avg}}(M)$, but it changes the amplitude and shape of $\xi_{1\text{h}}(r)$, destroying the power-law behavior. Changing M_{min} , with a compensating change in M_1 to keep \bar{n}_g fixed, has different effects in the 1-halo and 2-halo regimes. If $M_{\text{min}} \ll M_*$, then the impact on b will generally be modest. However, raising M_{min} redistributes pairs that were previously in low mass halos to high mass halos, substantially increasing the 1-halo contribution of these halos and destroying the previous balance. Changing α has a more complicated effect than changing M_{min} because it can significantly alter b and because it changes both the amplitude and shape of $\xi_{1\text{h}}(r)$. However, these three changes generally do not work in a way that preserves a power law. Finally, Figure 6 shows that changes to the halo profile have relatively little leverage for modifying a non-power-law $\xi_g(r)$ into a power law. Even the rather drastic profile changes represented by $\Delta\gamma = \pm 1$ only alter $\xi_g(r)$ on fairly small scales. A central galaxy restriction affects still smaller scales, since central galaxy pairs only matter in low- N halos with small virial radii. Central galaxies probably have an important influence on $\xi_g(r)$ at $r < 100h^{-1}\text{kpc}$, but they are not fundamental to understanding the $0.1 - 0.5h^{-1}\text{Mpc}$ regime. More generally, adopting the “right” halo profile can never compensate for having the “wrong” $P(N|M)$.

To roughly quantify the “difficulty” of obtaining a power-law $\xi_g(r)$, we have carried out a systematic survey of HOD models with power-law $N_{\text{avg}}(M)$, Average or Poisson $P(N|N_{\text{avg}})$, and M_1 chosen in all cases to yield $\bar{n}_g = 0.01h^3\text{Mpc}^{-3}$. Figure 8 summarizes the results for a representative sample of models. Using an unweighted least-squares fit in the range $0.1h^{-1}\text{Mpc} < r < 10h^{-1}\text{Mpc}$, we determine the best-fit power-law parameters r_0 and γ for each model correlation function. As expected, the slope γ steepens with increasing M_{min} or α , since these changes amplify the 1-halo term relative to the 2-halo term. The influence of M_{min} is stronger in Average models than in Poisson models (compare Figs. 8e and 8f) because $\langle N(N-1) \rangle$ cuts off more sharply near M_{min} in an Average model. The correlation length r_0 generally increases with increasing M_{min} or α (Figs. 8c and 8d). However, the dependence on M_{min} is weak when M_{min} is small, because the bias factor integral (eq. [8]) remains dominated by low mass halos. The dependence becomes stronger when M_{min} becomes large enough to significantly increase the

fraction of galaxies in halos with $M > M_*$ (and thus $b_h > 1$). Increasing α , by contrast, always increases the relative numbers of galaxies in more biased halos, and the dependence of r_0 on α is fairly steady.

The top panels of Figure 8 show the χ^2 of the power-law fit. Since we used an unweighted fit, we scale the values of χ^2 by a constant factor so that models with visually acceptable power-law correlation functions have $\chi^2 \leq 1$. (If we were trying to match specific observational data with known error bars, we would follow a more rigorous methodology, but that is not our purpose here.) As one would guess from the sampling of models shown in Figures 3-6, only a small region of this HOD parameter space — Average models with $M_{\min} \lesssim 3 \times 10^{11} h^{-1} \text{Mpc}$ and $\alpha \approx 0.4 - 0.6$ — yields power-law correlation functions. In more general terms, achieving a power-law $\xi_g(r)$ requires that a large fraction of galaxies reside in low mass (and low multiplicity) halos; otherwise the 1-halo portion of $\xi_g(r)$ is too high relative to the 2-halo portion. Average models are more successful than Poisson models because they suppress $\langle N(N-1) \rangle$ in low mass halos and thus prevent a steepening of $\xi_g(r)$ at small r . Values of M_{\min} smaller than our resolution threshold ($1.4 \times 10^{11} h^{-1} M_\odot$) might allow a Poisson model to work, but we are modeling the population of galaxies with $L > 0.5L_*$, and a lower value of M_{\min} would force some of these galaxies into very low mass halos, contradicting constraints from the Tully-Fisher (1977) relation. In addition, the bottom panels of Figure 8 show that a small M_{\min} implies a large M_1 ($M_1 \geq 3 \times 10^{12} h^{-1} M_\odot$ for $M_{\min} \leq 2.8 \times 10^{11} h^{-1} M_\odot$). Since halos of mass $\sim 2M_1$ still have a significant probability of hosting a single galaxy, a high M_1 may force some low luminosity galaxies into fairly massive halos, again running afoul of Tully-Fisher constraints.

This discussion suggests that the power-law $N_{\text{avg}}(M)$ parameter space may itself be too restrictive, since it ties the fraction of galaxies in low mass halos directly to the relative distribution of galaxies among high mass halos (which affects the large scale bias and the larger separation end of the 1-halo regime). We have also examined the family of broken power-law models defined by equation (2), which (for $\alpha < \beta$) allow more galaxies in low mass halos for a given slope in the high mass regime. With a break point at $M_{\text{crit}} = 10^{13} h^{-1} \text{Mpc}$, we find acceptable correlation functions for some Average models with $M_{\min} \sim 3 - 5 \times 10^{11} h^{-1} M_\odot$, $\alpha \sim 0.2 - 0.3$, $\beta \sim 0.6 - 0.8$, and for some Poisson models with $M_{\min} \sim 1 - 2 \times 10^{11} h^{-1} M_\odot$, $\alpha \sim 0.4 - 0.5$, $\beta \sim 0.8 - 0.9$. The solid line in Figure 9 shows the correlation function of one of these models, which matches the APM results quite well. Even with broken power-law $N_{\text{avg}}(M)$, acceptable Poisson models require low values of M_{\min} . To the extent that such low values are implausible, we concur with arguments in previous papers (Benson et al. 2000; Seljak 2000; Peacock & Smith 2000; Scoccimarro et al. 2000) that sub-Poisson number fluctuations in low multiplicity halos are important in explaining the observed form of $\xi_g(r)$.

At scales $r \lesssim 5h^{-1} \text{Mpc}$, peculiar velocities severely distort the shape of the correlation function in redshift space. Observational evidence for a power-law $\xi_g(r)$ therefore rests on measurements of the angular correlation function $w(\theta)$ or the projected redshift-space correlation function $w_p(r_p)$ (see, e.g., Baugh 1996; Norberg et al. 2001; Zehavi et al. 2001). While a power-law $\xi_g(r)$ projects into a power-law $w(\theta)$ or $w_p(r_p)$ (Limber 1954; Davis & Peebles 1983), one might worry that projection could wash out departures from a power-law $\xi_g(r)$. We have checked that this is not the case by computing $w_p(r_p)$ for many of our HOD models. We find that any models that predict visually evident departures from a power-law $\xi_g(r)$ also predict visually evident

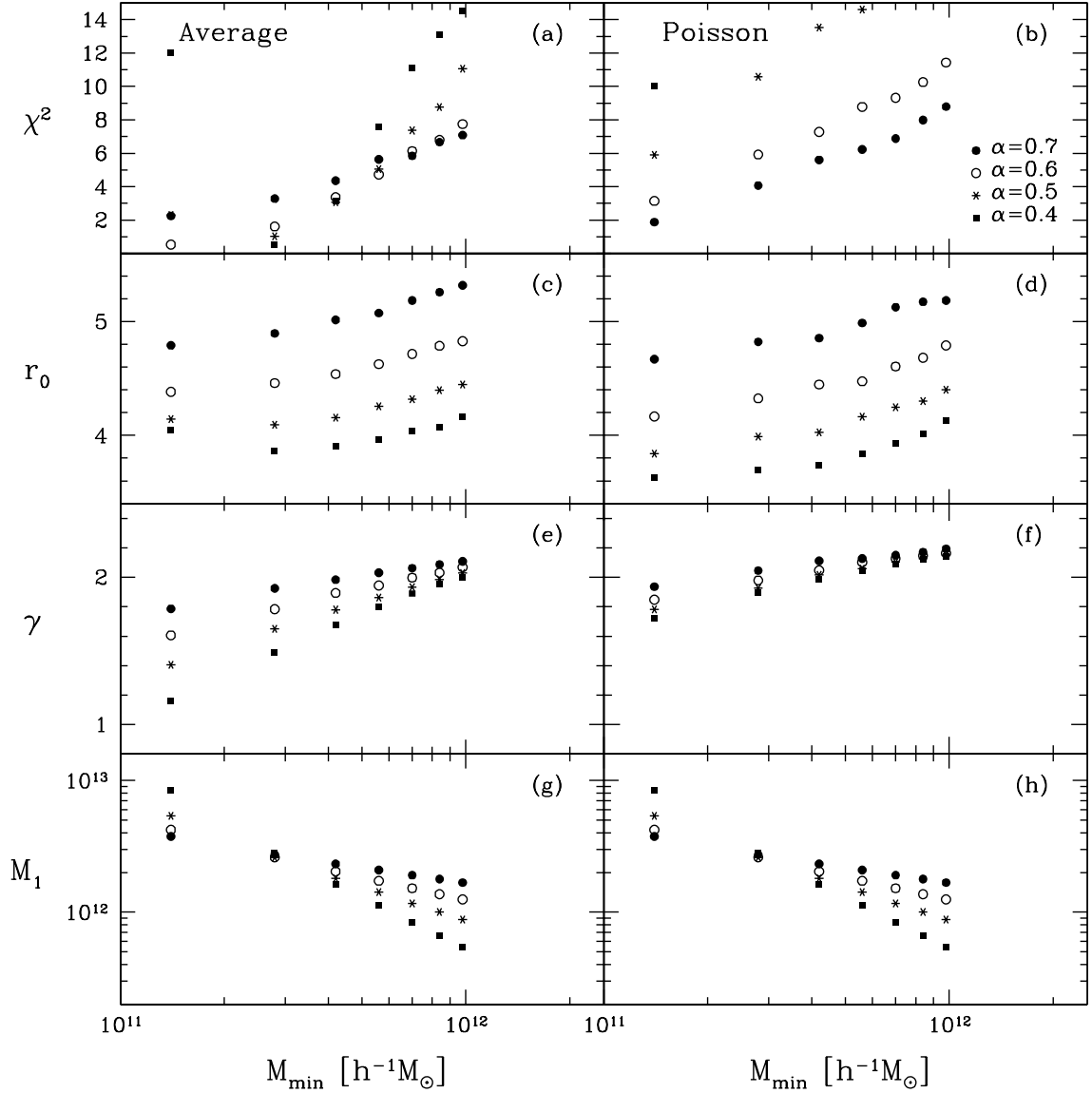


Fig. 8.— Power-law fits to a sample of HOD model galaxy correlation functions. Each point corresponds to a specific $P(N|M)$, where the x-axis shows M_{\min} and the type of point represents α as shown in panel (b). The left-hand-side and right-hand-side panels contain models with an Average and Poisson $P(N|N_{\text{avg}})$, respectively. Panels (a) and (b) show values of χ^2 from these fits. Since the fits are unweighted, the values of χ^2 have been scaled so that models with visually acceptable power-law correlation functions have $\chi^2 < 1$. Panels (c) and (d) show the best-fit values of the correlation length r_0 . Panels (e) and (f) show the best-fit values of the slope γ . Panels (g) and (h) show the value of M_1 for each model, chosen to yield a galaxy distribution of fixed number density $\bar{n}_g = 0.01 h^3 \text{Mpc}^{-3}$.

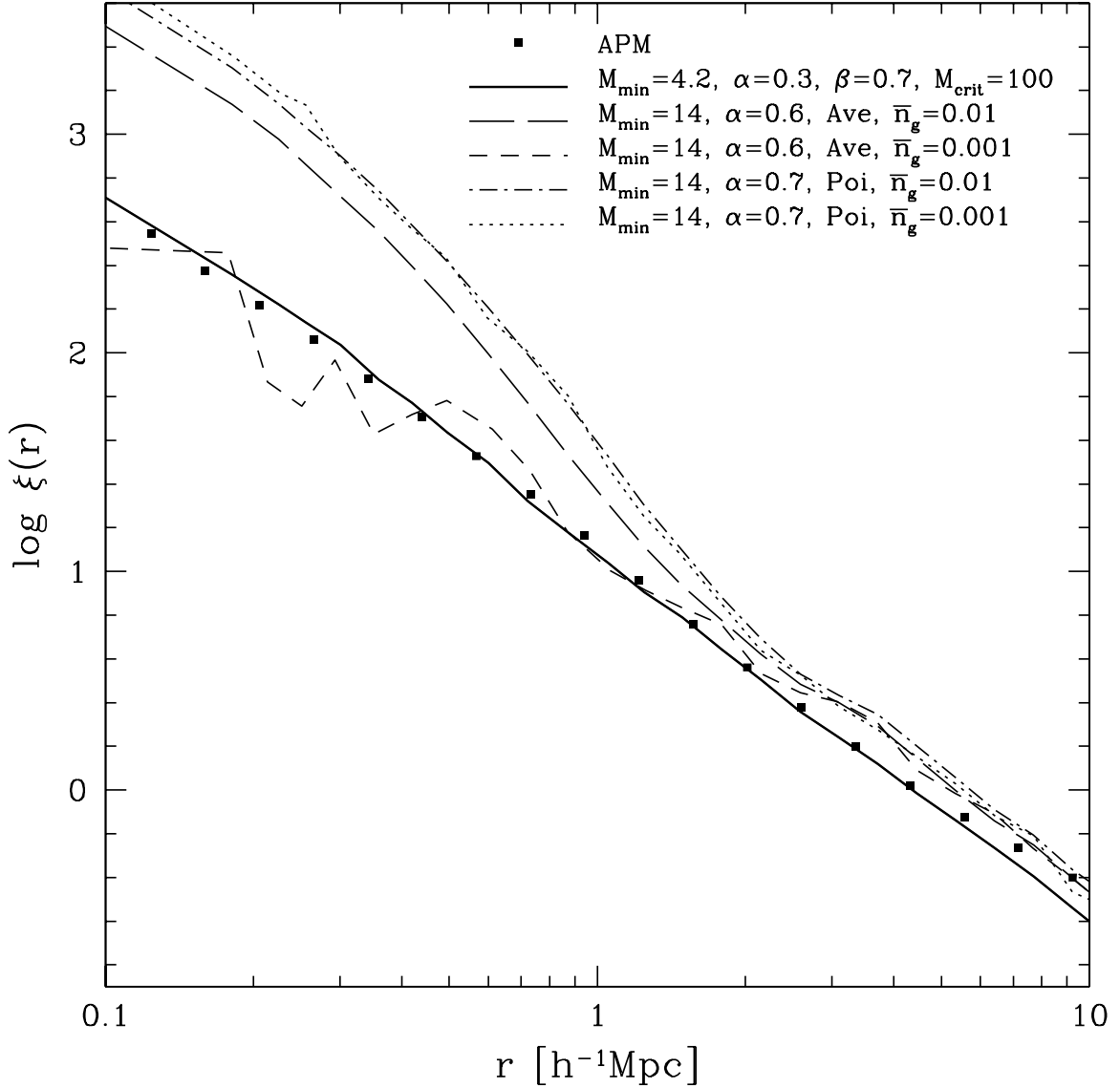


Fig. 9.— Real-space correlation functions of galaxy distributions for different HOD prescriptions. As indicated in the legend, there is one HOD model with a broken power-law $N_{\text{avg}}(M)$, and four power-law $N_{\text{avg}}(M)$ models with two values of the galaxy space density \bar{n}_g (see text for further discussion). Values of M_{min} and M_{crit} are given in units of $10^{11}h^{-1}M_{\odot}$, and values of \bar{n}_g are in units of $h^3\text{Mpc}^{-3}$.

departures from a power-law $w_p(r_p)$.

At higher luminosities, the observed $\xi_g(r)$ has a higher amplitude and a similar power-law slope. The higher amplitude is not surprising, since M_{\min} should be higher for more luminous galaxies. Retaining the power-law form of $\xi_g(r)$, however, requires that other HOD parameters adjust in the right way. A higher luminosity threshold also implies a lower galaxy space density \bar{n}_g , so in general we expect both M_{\min} and M_1 to be higher for more luminous samples. The influence of M_1 on $\xi_g(r)$ depends crucially on the form of the probability distribution $P(N|N_{\text{avg}})$. For a Poisson model, raising M_1 is equivalent to randomly sampling the galaxy population, which does not alter the correlation function. For an Average model, on the other hand, raising M_1 reduces $\langle N(N-1) \rangle$ by a factor larger than \bar{n}_g^2 , thus reducing the 1-halo contributions to $\xi_g(r)$. We demonstrate this point with an explicit example in Figure 9. The long-dashed and dot-dashed lines show $\xi_g(r)$ for two models, one Average and one Poisson, with space densities $\bar{n}_g = 0.01h^3\text{Mpc}^{-3}$. The two correlation functions show similar departures from a power-law at $r \lesssim 2h^{-1}\text{Mpc}$. Raising M_1 to reduce the number density to $\bar{n}_g = 0.001h^3\text{Mpc}^{-3}$ does not change the correlation function of the Poisson model (dotted line). However, the correlation function of the Average model drops dramatically on small scales and stays the same on large scales (short-dashed-line), yielding a (noisy) power-law $\xi_g(r)$. To raise the amplitude of $\xi_g(r)$ on large scales, one would want to increase M_{\min} and/or α as well as M_1 , changes that tend to boost the 1-halo term relative to the 2-halo term. The generic difficulty of finding HOD models that yield a high bias factor and a power-law $\xi_g(r)$ (see Fig. 8) suggests that suppression of 1-halo clustering by sub-Poisson fluctuations in low multiplicity halos is especially important for explaining the correlation function of luminous galaxies.

The quantitative results in this Section (and the rest of the paper) apply to the specific ΛCDM cosmological model used for the N-body simulation described in § 2. The galaxy correlation function depends on the HOD and on the mass and spatial distributions of dark matter halos themselves. In terms of the analytic discussion in § 3.1, the cosmological model influences $\xi_g(r)$ by determining dn/dM , $b_h(M)$, and $\xi_m(r)$ (see eqs. 8 and 11). However, we expect that our conclusions about the influence of HOD parameters on $\xi_g(r)$ and the generic requirements for obtaining a power-law correlation function would continue to hold for a fairly wide range of cosmological models.

In HOD models, a power-law correlation function emerges from a balance of several competing effects and therefore requires rather specific combinations of parameters. This complex explanation of a simple result may at first seem unreasonably contrived, but we see no physically realistic alternative. A model with $N_{\text{avg}}(M) \propto M$ above a mass threshold M_{\min} predicts a strongly scale-dependent bias in the non-linear regime if M_{\min} is large enough to exclude a significant fraction of the mass. Thus, even if the non-linear matter correlation function were a pure power law, that simplicity would be lost as soon as one demanded that luminous galaxies inhabit halos above some minimum mass. Eliminating the mass in low mass halos will in general change the 1-halo and 2-halo regimes of the correlation function by different factors, so there is no reason to think that a power-law dark matter correlation function would produce a power-law galaxy correlation function if a significant fraction of the mass resided in halos that were too small to host galaxies above the luminosity threshold, even if the galaxies traced the mass in larger halos. Furthermore, obtaining a power-law $\xi_m(r)$ requires features in the primordial matter power

spectrum that have no obvious physical motivation (Peacock & Dodds 1996).

We conclude instead that the observed power-law form of $\xi_g(r)$ provides a strong constraint on the physics of galaxy formation, and that the success of semi-analytic models (Kauffmann et al. 1999; Benson et al. 2000), hydrodynamic simulations (Pearce et al. 1999; Cen & Ostriker 2000; Davé et al. 2000; Yoshikawa et al. 2001), and high resolution N-body simulations (Colín et al. 1999) in reproducing this form is entirely non-trivial. In a subsequent paper (Berlind et al., in preparation), we will show that semi-analytic calculations and SPH simulations of the Λ CDM model predict $P(N|M)$ distributions that are similar to those of the broken power-law Average model shown in Figure 9, which does indeed yield a power-law $\xi_g(r)$. Improving observations of galaxy clustering already show evidence for statistically significant departures from a power-law correlation function on small scales at low (Connolly et al. 2001) and high (Porciani & Giavalisco 2001) redshift, in addition to the “shoulder” in $\xi_g(r)$ at $r \approx r_0$ (Gaztañaga & Juszkiewicz 2001 and references therein). Such departures are theoretically expected at some level, and they may provide further important clues to the properties of the HOD.

4. Other Statistics

4.1. Galaxy-Mass Cross-Correlation Function

Advances in wide-field digital imaging have recently begun to provide a new and direct probe of the relation between galaxies and dark matter, the galaxy-mass cross-correlation function $\xi_{gm}(r)$. This statistic can be measured using galaxy-galaxy lensing (Brainerd, Blandford, & Smail 1996; Griffiths et al. 1996; dell’Antonio & Tyson 1996; Hudson et al. 1998; Fischer et al. 2000; Smith et al. 2001) or by cross-correlating cosmic shear maps with galaxy light maps (Wilson, Kaiser, & Luppino 2001). Since the lensing signal depends on the surface density in units of the critical density for lensing, rather than the cosmic mean density, these techniques measure a combination of Ω_m and $\xi_{gm}(r)$ rather than $\xi_{gm}(r)$ alone. Recent analyses of galaxy-galaxy lensing in the SDSS (McKay et al. 2001) constrain $\xi_{gm}(r)$ out to $r \sim 1h^{-1}\text{Mpc}$ and demonstrate its dependence on galaxy luminosity, color, and environment.

Theoretical calculations of $\xi_{gm}(r)$ have been presented in the context of halo occupation models (Seljak 2000), semi-analytic galaxy formation models (Guzik, & Seljak 2001), and hydrodynamic simulations (White, Hernquist, & Springel 2001). Much of our analytic discussion of $\xi_g(r)$ in § 3.1 carries over to $\xi_{gm}(r)$, except that we are now considering the correlation between the galaxies and a second “population” of objects that trace the mass. On large scales, we expect

$$\xi_{gm}(r) = b\xi_m(r), \tag{14}$$

with the same bias factor given in equation (8). On small scales, we expect a “1-halo” term analogous to equation (10), but with halos weighted by $MN_{\text{avg}}(M)$ instead of $\langle N(N-1) \rangle_M$. An important consequence of this change is that the shape of $P(N|N_{\text{avg}})$ should not influence $\xi_{gm}(r)$ even in the 1-halo regime.

Figure 10 shows the galaxy-mass cross-correlation function for a variety of HOD models, with each panel concentrating on a specific feature of the HOD. Figure 10a shows the effect of varying

M_{\min} . On large scales, models with higher M_{\min} have a slightly higher bias factor, in agreement with our results for $\xi_g(r)$ in Figure 3. On small scales, higher M_{\min} models have a significantly larger $\xi_{gm}(r)$, since a larger fraction of their galaxies live in high mass halos. Increasing α raises $\xi_{gm}(r)$ for the same reasons, as shown in Figure 10b. The influence of α extends over a wider range of scales, as it did for $\xi_g(r)$ (see the discussion of Fig. 7c in § 3.2). Figure 10c confirms that $\xi_{gm}(r)$ does not depend on the shape of $P(N|N_{\text{avg}})$, since the 1-halo and 2-halo contributions are both controlled by $N_{\text{avg}}(M)$. For $\Delta\gamma = -1$, galaxies are more concentrated in the central, high density regions of halos, boosting $\xi_{gm}(r)$ on small scales (Fig. 10d). A central galaxy restriction has a similar effect, but the impact is confined to smaller r . Conversely, setting $\Delta\gamma = +1$ suppresses $\xi_{gm}(r)$ by pushing galaxies to lower density regions of their parent halos.

For $r \lesssim 200h^{-1}\text{kpc}$, our approach of selecting N-body particles to represent galaxies necessarily underestimates $\xi_{gm}(r)$ for a given HOD because it cannot account for the ability of condensed baryons to concentrate dark matter around them. One could do somewhat better by locating galaxies at density peaks of halo substructure, but this method still would not capture the effects of baryonic dissipation on the dark matter distribution. We expect our approach to be accurate at larger scales (note, for example, that the effect of a central galaxy restriction is negligible beyond $200h^{-1}\text{kpc}$) and to illustrate the correct qualitative dependence on HOD parameters even at small r .

With observations of $\xi_g(r)$ and $\xi_{gm}(r)$, one can define a bias function $b(r) = \xi_g(r)/\xi_{gm}(r)$. At least on large scales, we expect this ratio to equal the bias between the galaxy and matter correlation functions $[\xi_g(r)/\xi_m(r)]^{1/2}$, allowing $\xi_m(r)$ to be inferred indirectly. Figure 11 confirms this expectation for several HOD models. In each panel, thick and thin solid curves represent the two bias functions for an HOD model with $M_{\min} = 2.8 \times 10^{11}h^{-1}M_{\odot}$, $\alpha = 0.5$, and an Average $P(N|N_{\text{avg}})$. Thick and thin dashed curves show corresponding results for a model with higher M_{\min} (11a), higher α (11b), or Poisson $P(N|N_{\text{avg}})$ (11c). All of the curves go flat at $r \gtrsim 4h^{-1}\text{Mpc}$, indicating that $\xi_g(r)$ and $\xi_{gm}(r)$ have the same shape as $\xi_m(r)$. In this regime, the two definitions of b are in essentially perfect agreement. At smaller r , the bias functions are scale-dependent and do not track each other perfectly, though for a given model, they have similar shapes even in this regime. From Figure 11 we see that a similarity of shape between $\xi_g(r)$ and $\xi_{gm}(r)$ should not be taken as evidence that galaxies trace mass (Wilson et al. 2001). However, if measurements of $\xi_{gm}(r)$ can be pushed to $r \gtrsim 4h^{-1}\text{Mpc}$, they should yield an accurate estimate of $\xi_g(r)/\xi_m(r)$, and even on smaller scales they can indicate whether galaxies are more or less clustered than the matter. Since the weak lensing signal depends on Ω_m as well as $\xi_{gm}(r)$, these measurements will generally constrain a combination of Ω_m and b rather than b alone.

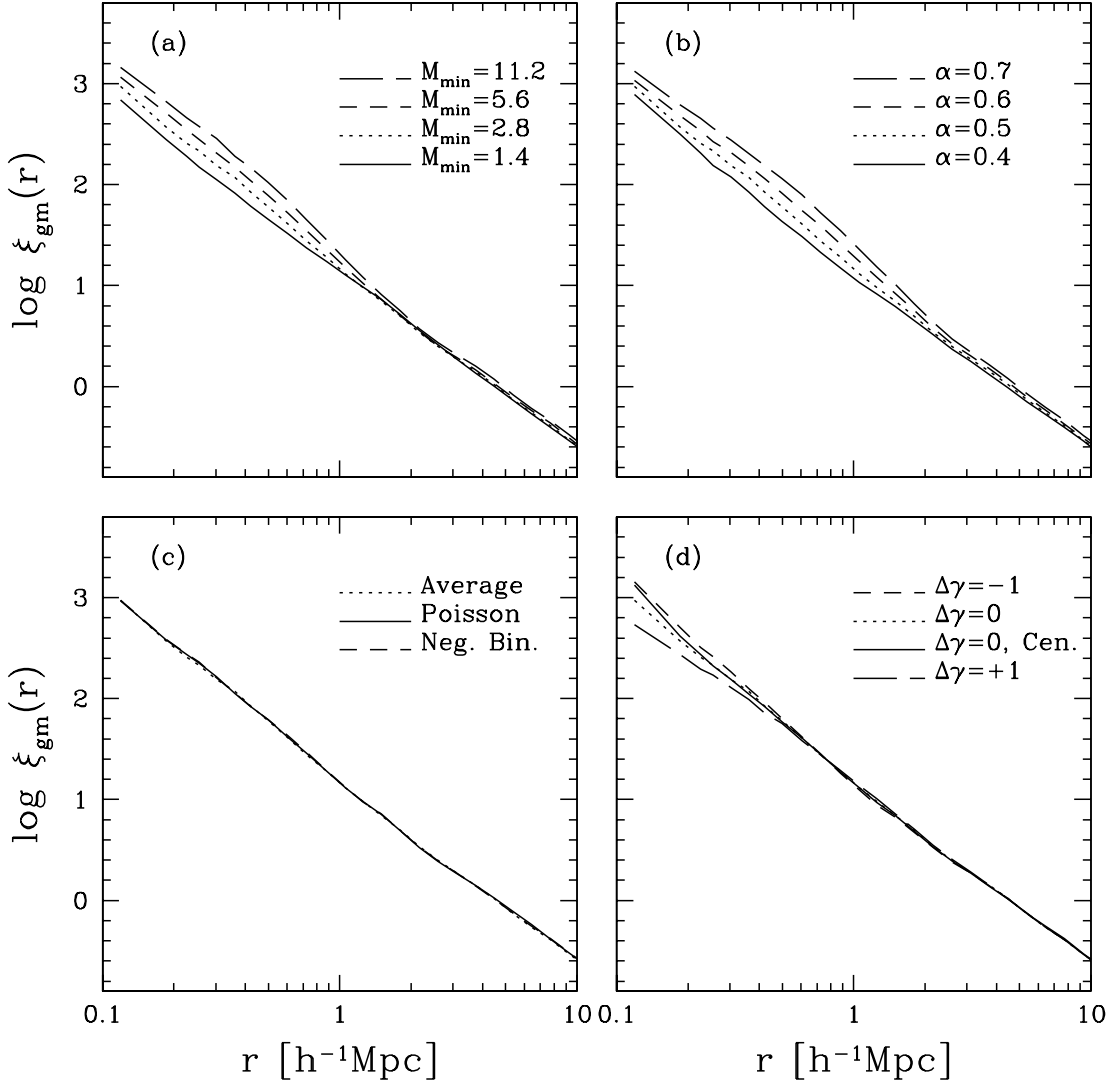


Fig. 10.— Galaxy-mass cross-correlation functions for different HOD prescriptions. In each panel, the dotted curve shows $\xi_{gm}(r)$ for a model with power-law $N_{\text{avg}}(M)$, $M_{\min} = 2.8 \times 10^{11} h^{-1} M_{\odot}$, $\alpha = 0.5$, Average $P(N|N_{\text{avg}})$, and $\Delta\gamma = 0$. Other curves show $\xi_{gm}(r)$ for models with different M_{\min} (panel a), different α (panel b), different $P(N|N_{\text{avg}})$ (panel c), or different galaxy distributions within halos (panel d).

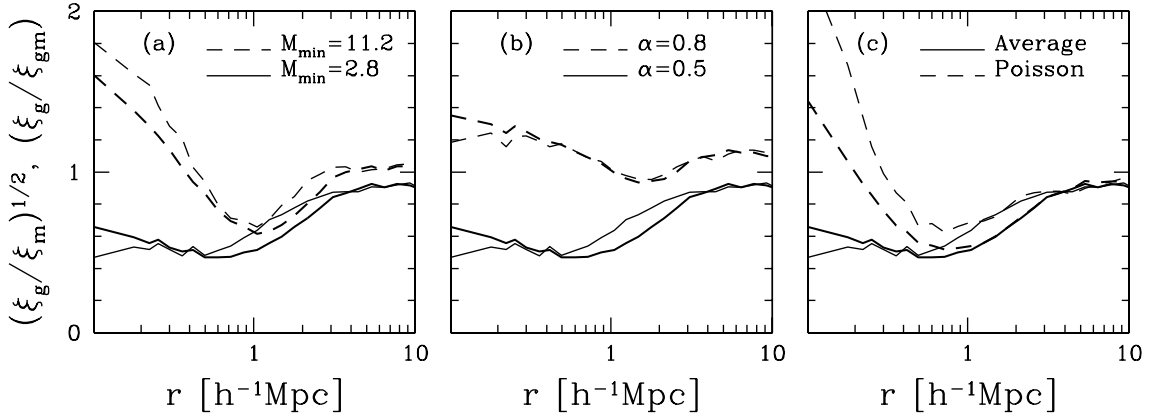


Fig. 11.— Effective bias functions defined by ratios of correlation functions for different HOD prescriptions. Thick curves represent $(\xi_g/\xi_m)^{1/2}$, where ξ_g and ξ_m are the galaxy and mass autocorrelation functions, respectively. Thin curves represent $(\xi_g/\xi_{gm})^{1/2}$, where ξ_{gm} is the galaxy-mass cross-correlation function. In each panel, solid curves represent an HOD model with power-law $N_{\text{avg}}(M)$, $M_{\min} = 2.8 \times 10^{11} h^{-1} M_{\odot}$, $\alpha = 0.5$, and Average $P(N|N_{\text{avg}})$. Dashed curves represent models with different M_{\min} (panel a), different α (panel b), or different $P(N|N_{\text{avg}})$ (panel c).

If one’s goal is to determine the HOD given a known cosmology, then the principal virtue of $\xi_{gm}(r)$ is its sensitivity to $N_{\text{avg}}(M)$ in a regime where $\xi_g(r)$ is sensitive to $\langle N(N-1) \rangle_M$. By combining the two statistics, one can discriminate between models that have different $P(N|N_{\text{avg}})$, even if $N_{\text{avg}}(M)$ is adjusted so that the models produce similar galaxy correlation functions.³ However, independent data will not determine cosmological parameters perfectly, and the more crucial role of galaxy-galaxy lensing measurements will be to help break the degeneracy between the HOD and the background cosmology, by providing direct estimates of the masses of the halos that galaxies inhabit. We return to this point in § 6.

4.2. Bispectrum

Higher order clustering statistics complement the information in the two-point correlation functions $\xi_g(r)$ and $\xi_{gm}(r)$. Because rare, high multiplicity halos make a larger contribution to high order statistics, we expect them to be more sensitive to the occupation of massive halos and to the high- N tails of $P(N|N_{\text{avg}})$. Ma & Fry (2000) and Scoccimarro et al. (2000) give fairly comprehensive analytic discussions of the three-point correlation function and its Fourier transform, the bispectrum, in the halo occupation framework. The basic principles are similar to those that govern $\xi_g(r)$ and $P_g(k)$ — for example, small scale correlations are dominated by a 1-halo term, in which halos of mass M contribute in proportion to the mean number of galaxy triples per halo, $\langle N(N-1)(N-2) \rangle_M$. However, the mathematics of three-point correlations is considerably more intricate, in part because there are three terms (1-, 2-, and 3-halo) contributing to the galaxy correlations, and in part because the bias of the halos is more complicated. On large scales, where second-order perturbation theory is valid, the relation between the halo and mass three-point correlations depends on two bias factors, one describing the ratio of rms halo and mass fluctuations and one describing the non-linearity of the relation between halo number and mass density contrast.

To facilitate comparison with other work, we focus here on the reduced bispectrum,

$$Q(\mathbf{k}_1, \mathbf{k}_2, \mathbf{k}_3) = \frac{B(\mathbf{k}_1, \mathbf{k}_2, \mathbf{k}_3)}{P(k_1)P(k_2) + P(k_2)P(k_3) + P(k_3)P(k_1)}, \quad k_i = |\mathbf{k}_i|, \quad (15)$$

where $B(\mathbf{k}_1, \mathbf{k}_2, \mathbf{k}_3)$ is the bispectrum itself, and $P(k)$ is the power spectrum. The three wave-vectors form a triangle $\mathbf{k}_1 + \mathbf{k}_2 + \mathbf{k}_3 = 0$, so they can also be specified by the magnitude k_1 , the ratio k_1/k_2 , and the angle θ between \mathbf{k}_1 and \mathbf{k}_2 . In second-order perturbation theory, the reduced matter bispectrum Q_m is independent of the scale k_1 , but it depends on the triangle shape, with higher Q_m at the elongated configurations ($\theta \approx 0^\circ$ and $\theta \approx 180^\circ$) favored by anisotropic gravitational collapse (Fry 1984). In bias models where the galaxy density contrast is a local function of the mass density contrast, $\delta_g = f(\delta_m)$, a second-order calculation yields

$$Q_g = \frac{Q_m}{b_1} + \frac{b_2}{b_1^2}, \quad (16)$$

³The constraint of fixed number density greatly restricts one’s ability to trade off $N_{\text{avg}}(M)$ against $P(N|N_{\text{avg}})$, since $\int dM \frac{dn}{dM} N_{\text{avg}}(M)$ must remain constant. However, $\xi_{gm}(r)$ provides more discriminating power because different scales constrain the behavior of $N_{\text{avg}}(M)$ in different halo mass ranges.

where $b_1 = f'(0)$ and $b_2 = \frac{1}{2}f''(0)$ (Fry 1994; see also Fry & Gaztañaga 1993; Juszkiewicz et al. 1995). On smaller scales, the value of Q_m rises and then plateaus at a higher level, and the dependence of Q_m on triangle shape decreases (Ma & Fry 2000; Scoccimarro et al. 2000).

To compute the reduced bispectrum, we form continuous density fields by cloud-in-cell (CIC) binning the discrete mass or galaxy distributions onto a 200^3 grid and calculate $P(k)$ and $B(\mathbf{k}_1, \mathbf{k}_2, \mathbf{k}_3)$ using a Fast Fourier Transform (FFT). Figure 12 shows $Q_{\text{eq}}(k)$, the reduced bispectrum as a function of scale in the equilateral triangle case ($k_1 = k_2 = k_3$), for a variety of HOD models and for the unbiased mass distribution. For the same set of HOD models, Figure 13 shows $Q(\theta)$, the reduced bispectrum as a function of triangle shape, in the case $k_1 = 2k_2 = 1h\text{Mpc}^{-1}$. The fundamental mode of the $141.3h^{-1}\text{Mpc}$ simulation cube is $k_f = 0.0445h\text{Mpc}^{-1}$. In Figure 12, $Q_{\text{eq}}(k)$ curves for the mass distribution begin at $k_1 = 3k_f$, and in Figure 13 $k_1 = 2k_2 = 22.5k_f$.

Figures 12a and 13a show models with $\alpha = 0.5$, Average $P(N|N_{\text{avg}})$, and varying values of M_{min} . Because of the limited size of the simulation volume, the mass $Q_{\text{eq}}(k)$ does not show the low- k plateau predicted by perturbation theory very clearly, though it does show the usual rise into the non-linear regime and plateau at high- k . The scale k_1 adopted in Figure 13 is sufficiently non-linear that most of the shape dependence in $Q_m(\theta)$ has disappeared, though there is still a slight enhancement for elongated triangles. The galaxies have much lower values of $Q_{\text{eq}}(k)$. In the context of equation (16), we interpret the depression of $Q_{\text{eq}}(k)$ as a sign of negative b_2 , since the galaxies are *anti*-biased in an rms sense (compare the galaxy and mass correlation functions in Figure 3), and this anti-bias on its own would tend to boost Q ($b_1 < 1$).⁴ Turning to non-equilateral triangles in Figure 13a, we see that Q_g is strongly depressed relative to Q_m for $30^\circ \lesssim \theta \lesssim 140^\circ$ but rises towards Q_m near $\theta = 0^\circ$ and, especially, near $\theta = 180^\circ$. As a result, the shape dependence of Q_g is stronger than that of Q_m . We are unsure how to explain the shape dependence of the suppression of Q_g , though a greater impact of bias on roughly equilateral configurations than on elongated configurations is not surprising.

In Figure 12a, we see that changing M_{min} has no significant impact on $Q_{\text{eq}}(k)$ in these models. While $B_{\text{eq}}(k)$ and $P(k)$ both increase for larger M_{min} , the two effects cancel in the ratio that defines Q . Figure 13a shows a modest dependence of $Q(\theta)$ on M_{min} for $\theta \gtrsim 140^\circ$, perhaps because the signature of elongated structures is stronger when galaxies are distributed among lower mass halos (smaller M_{min}). Figure 12b shows the dependence of $Q_{\text{eq}}(k)$ on α ; while $B_{\text{eq}}(k)$ and $P(k)$ both increase for larger α , $B_{\text{eq}}(k)$ grows faster, and $Q_{\text{eq}}(k)$ rises closer to the value of Q_m . Because low α suppresses $Q(\theta)$ primarily at intermediate values of θ , the triangle-shape dependence weakens as α increases (Fig. 13b).

Figures 12c and 12d show the dependence of $Q_{\text{eq}}(k)$ on the form of $P(N|N_{\text{avg}})$ for $M_{\text{min}} = 2.8 \times 10^{11}h^{-1}M_\odot$ and $\alpha = 0.5$ and 0.8 , respectively. The dependence is minimal in the first case but significant in the second, with the Average distribution producing the highest $Q_{\text{eq}}(k)$ at high k . While the narrower width of the Average distribution leads to a smaller $B_{\text{eq}}(k)$, it causes a still larger reduction in the denominator of equation (15), thus boosting Q . The greater

⁴The association of b_1 and b_2 with derivatives of $f(\delta_m)$ is no longer accurate in the non-linear regime, but one can still define $b_1 = [P_g(k)/P_m(k)]^{1/2}$ and define b_2 through equation (16), though b_2 may now be dependent on triangle shape.

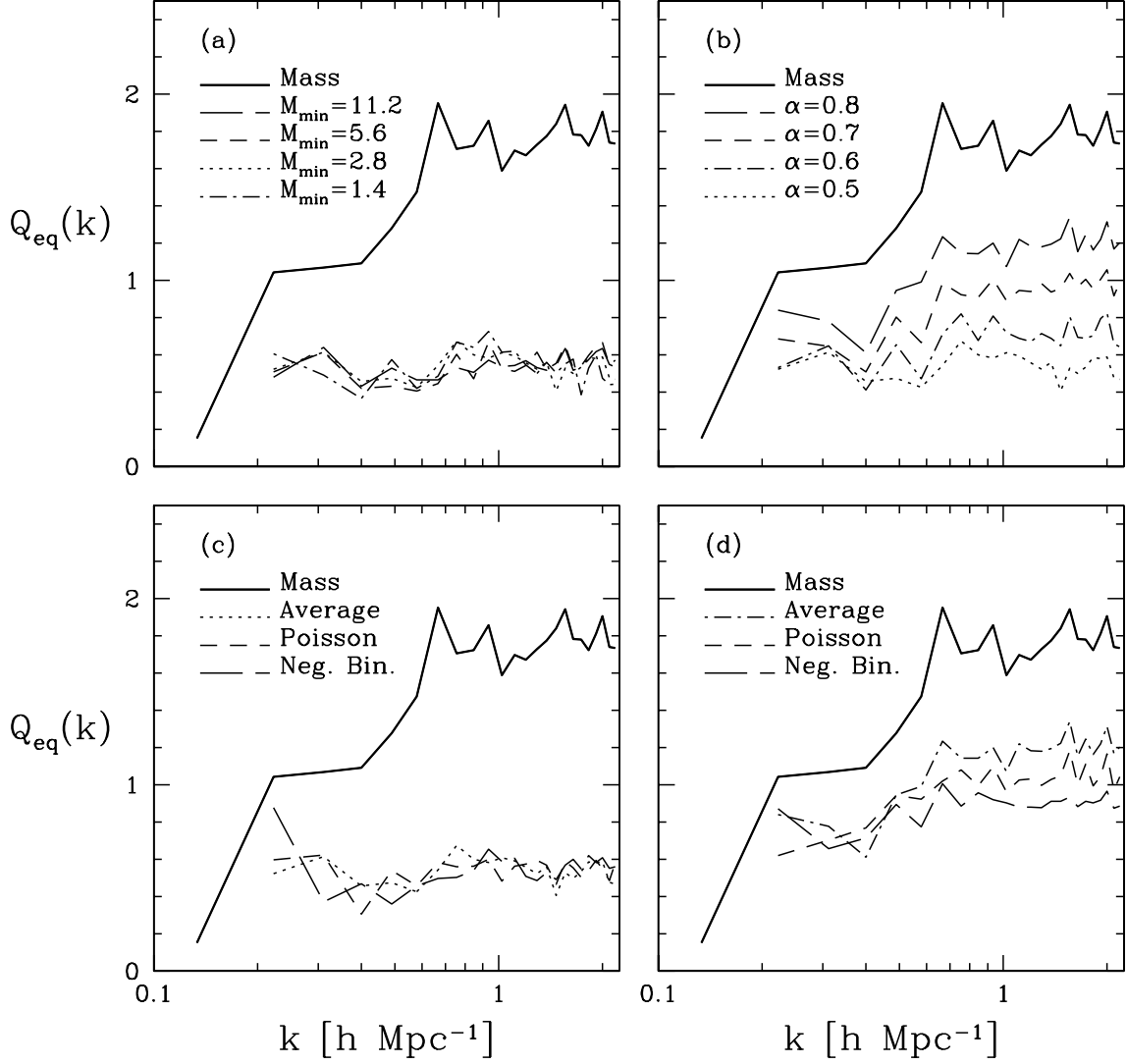


Fig. 12.— Reduced bispectrum $Q_{\text{eq}}(k)$ for equilateral configurations as a function of scale, for different HOD prescriptions. In panels (a)-(c), the dotted curve shows $Q_{\text{eq}}(k)$ for a model with power-law $N_{\text{avg}}(M)$, $M_{\text{min}} = 2.8 \times 10^{11} h^{-1} M_{\odot}$, $\alpha = 0.5$, and Average $P(N|N_{\text{avg}})$. Other curves show $Q_{\text{eq}}(k)$ for models with different M_{min} (panel a), different α (panel b), or different $P(N|N_{\text{avg}})$ (panel c). Panel (d) shows models with different $P(N|N_{\text{avg}})$ for $\alpha = 0.8$. Thick solid curves show $Q_{\text{eq}}(k)$ for the unbiased mass distribution.

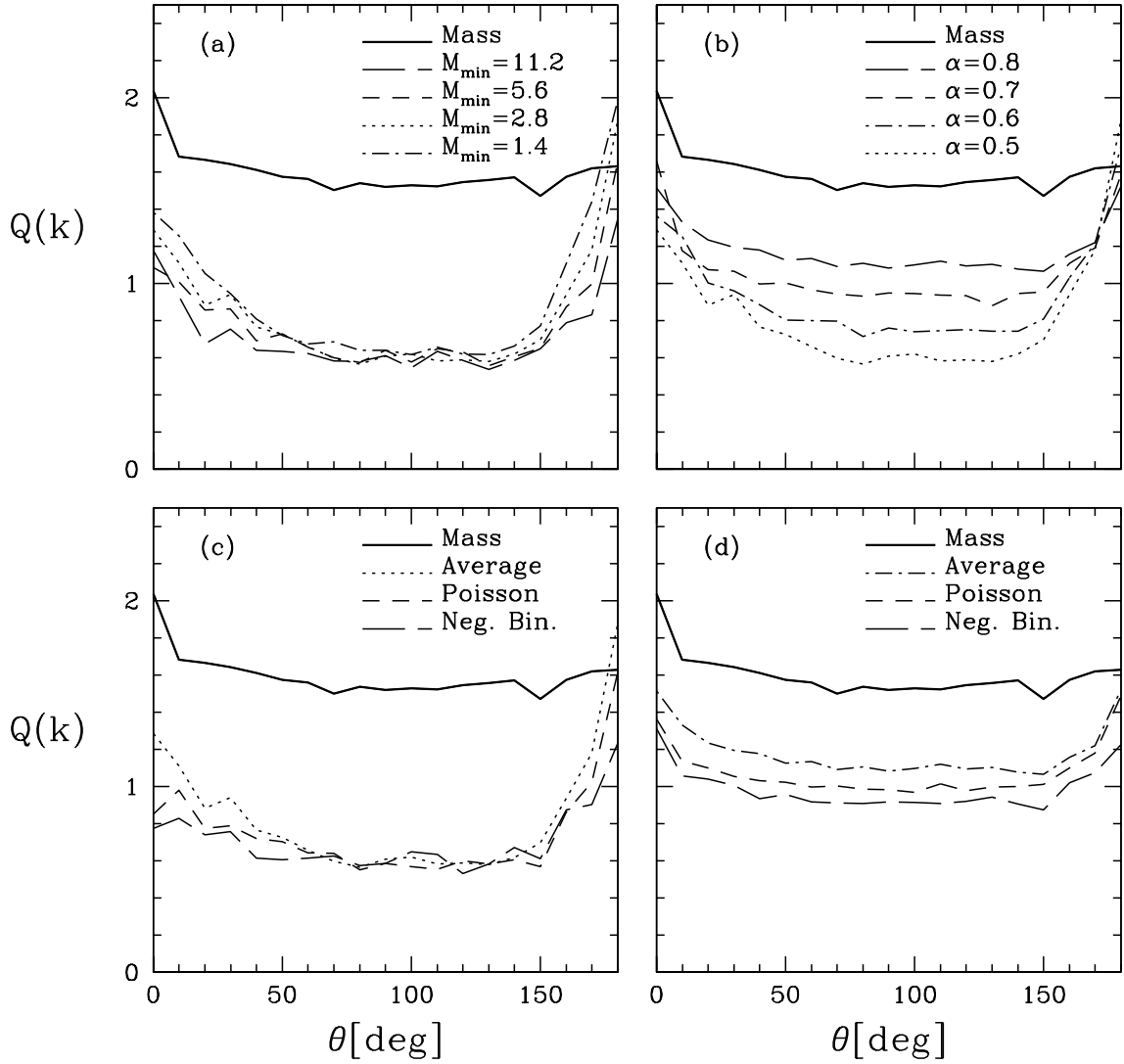


Fig. 13.— The reduced bispectrum $Q(\theta)$ as a function of triangle shape, where $k_1 = 2k_2 = 1h\text{Mpc}^{-1}$ ($k = 2\pi/\lambda$). The four panels show the same HOD models as in Fig. 12.

dependence on $P(N|N_{\text{avg}})$ for higher α reflects the greater importance of the 1-halo and 2-halo terms when massive halos are highly occupied, since the 3-halo term is independent of $P(N|N_{\text{avg}})$ but the other two are not. Figures 13c and 13d show a slight dependence of $Q(\theta)$ on $P(N|N_{\text{avg}})$ for $\alpha = 0.5$ and a depression of $Q(\theta)$ at all angles for the broader distributions when $\alpha = 0.8$.

We have found the influence of HOD parameters on the reduced bispectrum relatively difficult to interpret cleanly, for several reasons. First, HOD changes influence both the individual terms (1-, 2-, and 3-halo) contributing to the bispectrum and the relative importance of those terms, and it is not always clear which effect is more significant. Second, the use of a Fourier space measure makes it more difficult to separate terms based on scale — the 1-halo contribution to the three-point function, for example, must vanish beyond the virial diameter of the largest halos, but it can still have an influence on the bispectrum down to fairly low k . Finally, while the influence of an HOD change on the bispectrum or power spectrum may be easy to guess, the effect on the ratio Q is often much harder to predict. The reduced bispectrum is a natural statistic for describing mass clustering, especially in the perturbative regime. However, the unreduced, configuration space three-point function may prove more useful in unraveling the HOD, at least on scales of individual halos.

We have also computed the hierarchical amplitudes S_3 and S_4 (related to the skewness and kurtosis, respectively), as a function of smoothing scale. These results are qualitatively similar to those for the reduced bispectrum shown in Figure 12, so we do not show them here.

Despite the complexities, three-point correlations clearly have information content that is not present in $\xi_g(r)$, because of their dependence on higher moments of $P(N|N_{\text{avg}})$ and their greater weighting of massive halos. The dependence of Q on M_{min} , α , and $P(N|N_{\text{avg}})$ is significantly different from the dependencies found for $\xi_g(r)$ in § 3. We therefore expect three-point correlations to play an important role in constraining the HOD and breaking degeneracies between bias and cosmology. The suppression of Q_g relative to Q_m in HOD models with $\alpha < 1$ (seen for all of the cases in Figure 12) may help to explain the low amplitude that Jing & Börner (1998) find for the configuration-space three-point function of LCRS galaxies, which is reduced relative to the N-body prediction for the mass distribution by about a factor of two.

4.3. Void Probability Function

We now turn to a statistic which focuses on the lowest density regions, the voids in the galaxy distribution. The statistic we examine is the void probability function (VPF), and it is defined as the probability $P_0(R)$ that a randomly placed sphere of radius R contains no galaxies. The best observational study of the VPF to date is the analysis of the CfA2 redshift survey by Vogeley et al. (1994), though 2dFGRS and SDSS should yield results in the near future. Little & Weinberg (1994) showed that the VPF is sensitive to the details of biasing, using environmental bias models. In the HOD context, the VPF should depend on the expected number of halos contained within a given sphere, as well as the expected number of galaxies per halo. The VPF does not distinguish between halos that contain one galaxy and those that contain multiple galaxies, since one galaxy alone prevents a region from being empty. Therefore, the VPF should be very sensitive to the halo mass regime $M_{\text{min}} \leq M \leq M_1$, where most halos contain either one galaxy or no galaxies. Benson

(2001) has analytically studied count probabilities in the HOD framework, and Casas-Miranda et al. (2001) have studied halo counts in voids. These are steps towards an analytic description of the galaxy VPF under HOD bias. Here we provide an approximate model that is useful for understanding our numerical results.

The number of galaxies expected in a volume V that has a density contrast δ is

$$\langle N|V, \delta \rangle = V \int_0^\infty dM \left. \frac{dn}{dM} \right|_\delta N_{\text{avg}}(M), \quad (17)$$

where the halo mass function is conditional on δ because halos are, on average, more abundant and more massive in high density regions than in low density regions. The amplitude of dn/dM is enhanced by the same factor $(1 + \delta)$ that affects the mass density. However, the shape of the mass function also depends on environment: in low density regions, gravitational growth of structure is suppressed, and the halo mass function shifts towards lower masses. This dependence of the halo mass function on density is the basis for the Mo & White (1996) calculation of halo bias. For our present purposes, it is useful to write equation (17) as

$$\langle N|V, \delta \rangle = V(1 + \delta) \int_0^\infty dM \left. \frac{dn}{dM} \right|_{\delta_L} N_{\text{avg}}(M), \quad (18)$$

where δ_L denotes the Lagrangian density contrast associated with the evolved non-linear density contrast δ . In equation (18), the dispersal of halos by the expansion of underdense regions is represented by $(1 + \delta)$, while the shift of the mass function is represented by $\left. \frac{dn}{dM} \right|_{\delta_L}$.

For a Poisson distribution of mean $\langle N \rangle$, the probability of having $N = 0$ is $P(0) = \exp(-\langle N \rangle)$. The actual probability distribution of galaxy counts depends both on $P(N|N_{\text{avg}})$ and on the probability distribution of halo counts; however, approximating the combined effect as Poisson provides a useful guide for understanding the VPF. In the Poisson approximation, we can write an expression for the VPF by integrating over δ ,

$$P(N = 0|V) = \int_{-\infty}^\infty d\delta P(\delta|V) (1 + \delta) \exp \left[-V \int_0^\infty dM \left. \frac{dn}{dM} \right|_{\delta_L} N_{\text{avg}}(M) \right], \quad (19)$$

where $P(\delta|V)$ is the probability that a sphere of volume V has a mass density contrast δ . If we ignored the dependence of dn/dM on δ_L , the exponential factor would simply be $\exp(-V\bar{n}_g)$, and the VPF would thus not depend on the HOD. For $V\bar{n}_g \lesssim 1$, the exponential factor will not be too far from unity, so the VPF will depend mainly on $P(\delta)$. However, at large R , where $V\bar{n}_g \gg 1$, the exponential suppression is usually large, and changes to $N_{\text{avg}}(M)$ can potentially have very large effects on the VPF.

Figure 14 shows VPFs for a variety of HOD models, as well as for the unbiased mass distribution. Since the VPF is very sensitive to the number density of particles in the distribution being studied, we have randomly sampled the mass distribution to have the same space density of particles as the galaxy distributions. All HOD models shown have a power-law $N_{\text{avg}}(M)$. Figure 14a shows that changing M_{min} from 1.4 to 2.8 (in units of $10^{11}h^{-1}M_\odot$) has little effect but that raising it to 7 and again to 11.2 has a dramatic impact, especially at large R . This behavior has a natural explanation in the context of equation (19). When M_{min} is low, the integral inside

the exponential factor is never far from \bar{n}_g . However, when M_{\min} is large, the break in the halo mass function can shift below M_{\min} in the lowest density regions, decreasing the integral and producing an enormous increase in the exponential factor. Figure 14b shows the effect on the VPF of varying α . HOD models with higher values of α have somewhat higher probability of containing voids, since they have lower N_{avg} at masses just above M_{\min} , but the dependence of the VPF on α is clearly weaker than the dependence on M_{\min} . Figure 14c shows the effect of varying $P(N|N_{\text{avg}})$. Models with wider $P(N|N_{\text{avg}})$ distributions have a slightly higher probability of containing voids because they sometimes produce empty halos in the halo mass regime where $N_{\text{avg}} \sim 1 - 2$. Finally, Figure 14d shows that the VPF is completely insensitive to the distribution of galaxies within halos.

The VPF complements correlation statistics by responding sensitively to the low mass end of $P(N|M)$ and especially to the cutoff mass M_{\min} . The VPF is a special case of count probabilities or of the closely related probability distribution function (PDF) of smoothed density fields. We have also measured these full PDFs, and they respond roughly as one would expect: models with more “bias” produce wider PDFs. However, we have been unable to draw simple associations between specific features of PDFs and specific properties of the HOD, so we have chosen not to present these results in detail.

4.4. Pairwise Velocity Dispersion

The statistics we have examined so far characterize the clustering of galaxies in real space. However, there is also important information stored in galaxy peculiar velocities, which are gravitationally induced by the underlying mass distribution. One of the statistics most widely used to characterize the galaxy velocity distribution is the pairwise radial velocity dispersion,

$$\sigma_v^2(r) \equiv \langle |(\mathbf{v}_1 - \mathbf{v}_2) \cdot \mathbf{r}_{12}|^2 \rangle - \langle (\mathbf{v}_1 - \mathbf{v}_2) \cdot \mathbf{r}_{12} \rangle^2, \quad (20)$$

where \mathbf{v}_1 and \mathbf{v}_2 are the velocities of two galaxies separated by \mathbf{r}_{12} , and the average is over all galaxy pairs of separation $r = |\mathbf{r}_{12}|$. This quantity can be estimated from the 2-dimensional correlation function $\xi(r_p, \pi)$ (e.g., Davis & Peebles 1983), and its relatively low observed value provided one of the strongest early arguments against an $\Omega_m = 1$ cosmology with an unbiased galaxy distribution (Davis et al. 1985). Recent observations give $\sigma_v = 500 - 600 \text{ km s}^{-1}$ at $r \sim 1 h^{-1} \text{ Mpc}$ for typical optical samples, with a weak dependence on scale but a strong dependence on galaxy color or morphological type (Jing, Mo, & Börner 1998; Zehavi et al. 2001). Narayanan et al. (2000) found that $\sigma_v^2(r)$ is highly sensitive to the details of biasing, and here we wish to explore this sensitivity in the HOD framework of bias.

On small scales, $\sigma_v^2(r)$ will be dominated by pairs of galaxies within the same halo. If we assume that the halo velocity distribution is isotropic and isothermal, then the mean pairwise radial dispersion of galaxy pairs in a halo of mass M is $2\alpha_v^2\sigma^2(M)$, where $\sigma(M)$ is the halo’s one-dimensional velocity dispersion and α_v is the galaxy velocity bias parameter defined in § 2. The pairwise dispersion of the galaxy population is the average value of $2\alpha_v^2\sigma^2(M)$ weighted by the fraction of galaxy pairs of separation r contributed by halos of mass M . Reference to equation (11)

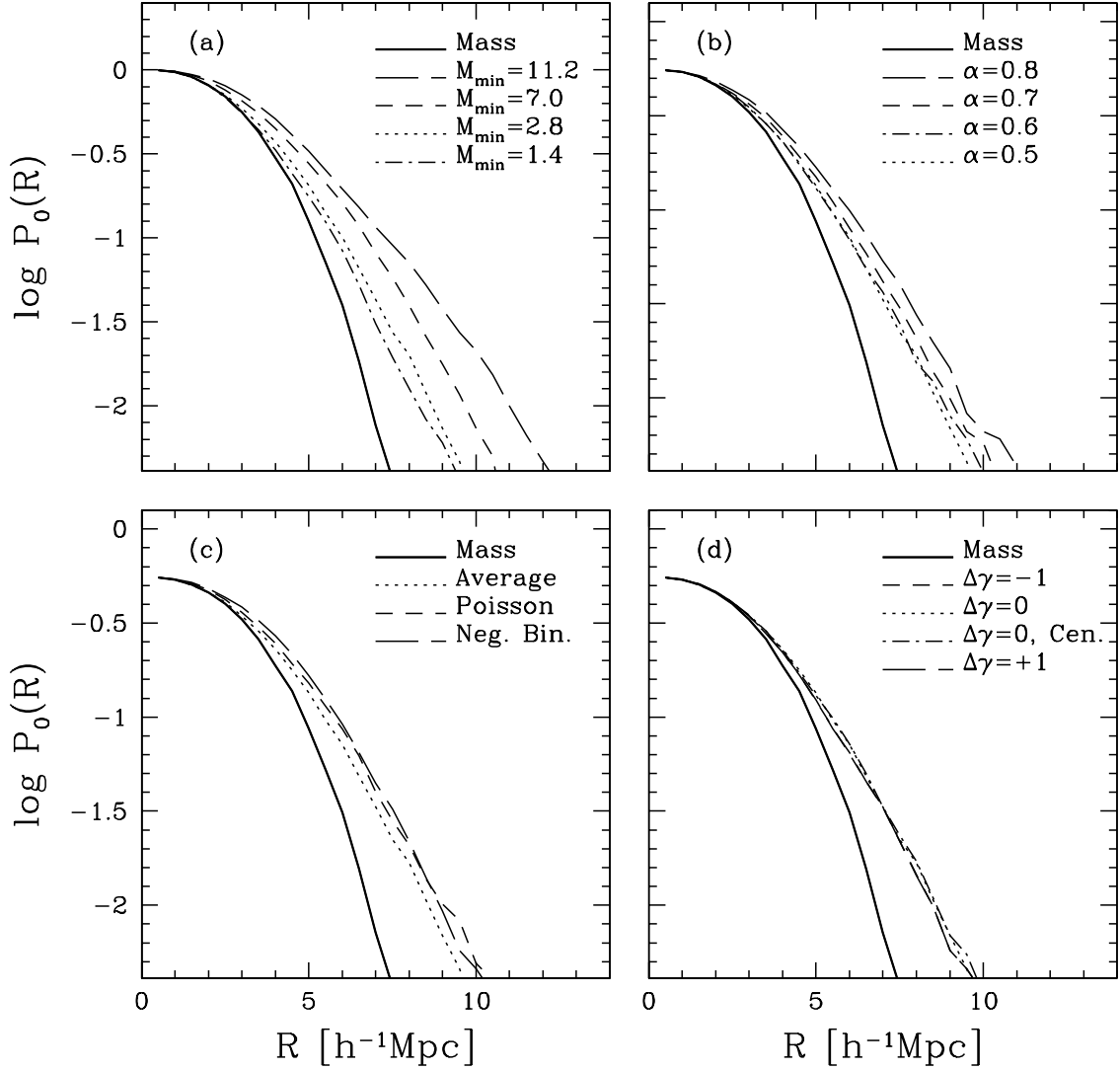


Fig. 14.— Void probability functions (VPF) for different HOD prescriptions. In each panel, the dotted curve shows the VPF for a model with power-law $N_{\text{avg}}(M)$, $M_{\min} = 2.8 \times 10^{11} h^{-1} M_{\odot}$, $\alpha = 0.5$, Average $P(N|N_{\text{avg}})$, and $\Delta\gamma = 0$. Other curves show VPFs for models with different M_{\min} (panel a), different α (panel b), different $P(N|N_{\text{avg}})$ (panel c), or different galaxy distributions within halos (panel d). Thick solid curves show the VPF for the unbiased mass distribution.

for $\xi_{1h}(r)$ shows that this average is

$$\sigma_{v,1h}^2(r) = \left[2\pi r^2 \bar{n}_g^2 \xi_g(r)\right]^{-1} \int_{M_{\min}}^{\infty} dM \frac{dn}{dM} \frac{\langle N(N-1) \rangle_M}{2} \frac{1}{2R_{\text{vir}}(M)} F' \left(\frac{r}{2R_{\text{vir}}} \right) 2\alpha_v^2 \sigma^2(M), \quad (21)$$

where we have assumed $\xi_g(r) = \xi_{1h}(r) \gg 1$.

At large scales, each member of a galaxy pair resides in a separate halo, and the velocity of each galaxy is the center-of-mass velocity of its halo plus a random velocity of 1-d dispersion $\alpha_v^2 \sigma^2(M)$. Since the random velocities are uncorrelated with the center-of-mass velocities and with each other, the mean pairwise dispersion of galaxy pairs in halos of mass M_1 and M_2 at separation r is $\sigma_{12}^2(r) + \alpha_v^2 \sigma^2(M_1) + \alpha_v^2 \sigma^2(M_2)$, where $\sigma_{12}^2(r)$ is the pairwise dispersion of halos. In the 2-halo regime, the pairwise dispersion of the galaxy population is the average of this quantity weighted by the number of pairs in halos of mass M_1 , M_2 , which is proportional to $(1 + \xi_{12}(r))N_{\text{avg}}(M_1)N_{\text{avg}}(M_2)$. Using equation (7) we have

$$\begin{aligned} \sigma_{v,2h}^2(r) &= \left[\bar{n}_g^2(1 + \xi_g(r))\right]^{-1} \int_{M_{\min}}^{\infty} dM_1 \frac{dn}{dM_1} N_{\text{avg}}(M_1) \int_{M_{\min}}^{\infty} dM_2 \frac{dn}{dM_2} N_{\text{avg}}(M_2) \\ &\quad \times (1 + \xi_{12}(r)) \left[\alpha_v^2 \sigma^2(M_1) + \alpha_v^2 \sigma^2(M_2) + \sigma_{12}^2(r)\right] \\ &= \frac{2\alpha_v^2}{1 + \xi_g(r)} \left[\langle \sigma^2(M) \rangle_N + \xi_g(r) \langle \sigma^2(M) \rangle_{Nb}\right] + \langle \sigma_{12}^2(r) \rangle, \end{aligned} \quad (22)$$

where

$$\langle \sigma^2(M) \rangle_N \equiv \bar{n}_g^{-1} \int_{M_{\min}}^{\infty} dM \frac{dn}{dM} N_{\text{avg}}(M) \sigma^2(M) \quad (23)$$

is the mean halo dispersion weighted by galaxy number,

$$\langle \sigma^2(M) \rangle_{Nb} \equiv (b\bar{n}_g)^{-1} \int_{M_{\min}}^{\infty} dM \frac{dn}{dM} N_{\text{avg}}(M) b_h(M) \sigma^2(M) \quad (24)$$

is the mean halo dispersion weighted by galaxy number and halo bias factor (and b is the galaxy bias factor of eq. [8]), and

$$\begin{aligned} \langle \sigma_{12}^2(r) \rangle &\equiv \left[\bar{n}_g^2(1 + \xi_g(r))\right]^{-1} \int_{M_{\min}}^{\infty} dM_1 \frac{dn}{dM_1} N_{\text{avg}}(M_1) \int_{M_{\min}}^{\infty} dM_2 \frac{dn}{dM_2} N_{\text{avg}}(M_2) \\ &\quad \times (1 + \xi_{12}(r)) \sigma_{12}^2(r) \end{aligned} \quad (25)$$

is the mean pairwise halo dispersion weighted by number of galaxy pairs. Since $\sigma_{12}(r)$ can in principle depend on both M_1 and M_2 , it cannot generally be pulled out of the integral in equation (25), though at large scales it may be close to the value $\sigma_{v,\text{lin}}^2(r)$ predicted for the mass by linear theory, since halos obtain their relative velocities from large scale density perturbations.

For a more detailed discussion, we refer the reader to Sheth et al. (2001), who give a much more comprehensive analytic treatment of the pairwise dispersion and mean streaming in the halo occupation framework and address a number of subtle issues (like non-isothermality) that we have glossed over here. For our purposes, the crucial features of equations (21) and (22) are the following. In the 1-halo regime, σ_v^2 depends on α_v^2 and $\langle N(N-1) \rangle_M$, and different halo

masses contribute on different scales just as they do in $\xi_{1h}(r)$. In the 2-halo regime, $\sigma_v^2(r)$ has one contribution that is proportional to α_v^2 and another that is independent of α_v . At large separations, where $\xi_g(r)$ is small, the first contribution becomes constant, so the *change* in $\sigma_v^2(r)$ is entirely due to $\langle\sigma_{12}^2(r)\rangle$.

Figure 15 shows the pairwise velocity dispersion for a variety of HOD models and for the unbiased mass distribution. Increasing M_{\min} (Fig. 15a) slightly increases $\sigma_v^2(r)$ because it forces galaxies into more massive halos with high velocity dispersions. However, increasing α (Fig. 15b) has a much more dramatic effect because it redistributes galaxies preferentially towards the most massive halos. For all α , $\sigma_v^2(r)$ has a broad maximum at $r \sim 1h^{-1}\text{Mpc}$, where the highest mass halos contribute a significant number of pairs. Higher α models have higher $\sigma_v^2(r)$ even at large scales because of the continuing contribution of $\langle\sigma^2(M)\rangle$ (eq. [22]). Figure 15c confirms that $\sigma_v^2(r)$ is independent of $P(N|N_{\text{avg}})$ on large scales, where the 2-halo term dominates. However, on small scales $P(N|N_{\text{avg}})$ has an important impact. While making $P(N|N_{\text{avg}})$ broader boosts the correlation function (Fig. 5), it drives $\sigma_v^2(r)$ *down* by allowing $\sigma_{v,1h}^2(r)$ to be dominated by pairs in low mass halos. For example, the Average model never has pairs in halos with $N_{\text{avg}}(M) < 1$, but the Poisson model does. Consequently, the small scale pairs in the Average model necessarily come from higher mass halos with larger velocity dispersions than in the Poisson model.

Figure 15d shows the influence of α_v on $\sigma_v^2(r)$, which is, as one might expect, very strong. The dotted line shows the extreme case of $\alpha_v = 0$, where $\sigma_v^2(r)$ comes only from the relative velocities of halos themselves. This contribution goes to zero in the 1-halo regime. It is usually sub-dominant even on large scales, but it dominates the *change* in $\sigma_v^2(r)$ because the internal dispersion contribution becomes constant. Increasing or reducing galaxy random velocities by a factor of two ($\alpha_v = 2$ or 0.5) changes $\sigma_v^2(r)$ by a large amount at all scales; note, however, that values of α_v so far from unity are probably implausible on dynamical grounds. The dot-long-dash line in Figure 15 shows the impact of a central galaxy on a model with $\alpha_v = 1$; the pairwise dispersion drops slightly because the central galaxy moves with the halo mean velocity.

In the absence of velocity bias, $\alpha_v \approx 1$, the pairwise dispersion is a good diagnostic of α , which controls the fraction of galaxies in high dispersion halos (Jing, Mo, & Börner (1998) reach a similar conclusion). It also constrains $P(N|N_{\text{avg}})$, with a rather different signature from $\xi_g(r)$. For the ΛCDM cosmology and HOD models considered here, matching the observed amplitude and weak scale-dependence of $\sigma_v^2(r)$ requires $\alpha \approx 0.5$ to suppress the peak at $r \sim 1h^{-1}\text{Mpc}$ associated with massive halos, and sub-Poisson fluctuations at low M to prevent low mass halos from dragging down $\sigma_v^2(r)$ at small r . These are the same features of $P(N|M)$ required to match $\xi_g(r)$. The pairwise dispersion is also sensitive to Ω_m and to the amplitude of the mass power spectrum, since these determine the scale of halo velocity dispersions and of relative halo velocities.

4.5. Redshift Space Distortions

The dispersion of galaxy peculiar velocities in collapsed regions smears structure along the line of sight in redshift space; it is this induced anisotropy that allows $\sigma_v^2(r)$ to be inferred from redshift maps without measuring galaxy peculiar velocities individually. On large scales, coherent flows into overdense regions and out of underdense regions amplify the contrast of structure along

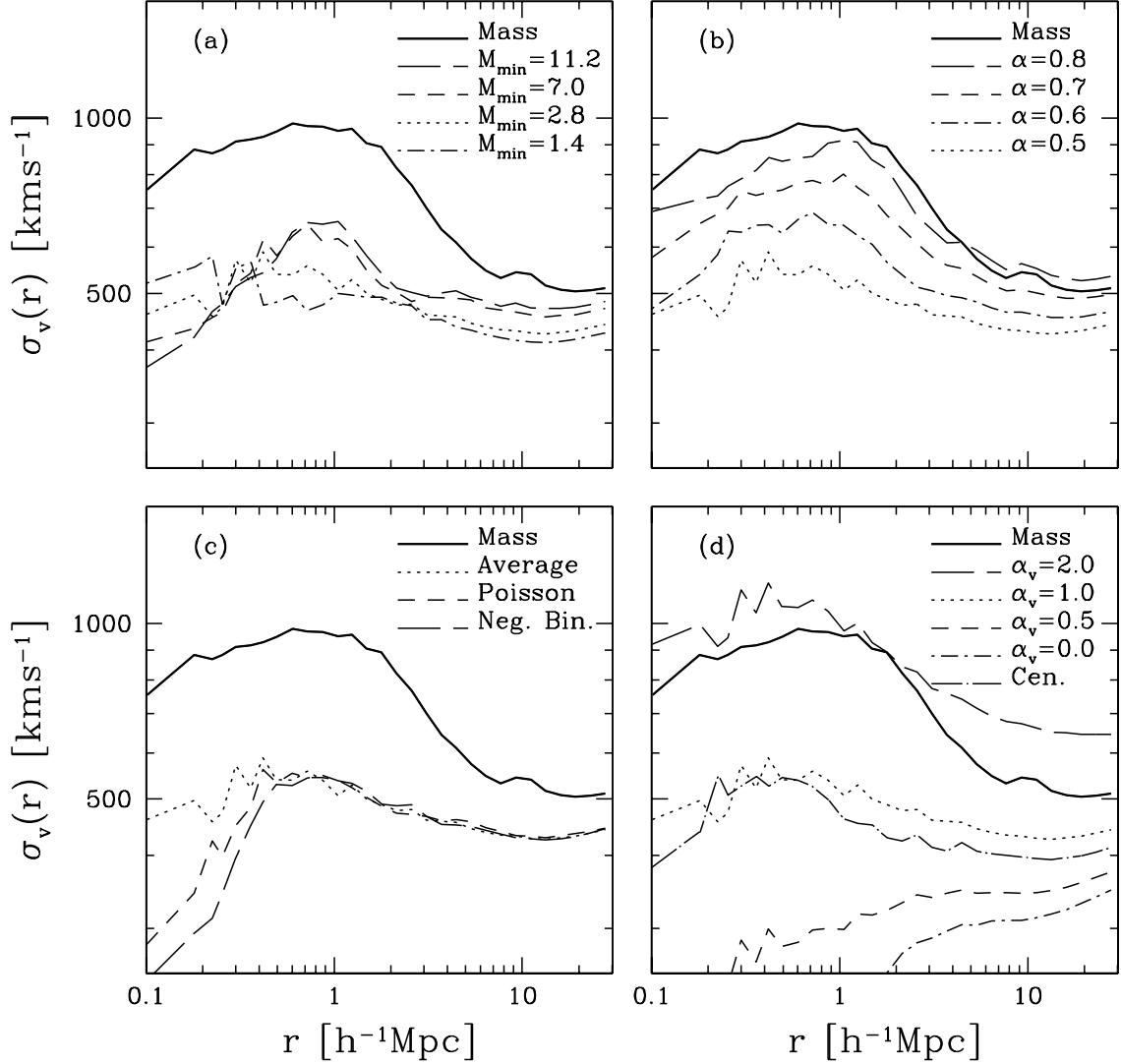


Fig. 15.— Mean pairwise radial velocity dispersions σ_v as a function of the pair separation r for different HOD prescriptions. In each panel, the dotted curve shows σ_v for a model with power-law $N_{\text{avg}}(M)$, $M_{\text{min}} = 2.8 \times 10^{11} h^{-1} M_{\odot}$, $\alpha = 0.5$, Average $P(N|N_{\text{avg}})$, and $\alpha_v = 1$. Other curves show σ_v for models with different M_{min} (panel a), different α (panel b), different $P(N|N_{\text{avg}})$ (panel c), or different velocity distributions within halos (panel d). Thick solid curves show σ_v for the unbiased mass distribution. The dot-long-dash curve in panel (d) shows a model with $\alpha_v = 1$ but the first, central galaxy in each halo forced to move at the halo’s mean velocity.

the line of sight (Sargent & Turner 1977; Kaiser 1987; for an excellent and comprehensive review see Hamilton 1998). In the linear regime, the linear bias approximation $\delta_g = b\delta_m$, and the distant observer approximation, the redshift-space power spectrum $P^S(k)$ is enhanced by a factor

$$\frac{P^S(k)}{P^R(k)} = 1 + \frac{2}{3}\beta + \frac{1}{5}\beta^2 \quad (26)$$

over the real-space power spectrum $P^R(k)$, where $\beta \equiv f(\Omega_m) \approx \Omega_m^{0.6}/b$ (Kaiser 1987). For models in which galaxy bias is a more complex function of local environment, equation (26) still applies on large scales, with b corresponding to the large-scale asymptotic value of the rms bias factor (Berlind et al. 2001). However, non-linear effects, especially those associated with velocity dispersions in collapsed regions, influence $P^S(k)$ out to scales $2\pi/k \sim 50 - 100h^{-1}\text{Mpc}$ or more (Cole et al. 1994). Measurement of β with redshift-space distortions therefore requires very large redshift surveys and accurate modeling of non-linear effects. The analysis of the 2dF galaxy redshift survey by Peacock et al. (2001) provides the best measurement to date.

We compute power spectra of our mass and galaxy distributions by CIC-binning them onto a 200^3 grid and applying an FFT. For the redshift-space power spectrum, we take the line-of-sight direction to be a Cartesian axis of the simulation cube, implicitly assuming that the whole simulation volume is far enough away to satisfy the distant observer approximation. Figure 16 shows $P^S(k)/P^R(k)$ for a variety of HOD models and for the unbiased mass distribution. The general behavior of these curves is as expected: suppression of the redshift-space power spectrum on small scales (high k), where non-linear effects dominate, and enhancement at low k . However, it is clear that the largest scales probed by our $141.3h^{-1}\text{Mpc}$ simulation cube are not yet in the linear regime described by equation (26), since there is no clear plateau in $P^S(k)/P^R(k)$ and the maximum ratio for the mass distribution is substantially lower than the value 1.37 implied for $\beta = 0.3^{0.6} = 0.48$.

In Figure 16a, raising M_{\min} depresses $P^S(k)/P^R(k)$ at all k . At small scales, where $P^S(k)/P^R(k) < 1$, this behavior reflects the increased suppression of line-of-sight structure by velocity dispersions in high mass halos. At large scales, one expects higher M_{\min} models to have lower $P^S(k)/P^R(k)$ because they have higher b (lower β), but the effect seen in Figure 16a may still be dominated by the increased residual impact of small scale velocity dispersions. All four HOD models have $\alpha = 0.5$, so relative to the mass distribution the high dispersion halos are down-weighted, and the large scale bias factor is slightly less than one. Thus, all four models have higher $P^S(k)/P^R(k)$ than the mass distribution. Raising α reduces $P^S(k)/P^R(k)$ by increasing velocity dispersions and the bias factor, as seen in Figure 16b. The $\alpha = 0.8$ model has nearly the same pairwise dispersion as the mass (Fig. 15b) and a large scale bias factor slightly larger than one (Fig. 4); as one might therefore expect, its $P^S(k)/P^R(k)$ ratio matches the mass on small scales and is slightly lower on large scales. Figure 16c shows that the form of $P(N|N_{\text{avg}})$ has no significant impact on the power spectrum distortion.

Figure 16d shows the impact of velocity bias within halos. Even though all four models have the same mean velocity field, their power spectrum ratios are different on all scales probed by the simulation. The comparison shows that the suppression of $P^S(k)/P^R(k)$ on small scales is dominated by dispersions within virialized halos. However, even the $\alpha_v = 0$ model shows a drop in $P^S(k)/P^R(k)$ relative to the value at large scales, showing that the dispersion of the halo velocities

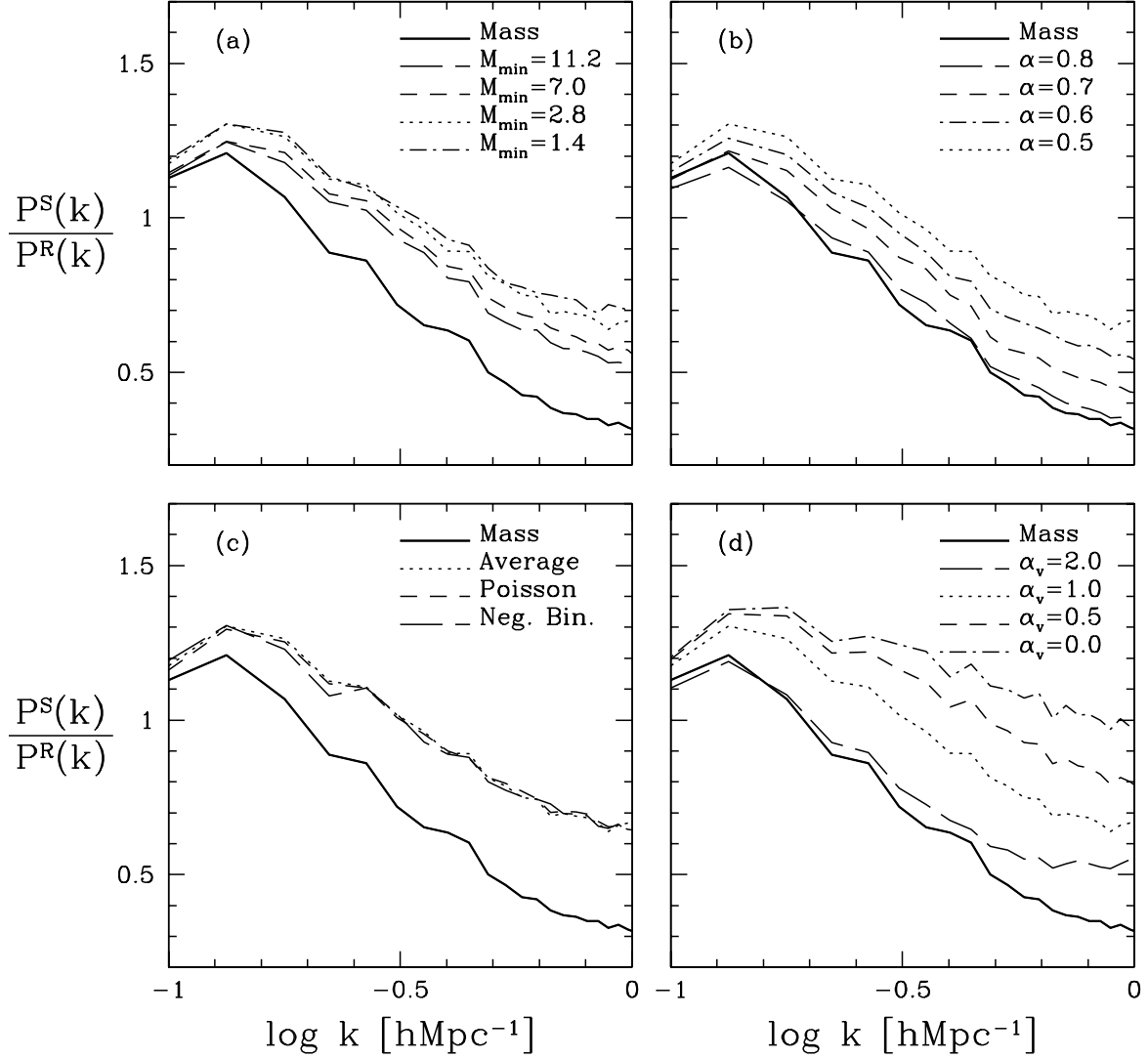


Fig. 16.— Ratios of the redshift to real space power spectra P^S/P^R as a function of wavenumber k for different HOD prescriptions. In each panel, the dotted curve shows $P^S(k)/P^R(k)$ for a model with power-law $N_{\text{avg}}(M)$, $M_{\text{min}} = 2.8 \times 10^{11} h^{-1} M_{\odot}$, $\alpha = 0.5$, Average $P(N|N_{\text{avg}})$, and $\alpha_v = 1$. Other curves show $P^S(k)/P^R(k)$ for models with different M_{min} (panel a), different α (panel b), different $P(N|N_{\text{avg}})$ (panel c), or different velocity distributions within halos (panel d). Thick solid curves show $P^S(k)/P^R(k)$ for the unbiased mass distribution.

themselves also plays a role. Above all, Figure 16d confirms previous indications that small scale galaxy velocity dispersions influence the redshift-space power spectrum out to remarkably large scales.

Redshift-space distortions can also be quantified using the ratio of quadrupole and monopole moments of $P^S(k)$ (Cole et al. 1994). We have measured this ratio as well as $P^S(k)/P^R(k)$ and find similar dependence on HOD parameters.

Although our simulation is not large enough to show it, we expect on the basis of Berlind et al. (2001) that the power spectrum ratio would approach the value defined by $\beta = \Omega_m^{0.6}/b_P$ at sufficiently low k , where b_P^2 is the asymptotic value of $P_g(k)/P_m(k)$. Even with a large galaxy redshift survey, constraining β requires modeling the non-linear effects on redshift-space distortions, which is most often done using the Peacock & Dodds (1994) model of a linear theory distortion modulated by random velocities with a single value of the velocity dispersion. With galaxy redshift samples of the size expected from the 2dF and SDSS, the limitation of this model introduces a systematic error that is larger than the statistical uncertainty (Cole et al. 1995; Hatton & Cole 1999). The HOD seems the natural framework in which to develop a more realistic and more accurate model of non-linear redshift-space distortions. The analytic studies of Seljak (2001) and White (2001) provide the basis for such a model, which should improve constraints on Ω_m and b from future analyses of larger data sets.

5. Group Statistics

The statistics that we have examined so far treat individual galaxies as the basic units of structure. A useful complementary strategy is to define groups of galaxies and measure their properties. We identify galaxy groups in real space using the same friends-of-friends algorithm that we used to find halos in the mass distribution. We use a linking length of 0.2 times the mean inter-galaxy separation, and we only retain groups containing four or more galaxies. Since our galaxy distributions have a space density of $0.01h^3\text{Mpc}^{-3}$, the linking length is approximately $0.9h^{-1}\text{Mpc}$. With this choice, most galaxies within the same halo are identified as belonging to the same group, but galaxies in separate halos are only occasionally linked. However, there are situations in which the galaxy populations of two halos are linked into a single group, and others where the population of one halo is split into two or more components, so the match between groups and halos is not exact. For a galaxy redshift survey there are additional complications including the need for different angular and redshift linking lengths to account for peculiar velocities, scaling linking lengths with distance to account for varying galaxy density in a flux-limited survey, and, in surveys that employ fiber spectrographs, accounting for incompleteness imposed by minimum fiber separations. (For discussion of some of these issues, see, e.g., Moore, Frenk, & White 1993 and Nolthenius, Klypin, & Primack 1994.) Here we consider the idealized case and leave the problem of design and performance of group-finding algorithms to studies that are tailored to specific data sets.

The most basic group statistic is the multiplicity function, the abundance of galaxy groups as a function of group richness. This can be measured for groups identified in a redshift survey (Maia, da Costa, & Latham 1989; Ramella, Geller, & Huchra 1989; Ramella et al. 1999), or from

the galaxy surface density in an imaging survey (Gott & Turner 1977; de Filippis et al. 1999). We define the cumulative multiplicity function $n_{\text{grp}}(> N)$ to be the number density of galaxy groups that contain N or more galaxies. To the extent that groups and halos correspond one-to-one, the differential group multiplicity function is simply a convolution of the halo mass function with $P(N|M)$, and the cumulative multiplicity function is

$$n_{\text{grp}}(> N) = \sum_N \int_0^\infty dM \frac{dn}{dM} P(N|M). \quad (27)$$

In the limit of a narrow $P(N|M)$, the space density of groups of multiplicity N is equal to the space density of halos with $N_{\text{avg}}(M) = N$. The direct connection implied by equation (27) makes the multiplicity function a promising tool for constraining $P(N|M)$.

Figure 17 plots $n_{\text{grp}}(> N)$ for a variety of HOD models, starting in each case at the largest group in the box and moving up to higher densities as N gets smaller. The function becomes noisy at high N where the number of groups is small. Increasing M_{min} (Fig. 17a) shifts $n_{\text{grp}}(> N)$ towards larger N , since the overall galaxy space density remains constant and the number of galaxies in high mass halos therefore increases. Increasing α has a much more drastic effect on the multiplicity function (Fig. 17b) because it boosts the multiplicity of higher mass halos by a larger factor, changing the slope of $n_{\text{grp}}(> N)$. Broadening $P(N|N_{\text{avg}})$ has a modest impact (Fig. 17c); while a given halo’s multiplicity can scatter in either direction, there are more low mass halos to scatter to high N than vice versa, so the net effect is to boost the high- N tail of the multiplicity function. Finally, Figure 17d shows that the group multiplicity function is completely insensitive to the spatial distribution of galaxies within halos, a reassuring indication that the friends-of-friends algorithm is consistently identifying the same groups regardless of their detailed internal structure.

From the HOD perspective, the other promising aspect of groups is the possibility of measuring their masses dynamically and thus obtaining a direct association between N and M . For each group in our simulated galaxy population, we apply the projected virial mass estimator given by Heisler, Tremaine, & Bahcall (1985),

$$M_{\text{vir}} = \frac{3\pi N}{2G} \frac{\sum_i V_{z,i}^2}{\sum_{i<j} 1/R_{\perp,ij}}, \quad (28)$$

where $V_{z,i}$ is the line-of-sight velocity of galaxy i relative to the group velocity centroid and $R_{\perp,ij}$ is the relative tangential separation between galaxies i and j . For this calculation, we treat one axis of the simulation box as the line-of-sight direction. (We have also tried the other mass estimators suggested by Heisler et al. 1985, with similar results.)

Figure 18 plots group richness against estimated virial mass for a variety of HOD models. Figure 18a shows a model with power-law $N_{\text{avg}}(M)$, $\alpha = 0.5$, $M_{\text{min}} = 2.8 \times 10^{11} h^{-1} M_{\odot}$, and Average $P(N|N_{\text{avg}})$. Each small point represents an individual galaxy group, and large points show the mean richness in bins of M_{vir} . If the group-halo match and virial mass estimates were perfect, this figure would reproduce the top panel of Figure 1, which illustrates the true $P(N|M)$ used to create this galaxy population. However, random errors in M_{vir} make the scatter-plot in Figure 18 much broader. Perhaps more seriously, the values of $N_{\text{avg}}(M)$ recovered from this

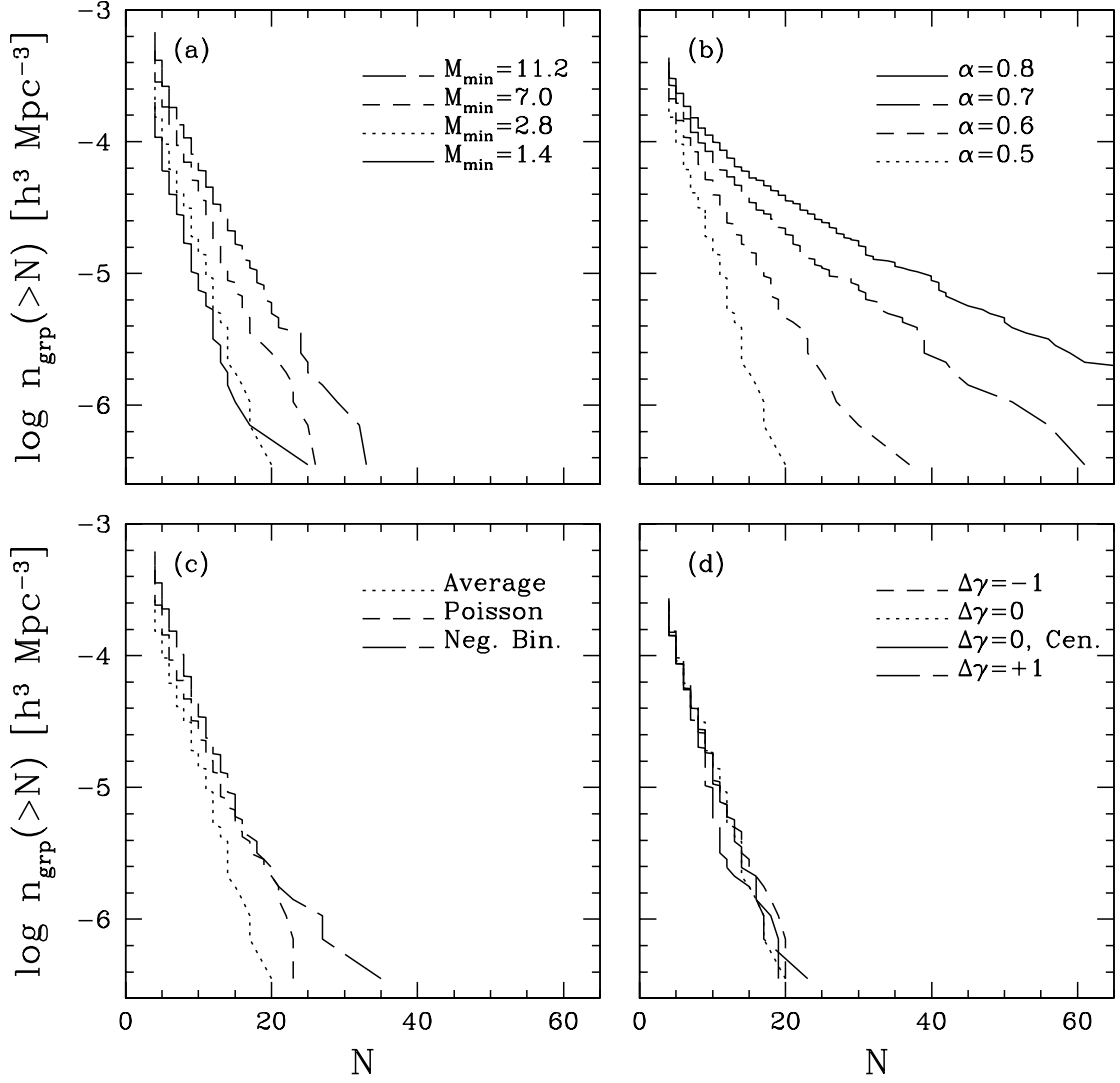


Fig. 17.— Cumulative group multiplicity functions for different HOD prescriptions. In each panel, the dotted curve shows $n_{\text{grp}}(>N)$ for a model with power-law $N_{\text{avg}}(M)$, $M_{\text{min}} = 2.8 \times 10^{11} h^{-1} M_{\odot}$, $\alpha = 0.5$, Average $P(N|N_{\text{avg}})$, and $\Delta\gamma = 0$. Other curves show $n_{\text{grp}}(>N)$ for models with different M_{min} (panel a), different α (panel b), different $P(N|N_{\text{avg}})$ (panel c), or different galaxy distributions within halos (panel d).

diagram are biased with respect to the true relation, shown by the solid line. At $M \lesssim 10^{13} h^{-1} M_{\odot}$, the mean multiplicity is overestimated because the group catalog excludes halos in this mass range that have $N < 4$. At high masses, random errors in M_{vir} cause a slight underestimate of $N_{\text{avg}}(M)$, since the number of low- N groups with overestimated M_{vir} exceeds the number of high- N groups with underestimated M_{vir} . Both of these biases are calculable, so data like those in Figure 18a could be corrected to yield a more accurate estimate of $N_{\text{avg}}(M)$. However, such a correction would require some assumptions about $P(N|M)$ (such as an extrapolation at the low mass end) and an accurate understanding of the error distribution of M_{vir} .

The situation is considerably more promising for the $\alpha = 0.7$ model shown in Figure 18b. This model has a much larger number of high multiplicity groups, which yield more accurate M_{vir} estimates because they have more galaxy tracers. Furthermore, the dynamic range in N is large enough to allow an accurate estimate of the slope of $N_{\text{avg}}(M)$ at high M , though the amplitude of the relation is still slightly underestimated. Figure 18c shows a model with a break in $N_{\text{avg}}(M)$ at $M_{\text{crit}} = 10^{14} h^{-1} M_{\odot}$. The virial mass estimates reveal the existence of the break and recover the high- M slope of $N_{\text{avg}}(M)$ reasonably well. However, the mass at which the break occurs and the slope at the low mass end of the relation are not clearly determined. A break at lower mass, like the one in the model illustrated in Figure 9, would pass undetected.

Figure 18d shows an $\alpha = 0.5$ model with a Poisson $P(N|N_{\text{avg}})$. Despite the scatter in the mass estimates themselves, the broader $P(N|M)$ is clearly detectable in comparison to the Average model of Figure 18a. The larger scatter increases the bias in the recovered $N_{\text{avg}}(M)$ at low M . Figure 18e shows a model with $\Delta\gamma = +1$, i.e., galaxies more extended than dark matter within halos, for which the recovered $N_{\text{avg}}(M)$ lies below the true relation at high M . Figure 18f shows a model with a strong velocity bias, $\alpha_v = 0.5$, which drives estimated masses down relative to true values. For rich groups and clusters, mass estimates from galaxy dynamics can be tested against masses estimated from X-ray observations or gravitational lensing, and systematic errors as large as those in Figures 18e and 18f (which display fairly extreme models) can probably be ruled out on the basis of existing studies (see, e.g., Wu et al. 1998). Such comparisons become harder for low multiplicity groups, though it may soon be possible to test for any overall bias by comparing mean dynamical masses to the group-mass correlation function derived from weak lensing.

Figure 18 suggests that it will be difficult to recover $P(N|M)$ or $N_{\text{avg}}(M)$ simply by measuring dynamical masses as a function of multiplicity. Even if there are no internal biases (like $\alpha_v \neq 1$ or $\Delta\gamma \neq 0$) that systematically influence M_{vir} , the random errors in M_{vir} and absence of low multiplicity halos from the group catalog drive the recovered $N_{\text{avg}}(M)$ away from the true value. However, viewed as another clustering statistic, the richness-virial mass relation can provide another valuable constraint on the HOD, especially if the form of $N_{\text{avg}}(M)$ has been determined from other clustering measures, since it tests the overall mass scale and constrains the role of internal spatial and velocity biases.

The poor performance of the mean richness as a function of virial mass in recovering $N_{\text{avg}}(M)$ leads us to consider an alternative way of interpreting the richness virial mass relation. Figure 19 shows this relation for the same set of HOD models as Figure 18, but large points now represent the mean virial mass at each multiplicity N , and solid lines show the true $M_{\text{avg}}(N)$ relation. For a narrow $P(N|N_{\text{avg}})$, such as the Average distribution, $M_{\text{avg}}(N)$ and $N_{\text{avg}}(M)$ contain identical

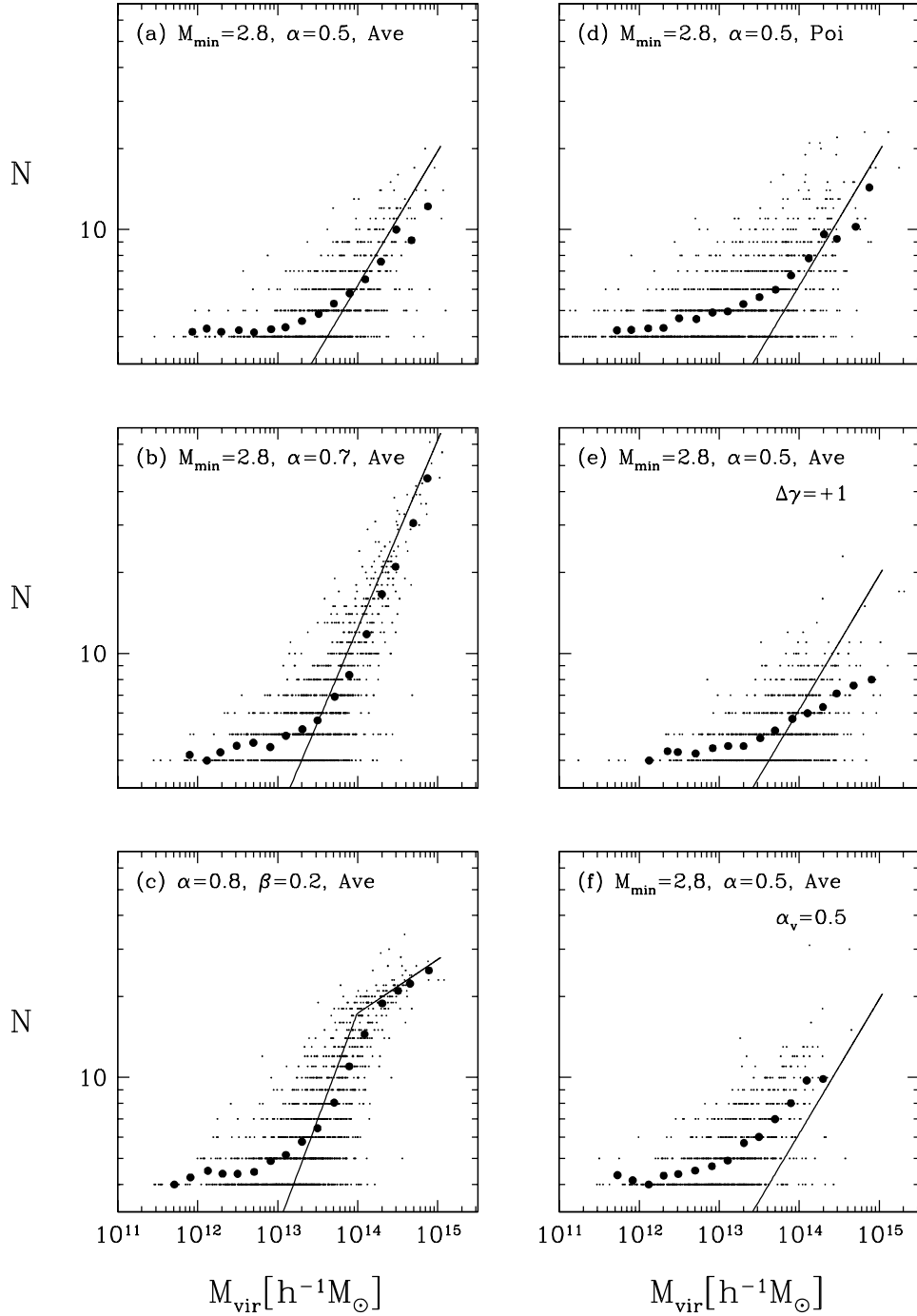


Fig. 18.— Richness vs. galaxy group virial mass estimates. Each panel represents a particular HOD model. The models are specified at the top of each panel, where M_{min} is given in units of $10^{11} h^{-1} M_{\odot}$, and Poi and Ave represent Poisson and Average $P(N|N_{\text{avg}})$ distributions, respectively. Galaxy groups were identified with a friends-of-friends algorithm in real space, and a virial estimator was used to estimate their mass. Each panel also shows the mean group richness in bins of M_{vir} (large points) as well as the input $N_{\text{avg}}(M)$ relation (line).

information, since $N_{\text{avg}}(M_{\text{avg}}(N)) = N$. However, in the Poisson case these two functions differ, as can be seen in Figure 19d, where $N_{\text{avg}}(M)$ is shown by the dashed line. Figure 19 demonstrates that most of the biases that affected the recovery of $N_{\text{avg}}(M)$ do not affect the recovery of $M_{\text{avg}}(N)$. Only velocity bias seriously hampers the recovery of $M_{\text{avg}}(N)$ (Fig. 19f), and, even in that case, only the amplitude of the relation is affected. Unfortunately, the $M_{\text{avg}}(N)$ relation cannot be inverted to recover $N_{\text{avg}}(M)$ without assuming a form for $P(N|N_{\text{avg}})$, so the improved performance of this statistic comes with the loss of model independence.

6. Measuring the HOD Empirically

The recurring theme of preceding sections is that different galaxy clustering statistics are sensitive to different aspects of the halo occupation distribution. The encouraging implication is that combinations of clustering measurements can pin down the properties of the HOD, hemming it in with complementary constraints. The 2dF and SDSS redshift surveys are ideally suited to this task because they can measure clustering with high precision over a wide dynamic range. The SDSS also provides detailed photometric information for all galaxies in the redshift survey, allowing studies of the HOD for a multitude of galaxy classes, and weak lensing measurements from the SDSS images can determine the galaxy-mass correlation function for each of these classes.

In this section, we outline a strategy for determining the HOD from observations, and although this outline is far from complete, we believe that it offers a promising route forward. Since the possible parameter space of HOD models is extremely broad, a practical strategy requires some procedure for getting a good first guess at $P(N|M)$, which can then be refined and tested using a battery of clustering measures. Our procedure assumes that the underlying cosmological model is known in advance based on independent observations, though the model can be further tested by seeing whether it reproduces all aspects of observed galaxy clustering for some HOD. The ability of large scale structure to constrain cosmology depends in part on whether two different cosmological models with two different halo occupation distributions can produce the same galaxy clustering; we consider this question briefly at the end of the section.

We take as our starting point the tight connection between $P(N|M)$ and the group multiplicity function implied by equation (27). If we assume that $P(N|N_{\text{avg}})$ is narrow, then group multiplicity is a monotonic function of halo mass, and determining $N_{\text{avg}}(M)$ from the multiplicity function is simply a matter of matching space densities. Given the measured $n_{\text{grp}}(> N)$ and the cumulative halo mass function $n_h(> M)$ computed from the cosmological model, we choose $N_{\text{avg}}(M)$ so that $n_{\text{grp}}[> N_{\text{avg}}(M)] = n_h(> M)$. More generally, one can assume a form of $P(N|N_{\text{avg}})$ and infer $N_{\text{avg}}(M)$ by reversing the convolution in equation (27). The relatively small impact of $P(N|N_{\text{avg}})$ on the multiplicity function compared to changes in $N_{\text{avg}}(M)$ (see Fig. 17) shows that results will not be overly sensitive to the assumed width of the distribution.

Figure 20 illustrates the performance of the monotonic matching method. The top panel plots the cumulative halo mass function derived from the GIF N-body simulation, with halos identified by the FoF algorithm as usual. The middle panel shows cumulative group multiplicity functions for three HOD models, with groups identified by the same FoF algorithm as described in § 5. The bottom panel shows the $N_{\text{avg}}(M)$ relations derived by matching $n_h(> M)$ to $n_{\text{grp}}(> N)$ and the

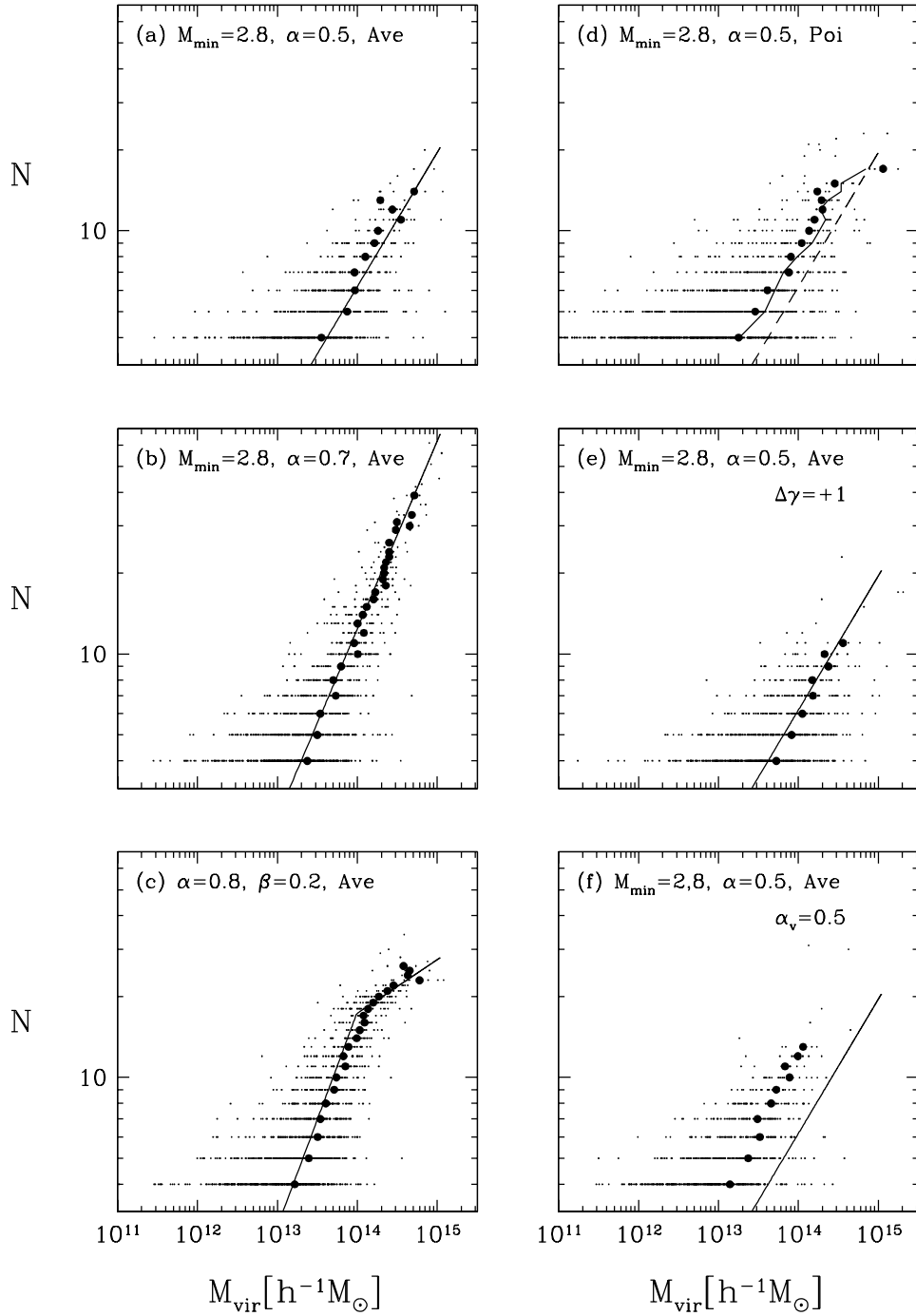


Fig. 19.— Same as Fig. 18, except that large points represent the mean estimated virial mass at fixed group richness N , solid lines show the true $M_{\text{avg}}(N)$, and the dashed line in panel (d) shows $N_{\text{avg}}(M)$.

true $N_{\text{avg}}(M)$ used as inputs to the HOD models. In all three cases, the method is impressively successful at recovering $N_{\text{avg}}(M)$ for $M \gtrsim 10^{13.5} h^{-1} M_{\odot}$, obtaining the correct power-law slopes for the $\alpha = 0.6$ and $\alpha = 1.0$ models and revealing the break in the broken power-law model. At low multiplicities, the discreteness of N causes a step-like behavior in $N_{\text{avg}}(M)$, but this could be easily repaired. The method works well for the $\alpha = 1.0$ Poisson model even though we have not applied any deconvolution correction.

The matching method illustrated in Figure 20 is a promising way of determining $N_{\text{avg}}(M)$ at high M , where halos contain large numbers of galaxies. For application to redshift survey data, the main challenge is to develop a good group-finding algorithm and understand any biases associated with it. When studying the HOD of galaxy classes, one would start with the group catalog and associated halo masses derived from the full, high density galaxy catalog, then measure the content of individual classes.

Group matching provides a partial guess at the HOD, which must be extrapolated to low masses, refined, and tested using other statistics. One important constraint on the extrapolation comes from the mean galaxy number density, $\bar{n}_g = \int_0^{\infty} dM \frac{dn}{dM} N_{\text{avg}}(M)$. A similar constraint with a different weighting of halos comes from the large scale bias factor, $b = \bar{n}_g^{-1} \int_0^{\infty} dM \frac{dn}{dM} b_h(M) N_{\text{avg}}(M)$, which can be inferred from the measured galaxy power spectrum given the assumed cosmological model. The most valuable constraints on halo occupation at low masses comes from the 1-halo regime of $\xi_g(r)$, since different separations probe different halo mass scales.

We can illustrate the constraining power of $\xi_g(r)$ using an approximation suggested by Figure 2a, which shows that the cumulative pair separation distribution $F(r/2R_{\text{vir}})$ is roughly a linear ramp out to a maximum separation $x_m \approx 0.6$ of the virial diameter, and is close to unity at larger separations. Under this approximation, the 1-halo term $\xi_{1h}(r)$ only receives contributions from halos with virial diameters $2R_{\text{vir}} > rx_m^{-1}$, or, using equation (12), with virial masses

$$M_l(r) = \frac{800\pi\bar{\rho}_m}{3} \left(\frac{r}{2x_m} \right)^3. \quad (29)$$

We can therefore rewrite equation (11) by substituting the constant value $F'(x) = x_m^{-1}$ and changing the lower limit of the integral to $M_l(r)$, which is now the only part of the integral with an r dependence. Differentiating both sides of the equation with respect to r and rearranging terms yields an expression relating the second factorial moment at M_l to the 1-halo correlation function and its logarithmic derivative at r :

$$\langle N(N-1) \rangle_{M_l} = \frac{4\pi}{3} \bar{n}_g^2 \left(\frac{dn}{d\ln M} \Big|_{M_l} \right)^{-1} r^3 \left(2 + \frac{d\ln \xi_{1h}(r)}{d\ln r} \right) \xi_{1h}(r). \quad (30)$$

Figure 21 illustrates the performance of equation (30). Despite the rather crude, linear ramp approximation for $F(r/2R_{\text{vir}})$, the estimates of $\langle N(N-1) \rangle_M$ derived from $\xi_{1h}(r)$ recover the true values shown by the solid lines for both of these HOD models, which have $M_{\text{min}} = 2.8 \times 10^{11} h^{-1} M_{\odot}$, $\alpha = 0.5$, and Poisson and Average $P(N|N_{\text{avg}})$, respectively. In practice, one could only apply this method to halos with virial diameters $2R_{\text{vir}} \lesssim 0.5x_m^{-1} h^{-1} \text{Mpc} \sim 0.8h^{-1} \text{Mpc}$ (mass

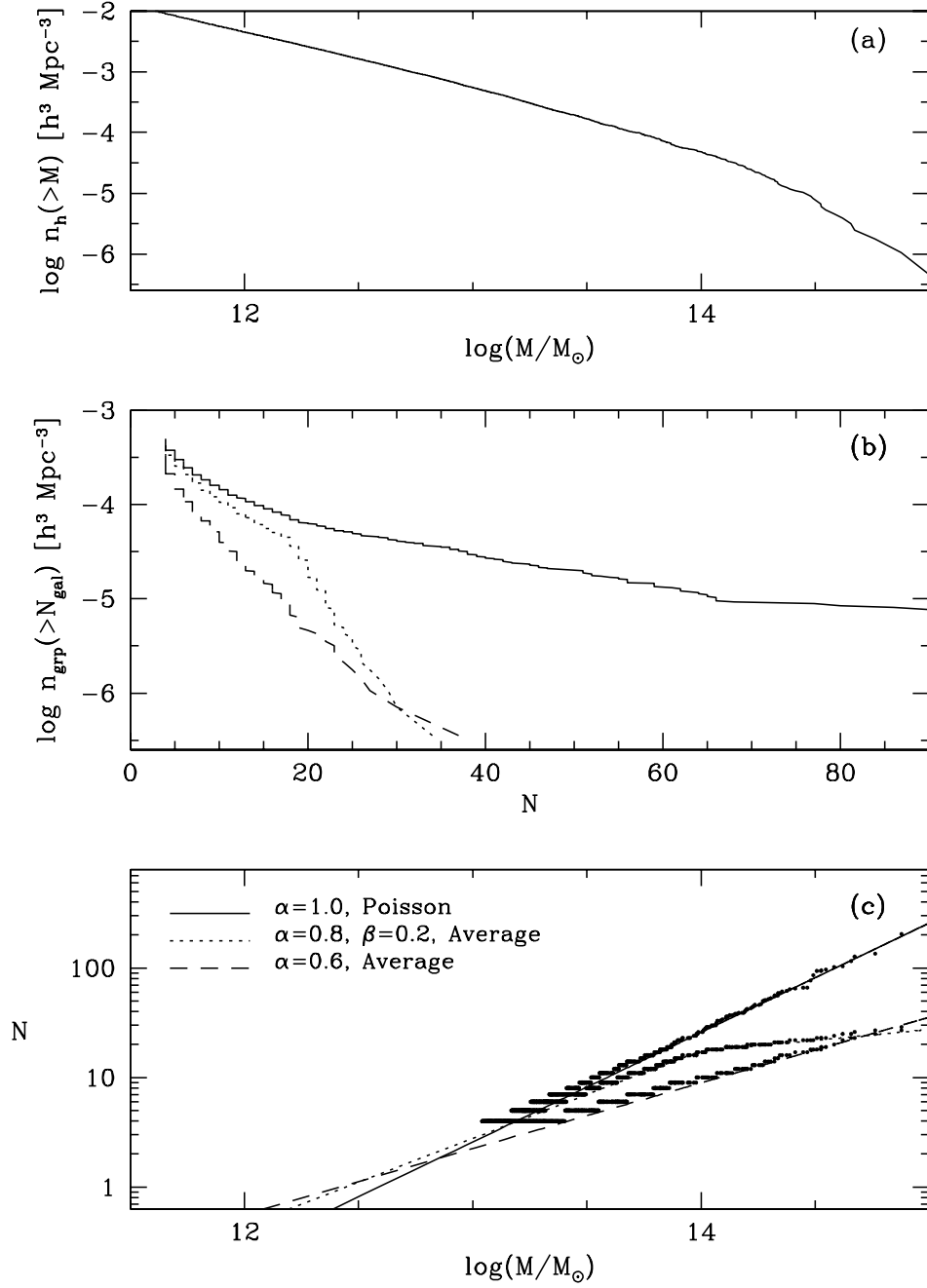


Fig. 20.— Recovery of $N_{\text{avg}}(M)$ from the group multiplicity function. Panel (a) shows the halo mass function $n_h(M)$ derived from the GIF N-body simulation, where halos were identified with a FoF algorithm. Panel (b) shows group multiplicity functions $n_{\text{grp}}(>N)$ for three HOD models, where galaxy groups were identified with the same FoF algorithm. Panel (c) shows the resulting $N_{\text{avg}}(M)$ relations from matching $n_h(M)$ to $n_{\text{grp}}(>N)$ (points). Also shown, for comparison, are the true $N_{\text{avg}}(M)$ functions that were used as inputs for the HOD models (lines).

$M \lesssim 5 \times 10^{12} h^{-1} M_\odot$ for $\Omega_m = 0.3$), since $\xi_g(r)$ departs from $\xi_{1h}(r)$ at $r \gtrsim 0.5h^{-1} \text{Mpc}$ (see Fig. 7). However, one could extend the range somewhat by calculating the 2-halo contribution to $\xi_g(r)$ and subtracting it to obtain $\xi_{1h}(r)$; alternatively, a numerical method that uses equation (11) directly instead of the linear ramp approximation would not be difficult to implement. The important lesson of equation (30) and Figure 21 is that $\xi_{1h}(r)$ provides fairly well localized information about $\langle N(N-1) \rangle_M$, in just the mass range where the group matching method breaks down.

The small scale correlation function depends on $\langle N(N-1) \rangle_M$ rather than $N_{\text{avg}}(M)$, and it has an additional dependence on the assumed galaxy profile (though Fig. 6 shows that this dependence is not strong). However, it is clear from the discussion above that matching $n_{\text{grp}}(> N)$, \bar{n}_g , and $\xi_g(r)$ already places strong constraints on $P(N|M)$ for a given cosmology. A trial HOD inferred by the techniques outlined above can be tested and refined using other clustering statistics. The VPF gives strong guidance on the low mass end of $P(N|M)$, especially the value of M_{min} . Higher order correlations probe the higher moments of $P(N|N_{\text{avg}})$. Additional strong tests come from the mean virial mass as a function of multiplicity and from the pairwise velocity dispersion, which is sensitive to the mean occupation at high mass and to $P(N|N_{\text{avg}})$ at low mass. Success in matching spatial clustering but failure with these dynamical measures could be a signature of an incorrect assumption about the underlying cosmology (e.g., the wrong value of Ω_m), or it could be an indication of velocity bias ($\alpha_v \neq 1$). The scale dependence of the pairwise dispersion can help discriminate between these possibilities, since $\sigma_v^2(r)$ combines terms that depend on α_v with others that do not (see eq. [22]). Lensing measurements of the galaxy-mass correlation function (or the analogous group-mass correlation function) provide stronger discrimination by probing halo mass scales independently of galaxy peculiar velocities. The 1-halo regime of $\xi_{gm}(r)$ also constrains $N_{\text{avg}}(M)$ in a range where $\xi_g(r)$ constrains $\langle N(N-1) \rangle_M$.

Suppose we find an HOD that reproduces all of these properties of observed galaxy clustering. Can we take this success as evidence that the assumed cosmological model is itself correct, or could there be some other combination of cosmology and HOD that would yield the same results? In other words, do cosmology and HOD bias have degenerate effects on galaxy clustering, or can sufficiently precise measurements constrain both independently? We reserve a detailed investigation of this question for future work, but qualitative arguments suggest grounds for optimism.

Let “model 1” denote our supposed successful combination of cosmological model and HOD prescription. If we raise Ω_m but keep the linear theory matter power spectrum $P_{\text{lin}}(k)$ the same, then the dark matter halo population will be essentially unchanged except that all masses will grow by the factor $\Omega_{m,2}/\Omega_{m,1}$, including the characteristic mass M_* of the halo mass function. If we maintain the same HOD as a function of M/M_* , then the spatial clustering of galaxies will stay the same, but dynamical measures like the pairwise velocity dispersion or virial mass vs. richness relation will not. Changes to dynamically sensitive statistics could be partially repaired by introducing velocity bias, with $\alpha_{v,2} < \alpha_{v,1}$, but this suppression will not disguise changes in $\sigma_v^2(r)$ or $P^S(k)$ at large scales or changes in $\xi_{gm}(r)$ at any scale.

For a less easily detectable change, we can reduce the amplitude of $P_{\text{lin}}(k)$ at the same time we increase Ω_m , maintaining a “cluster normalization” condition $\sigma_{8,2}\Omega_{m,2}^{0.5} \approx \sigma_{8,1}\Omega_{m,1}^{0.5}$ (White, Efstathiou, & Frenk 1993). This change preserves (approximately) the velocity scale of rich clusters

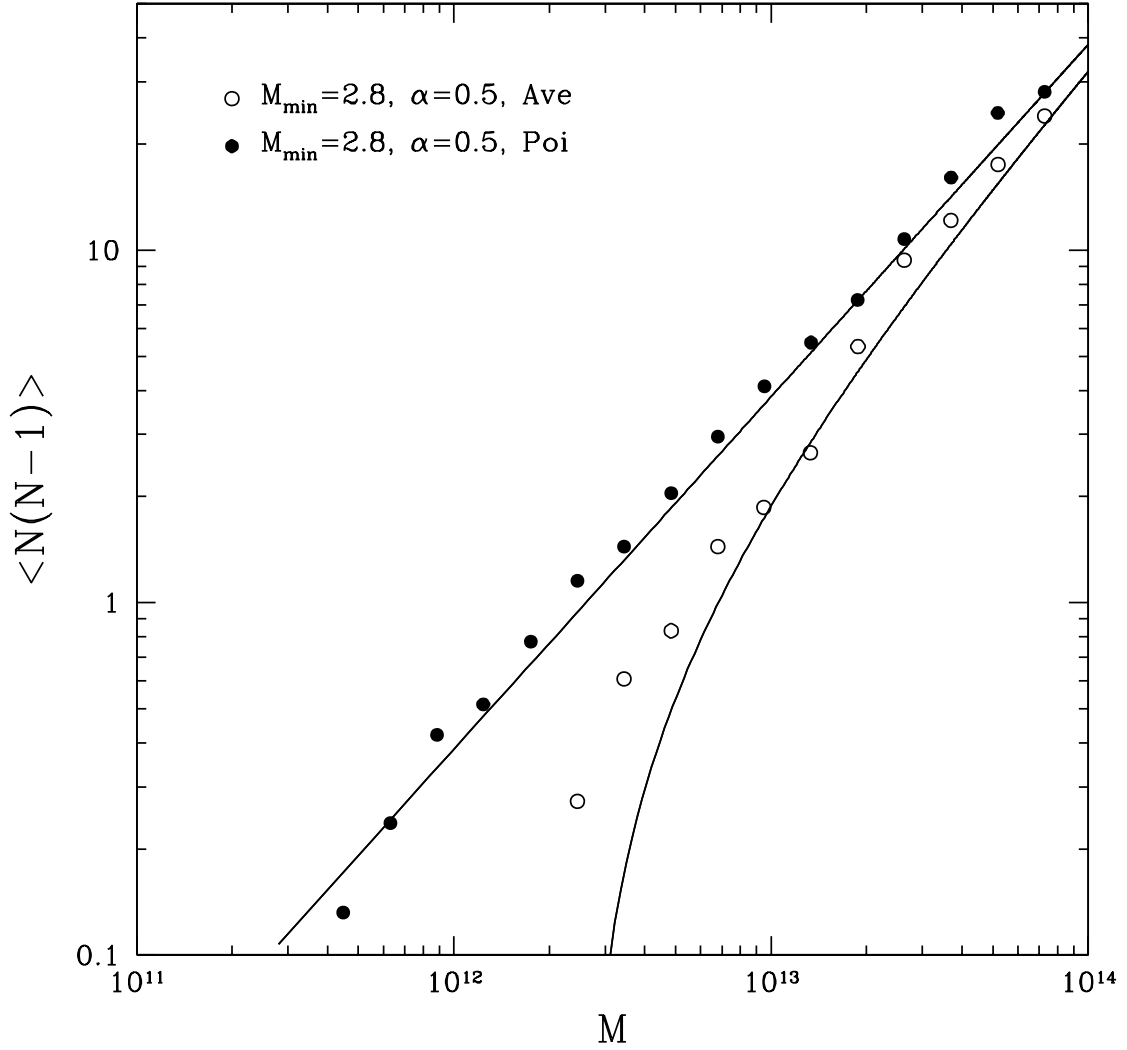


Fig. 21.— Recovery of $\langle N(N-1) \rangle_M$ from $\xi_{1h}(r)$ using eq. (30). The solid and open circles show the recovered $\langle N(N-1) \rangle_M$ for Poisson and Average $P(N|N_{\text{avg}})$ HOD models, respectively. Also shown for comparison, are the “true” $\langle N(N-1) \rangle_M$ relations that were used as inputs for the HOD models (lines).

and large scale flows, but it reduces the length scale of non-linearity in the matter distribution, by roughly the factor $(\Omega_{m,2}/\Omega_{m,1})^{1/3}$ required to keep M_* constant in physical units. If we maintain the same relative galaxy populations as a function of M/M_* , then all characteristic scales in the galaxy clustering drop by the same factor, including the galaxy correlation length r_0 . To return r_0 and the space density \bar{n}_g to their original values, we would need to raise M_{\min}/M_* , or change α , or make other alterations to $P(N|M)$, and these changes would generally have different impact on different clustering statistics. Furthermore, the cluster normalization condition preserves the amplitude of the halo mass function on cluster scales but changes the overall shape of dn/dM in physical units, with a steeper fall-off at high masses for models with lower σ_8 (higher Ω_m). This change could be partially repaired by altering the shape of $P_{\text{lin}}(k)$, but that would alter the halo spatial clustering. We tentatively conclude that substantial changes to the value of Ω_m or the normalization or shape of $P_{\text{lin}}(k)$ cannot be masked by changes in the HOD. (See Zheng et al. [2002] for further discussion of these issues.)

Given the increasingly tight constraints on cosmological parameters that come from CMB anisotropies, the Lyman- α forest, gravitational lensing, Type Ia supernovae, cluster evolution, and other data, a procedure that recovers the HOD for an assumed cosmology would be very valuable in itself. Successful application of this procedure to surveys like the 2dFGRS and SDSS would tell us essentially everything that local ($z = 0$) galaxy clustering has to say about galaxy formation, assuming that the adopted cosmological model is correct. Determinations of the HOD for different galaxy classes would provide detailed targets for analytic or numerical models of galaxy formation and insight into the physics that controls galaxy luminosities, colors, and morphologies.

If, as we have speculated, the effects of cosmology and bias are not degenerate, then the HOD determination procedure becomes something still more powerful: a systematic way of testing cosmological models against galaxy clustering data given only some very general assumptions about galaxy formation (basically the validity of the HOD framework itself). Incorrect cosmological models would fail to reproduce the observations for any choice of HOD. Of course, galaxy clustering provides a testing ground for cosmology even with less detailed assumptions about galaxy formation, since the effects of “local” bias on the power spectrum, higher order moments, redshift-space distortions, and galaxy density and velocity fields become relatively simple on sufficiently large scales (see, e.g., Coles 1993; Fry & Gaztañaga 1993; Mann, Peacock, & Heavens 1998; Scherrer & Weinberg 1998; Narayanan et al. 2000; Berlind et al. 2001). However, by incorporating HOD determination into analyses of galaxy clustering, one can use information from the highly nonlinear scales of individual halos to calculate effective “bias factors” for a variety of clustering statistics in the intermediate, moderately nonlinear regime, where the impact of bias may not be simple. This approach sharpens the sensitivity of clustering studies to small departures from the “minimal” cosmological model, which could be produced by light but not massless neutrinos, by a non-standard relativistic background, by non-scale invariant inflation, or even by a small contribution from isocurvature or non-Gaussian fluctuations. Analysis of separate galaxy classes with different HODs would provide redundant checks of the results, since the properties of the underlying mass clustering should be independent of the tracer population used to infer them.

The monotonic matching method proposed above is similar to the technique suggested by Peacock & Smith (2000), except that they use the “galaxy systems luminosity function” in place of the multiplicity function and extend the assumption of a monotonic relation between halo

mass and luminosity into the single-galaxy regime. Applying the technique to the data of Moore et al. (1993) and the Λ CDM halo mass function, Peacock & Smith (2000) recover an $N_{\text{avg}}(M)$ relation that is shallow at low mass and steepens towards higher masses, qualitatively similar to the predictions of semi-analytic models and hydrodynamic simulations (Benson et al. 2000; Berlind et al., in preparation) and to the broken power-law model whose correlation function is illustrated by the solid curve in Figure 9. As the first determination of the HOD from empirical data, this recovery of a relation that resembles theoretical predictions and yields approximately the observed galaxy power spectrum (Peacock & Smith 2000, figure 8) is very encouraging. Using similar methodology, Marinoni & Hudson (2001) have recently obtained a similar $N_{\text{avg}}(M)$ relation for a new sample of optically selected galaxies. With a different, model fitting approach, Jing, Mo, & Börner (1998), Jing & Börner (1998), and Jing, Börner & Suto (2002) conclude that suppression of the fraction of galaxies in high mass halos can help explain the observed form and amplitude of the galaxy two-point and three-point correlation functions and pairwise velocity dispersion. Determinations of the HOD from the 2dF and SDSS redshift surveys will yield a far more detailed picture of the relation between galaxies and dark matter and among different galaxy types themselves. The improved constraints on dark matter clustering have the potential to reveal effects that are quantitatively subtle but have profound physical implications.

7. Summary

In the HOD framework, the bias of a population of galaxies is fully defined by the conditional probability $P(N|M)$ that a halo of virial mass M contains N galaxies, together with prescriptions that specify the relative spatial and velocity distributions of galaxies and dark matter within virialized dark matter halos. This framework provides an informative basis for connecting observations of galaxy clustering to the physics of galaxy formation, and it opens a route to the empirical determination of bias from galaxy redshift surveys. We have investigated the sensitivity of galaxy clustering statistics to features of the HOD, focusing on models with mean occupation $N_{\text{avg}}(M) \propto M^\alpha$ for $M > M_{\text{min}}$, and found the following results:

1) The amplitude of the galaxy correlation function on large scales is determined by the relative numbers of galaxies in high mass and low mass halos, and is thus sensitive to α and, to a lesser extent, M_{min} . On small scales, $\xi_g(r)$ receives the largest contribution from galaxy pairs in halos of virial radius $R_{\text{vir}} \sim r$, so different separations probe the occupation at different masses. The amplitude and shape of $\xi_g(r)$ are highly sensitive to α , M_{min} , and $P(N|N_{\text{avg}})$, though each feature affects $\xi_g(r)$ in a different way. The spatial distribution of galaxies within halos has a relatively modest impact that is confined to small spatial scales.

2) In HOD models, a power-law correlation function emerges from a balance of several competing effects, and it therefore requires rather specific combinations of parameters. The sensitivity of $\xi_g(r)$ to HOD parameters implies that its observed power-law form is a strong constraint on the physics of galaxy formation, and that the success of semi-analytic models and hydrodynamic simulations in reproducing this form is entirely non-trivial.

3) The influence of HOD parameters on the galaxy-mass cross-correlation function is similar to the effect on $\xi_g(r)$, except that $\xi_{gm}(r)$ is independent of $P(N|N_{\text{avg}})$ even on small scales. The

direct dependence of galaxy-galaxy lensing measurements on the mass of halos makes them an especially valuable test of the background cosmology.

4) The bispectrum contains complementary information to two-point statistics due to its greater weighting of high mass halos and its dependence on the third moment of $P(N|N_{\text{avg}})$. The dependence of the reduced bispectrum $Q(k)$ on α and M_{min} is fairly complex, and different from the dependencies found for $\xi_g(r)$.

5) The void probability function (VPF) is sensitive to the low M regime of $P(N|M)$, where halos have a significant probability of containing no galaxies. In particular, the VPF is most sensitive to the cut-off halo mass M_{min} .

6) The pairwise velocity dispersion is particularly sensitive to α , which controls the fraction of galaxies in high dispersion halos, and to the presence of velocity bias in halos. In addition, $\sigma_v^2(r)$ is sensitive to Ω_m and the amplitude of the matter power spectrum.

7) The ratio of the redshift to real-space power spectra is sensitive to $N_{\text{avg}}(M)$ and velocity bias, as well as Ω_m . Velocity dispersions within halos influence the redshift-space power spectrum out to large scales.

8) The group multiplicity function is sensitive to M_{min} and α in different ways: increases in M_{min} cause a roughly horizontal shift of $n_{\text{grp}}(> N)$ towards greater N , whereas increases in α cause a drastic change in the slope of $n_{\text{grp}}(> N)$.

9) The richness - virial mass relation is a direct probe of $P(N|M)$. However, it is subject to biases that make it difficult to extract $N_{\text{avg}}(M)$. The mean halo mass per multiplicity, $M_{\text{avg}}(N)$, can be extracted much more robustly, though even this measure can be affected by velocity bias.

The different sensitivities of these clustering statistics to different features of the HOD suggest that the HOD can be empirically determined from observations of galaxy clustering. We have outlined a strategy for measuring the HOD from a galaxy redshift survey, which involves obtaining a first guess at $P(N|M)$ and then refining that guess with additional clustering statistics. In its present form, our strategy assumes that the cosmological model is known *a priori*. However, the effects of changing the HOD should generally be different from the effects of changing cosmological parameters, so an incorrect cosmological model may be unable to reproduce the full suite of galaxy clustering statistics for any choice of HOD. At the very least, determinations of the HOD for different classes of galaxies from the 2dF and SDSS redshift surveys will provide considerable insight into the physics of galaxy formation and the origin of galaxy properties. If the degeneracy between cosmology and bias can indeed be broken, then determinations of the HOD will also sharpen tests of the standard cosmological model, perhaps revealing the imprint of new physics on the large scale structure of the universe.

We are indebted to Vijay Narayanan for many helpful discussions on the subject of bias and for supplying some of the software used in this project. We thank Carlton Baugh, Andrew Benson, James Bullock, Chris Burke, Shaun Cole, Carlos Frenk, Andrey Kravtsov, and Roman Scoccimarro for helpful discussions, input, and comments, and Carlton Baugh for making the APM correlation function available to us in electronic format. We also thank the Virgo consortium for making

their simulations publicly available. This work was supported by NSF grants AST-9802568 and AST-0098584. AAB received additional support from a Presidential Fellowship from the Graduate School of The Ohio State University.

References

- Baugh, C. 1996, MNRAS, 280, 267
- Benson, A. J., Cole, S., Frenk, C. S., Baugh, C. M., & Lacey, C. G. 2000, MNRAS, 311, 793
- Benson, A. J. 2001, MNRAS, 325, 1039
- Berlind, A. A., Narayanan, V. K., & Weinberg, D. H. 2001, ApJ, 549, 688
- Blanton, M., Cen, R., Ostriker, J. P., & Strauss, M. A. 1999, ApJ, 522, 590
- Bond, J. R., Cole, S., Efstathiou, G., & Kaiser, N. 1991, ApJ, 379, 440
- Brainerd, T. G., Blandford, R. D., & Smail, I. 1996, ApJ, 466, 623
- Bullock, J. S., Kolatt, T. S., Sigad, Y., Somerville, R. S., Kravtsov, A. V., Klypin, A. A., Primack, J. R., & Dekel, A. 2001, MNRAS, 321, 559
- Bullock, J. S., Weschsler, R. H., & Somerville, R. S. 2001, MNRAS, 329, 246
- Casas-Miranda, R., Mo, H. J., Sheth, R. K., & Börner, G. 2001, MNRAS, in press
- Cen, R., & Ostriker, J. P. 2000, ApJ, 538, 83
- Cole, S., Fisher, K. B., & Weinberg, D. H. 1994, ApJ, 267, 785
- Cole, S., Fisher, K. B., & Weinberg, D. H. 1995, ApJ, 275, 515
- Coles, P. 1993, MNRAS, 262, 1065
- Coles, P., Melott, A. L., & Munshi, D. 1999, ApJ, 521, L5
- Colín, P., Klypin, A. A., Kravtsov, A. V., & Khokhlov, A. M. 1999, ApJ, 523, 32
- Colless, M. et al. 2001, MNRAS, 328, 1039
- Connolly, A. J. et al. 2001, ApJ, submitted (astro-ph/0107417)
- Davé, R., Hernquist, L., Katz, N., & Weinberg, D. H. 2000, in Proc. Rencontres Internationales de l'IGRAP, "Clustering at High Redshift", eds. A. Mazure, O. Le Fevre, & V. Le Brun (San Francisco: ASP Conference Series v.200), p.402
- Davis, M., & Peebles, P. J. E. 1983, ApJ, 267, 465
- Davis, M., Efstathiou, G., Frenk, C. S., & White, S. D. M. 1985, ApJ, 292, 371
- De Filippis, E., Longo, G., Andreon, S., Scaramella, R., Testa V., de Carvalho, R. R., & Djorgovski, S. G. 1999, MmSAI, in press, (astro-ph/9909368)
- Dekel, A., & Lahav, O. 1999, ApJ, 520, 24
- dell'Antonio, I. P., & Tyson, J. A. 1996, ApJ, 473, 17L,

- Efstathiou, G., Bond, J. R., & White, S. D. M. 1992, *MNRAS*, 258, 1
- Eke, V. R., Cole, S., & Frenk, C. S. 1996, *MNRAS*, 282, 263
- Evrard, A. E. 1987, *ApJ*, 316, 36
- Fischer, P. et al. 2000, *AJ*, 120, 1198
- Fry, J. 1984, *ApJ*, 279, 499
- Fry, J. N., & Gaztañaga, E. 1993, *ApJ*, 413, 447
- Fry, J. N. 1994, *Phys. Rev. Lett.*, 73, 215L
- Gaztañaga, E., & Juskiewicz, R. 2001, *ApJ*, 558, 1L
- Gott, J. R., & Turner, E. L. 1977, *ApJ*, 216, 357
- Griffiths, R. E., Casertano, S., Im, M., Ratnatunga, K. U. 1996, *MNRAS*, 282, 1159
- Guzik, J., & Seljak, U. 2001, *MNRAS*, 321, 439
- Guzzo, L., Strauss, M. A., Fisher, K. B., Giovanelli, R., & Haynes, M. P. 1997, *ApJ*, 489, 37
- Hamilton, A. J. S. 1998, in *The Evolving Universe*, ed. Hamilton, D., (Kluwer Academic, Dordrecht) p. 185 (astro-ph/9708102)
- Hamilton, A. J. S., Matthews, A., Kumar, P., & Lu, E. 1991, *ApJ*, 374, L1
- Hatton, S. J., & Cole, S. 1999, *MNRAS*, 310, 113
- Heisler, J., Tremaine, S., & Bahcall, J. N. 1985, *ApJ*, 298, 8
- Hudson, M. J., Gwyn, S. D. J., Dahle, H., Kaiser, N. 1998, *ApJ*, 503, 531
- Jenkins, A., Frenk, C. S., Pearce, F. R., Thomas, P. A., Colberg, J. M., White, S. D. M., Couchman, H. M. P., Peacock, J. A., Efstathiou, G., & Nelson, A. H. 1998, *ApJ*, 499, 20
- Jing, Y. P. 1998, *ApJ*, 503, 9
- Jing, Y. P., & Börner, G. 1998, *ApJ*, 503, 37
- Jing, Y. P., Mo, H. J., & Börner, G. 1998, *ApJ*, 494, 1
- Jing, Y. P., Börner, G., & Suto, Y. 2002, *ApJ*, 564, 15
- Juskiewicz, R., Weinberg, D. H., Amsterdamski, P., Chodorowski, M., & Bouchet, F. 1995, *ApJ*, 442, 39
- Kaiser, N. 1987 *MNRAS*, 227, 1
- Kauffmann, G., Colberg, J. M., Diaferio, A., & White, S. D. M. 1999, *MNRAS*, 303, 188

- Kauffmann, G., Nusser, A., & Steinmetz, M. 1997, MNRAS, 286, 795
- Lacey, C. G., & Cole, S. 1993, MNRAS, 262, 627
- Lemson, G. & Kauffmann, G. 1999, MNRAS, 302, 111
- Limber, D. 1954, ApJ, 119, 655
- Little, B., & Weinberg, D. H. 1994, MNRAS, 267, 605
- Ma, C., & Fry, J. N. 2000, ApJ, 543, 503
- Maddox, S. J., Efstathiou, G., Sutherland, W. J., & Loveday, J. 1990 MNRAS, 242, 43
- Maia, M. A. G., da Costa, & L. N., Latham, D. W. 1989, ApJS, 69, 809
- Mann, R. G., Peacock, J. A., & Heavens, A. F. 1998, MNRAS, 293, 209
- Marinoni, C., & Hudson, M. J. 2001, ApJ, submitted (astro-ph/0109134)
- McLelland, J., & Silk, J. 1977, ApJ, 217, 331
- McKay, T. et al. 2001, ApJ, submitted, (astro-ph/0108013)
- Mo, H. J., & White, S. D. M. 1996, MNRAS, 282, 347
- Moore, B.; Frenk, C. S.; White, S. D. M 1993, MNRAS, 261, 827
- Narayanan, V. K., Berlind, A. A., & Weinberg, D. H. 2000, ApJ, 528, 1
- Navarro, J. F., Frenk, C. S., & White, S. D. M. 1997, ApJ, 490, 493
- Neyman, J., & Scott, E. L. 1952, ApJ, 116, 144
- Nolthenius, R., Klypin, A., Primack, J. R. 1994, ApJ, 422, 45L
- Norberg, P. et al. 2001, MNRAS, 328, 64
- Norberg, P., et al. 2002, MNRAS, in press, astro-ph/0112043
- Peacock, J. A., & Dodds, S. J. 1994, MNRAS, 267, 1020
- Peacock, J. A., & Dodds, S. J. 1996, MNRAS, 280, 19
- Peacock, J. A., & Smith, R. E. 2000, MNRAS, 318, 1144
- Peacock, J. A. et al. 2001, Nature, 410, 169
- Pearce, F. R., Jenkins, A., Frenk, C. S., Colberg, J. M., White, S. D. M., Thomas, P. A., Couchman, H. M. P., Peacock, J. A., & Efstathiou, G. 1999 ApJ, 521L, 99
- Peebles, P. J. E. 1974, A&A, 32, 197
- Porciani, C., & Giavalisco, M. 2001, ApJ, 565, 24

- Press, W. H., & Schechter, P. 1974, *ApJ*, 187, 425
- Ramella, M., Geller, M. J., & Huchra, J. P. 1989, *ApJ*, 344, 57
- Ramella, M. et al. 1999, *A&A*, 342, 1
- Sargent, W. L. W., & Turner, E. L. 1977, *ApJ*, 212, 3L
- Scherrer, R. J., & Bertschinger, E. 1991, *ApJ*, 381, 349
- Scherrer, R. J., & Weinberg, D. H. 1998, *ApJ*, 504, 607
- Scoccimarro, R., Sheth, R. K., Hui, L., & Jain, B. 2000, *ApJ*, 546, 20
- Seljak, U. 2000, *MNRAS*, 318, 203
- Seljak, U. 2001, *MNRAS*, 325, 1359
- Sheth, R. K., Hui, L., Diaferio, A., & Scoccimarro, R. 2001, *MNRAS*, 325, 1288
- Smith, D. R., Bernstein, G. M., Fischer, P., Jarvis, M. 2001, *ApJ*, 551, 643
- Somerville, R. S., Lemson, G., Sigad, Y., Dekel, A., Kauffmann, G., & White, S. D. M. 2001, *MNRAS*, 320, 289
- Tully, R. B., & Fisher, J. R. 1977, *A&A*, 54, 661
- Vogele, M. S., Geller, M. J., Park, C., & Huchra, J. P. 1994, *AJ*, 108, 745
- Wang, X., Tegmark, M., & Zaldarriaga, M. 2001, *Phys. Rev. D.*, submitted (astro-ph/0105091)
- Weinberg, D. H. 1995, in *Wide-Field Spectroscopy and the Distant Universe*, eds. S. J. Maddox and A. Aragón-Salamanca (Singapore: World Scientific), 129
- White, M. 2001, *MNRAS*, 321, 1
- White, M., Hernquist, L., & Springel, V. 2001, *ApJ*, 550, L129
- White, M., Hernquist, L., & Springel, V. 2001, *ApJ*, submitted (astro-ph/0107023)
- White, S. D. M., Efstathiou, G. P., & Frenk, C. S. 1993, *MNRAS*, 262, 1023
- Wilson, G., Kaiser, N., & Luppino, G. A. 2001, *ApJ*, 556, 601
- Wu, X., Chiueh, T., Fang, L., & Xue, Y. 1998, *MNRAS*, 301, 861
- York, D. et al. 2000, *AJ*, 120, 1579
- Yoshikawa, K., Taruya, A., Jing, Y. P., & Suto, Y. 2001, *ApJ*, 558, 520
- Zehavi, I. et al. 2001, *ApJ*, submitted (astro-ph/0106476)
- Zheng, Z., Tinker, J. L., Weinberg, D. H., & Berlind, A. A. 2002, *ApJ*, submitted, astro-ph/0202358